UNIVERSITY OF SOUTHAMPTON

The Integration of Fibre Optics for Atom Chips

by

Stephen John Helsby

A thesis submitted in partial fulfillment for the degree of Doctor of Philosophy

in the

Faculty of Engineering, Science and Mathematics

OPTOELECTRONICS RESEARCH CENTRE

March 2008

UNIVERSITY OF SOUTHAMPTON

ABSTRACT

FACULTY OF ENGINEERING, SCIENCE AND MATHEMATICS
OPTOELECTRONICS RESEARCH CENTRE

Doctor of Philosophy

THE INTEGRATION OF FIBRE OPTICS FOR ATOM CHIPS

by Stephen John Helsby

This thesis reports on the progress made towards the integration of fibre optics components for the atom chip, a device developed to manipulate matter on the atomic scale for the purpose of quantum information processing, novel applications, and fundamental research. Following in the direction of the electronics industry, miniaturisation has resulted in exquisite control of cold atoms above surfaces, allowing the vision of a matter wave toolbox to come closer to fruition. However, although the size of the components necessary for guiding atoms via magnetic or electrostatic fields has been greatly reduced, there is still a need to scale down the optical components.

With this objective in mind, research and development of micro-optic devices capable of detecting single atoms has been undertaken. Fibre optics have been implemented in two main directions, fluorescence detection, and fibre gap cavities, with the latter forming the main part of this work. Here I am concerned with fibre Fabry-Perot cavities of a few centimetres in length, containing implanted reflectors, and accommodating a gap of several micrometres for atomic access. The interaction of the atom with the cavity field perturbs the transmitted signal to provide an indication of its presence.

The development of these cavities is detailed in this thesis, from early use of evaporated gold coated mirrors to the fully integral solution of photorefractive Bragg gratings. In addition to a thorough analysis of the optical properties of these fibre gap cavities, experimental results indicate that these gap cavity devices can be constructed with the sensitivity necessary for single atom detection.

Contents

List of Figures

List of Tables

Declaration of Authorship

I, Stephen John Helsby

declare that the thesis entitled

The Integration of Fibre Optics for Atom Chips

and the work presented in the thesis are my own, and have been generated by me as the result of my own original research. I confirm that:

- this work was done wholly or mainly while in candidature for a research degree at this University;
- where any part of this thesis has previously been submitted for a degree or any other qualification at this University or any other institution, this has been clearly stated;
- where I have consulted the published work of others, this is always clearly attributed;
- where I have quoted from the work of others, the source is always given. With the exception of such quotations, this thesis is entirely my own work;
- I have acknowledged all main sources of help;
- where the thesis is based on work done by myself jointly with others, I have made clear exactly what was done by others and what I have contributed myself;
- parts of this work have been published as: (See *List of Publications*).

Signed: _____

Date: _____

Acknowledgements

There are many people who I must thank for getting me so far, and helping me along the way. Firstly though, I would like to thank both the Jersey Education Department and the Optoelectronics Research Centre for their financial support. I am also very grateful to my supervisor, Prof. Peter Kazansky, for giving me the opportunity to work on such an interesting project, and for his support and inspiration over the years.

When I began I was lucky enough to work with Bruce Klappauf, a mentor through whom I learnt much, and who got me started along the road. Continuing with members of the group, I would like to thank Peter Horak, Costa, and Hebe. Peter Horak deserves particular thanks as he has been a wealth of theoretical knowledge, as well as being supportive and helpful in all aspects of my project and time here. I would also like to thank him for his feedback and criticism on my thesis, and also thank Eleanor Tarbox for her proofreading.

On the technical front, I owe much to Morten Ibsen for writing the Bragg gratings I used in this project, and his help with them in general. I would also like to thank everyone who lent and helped me with equipment, particularly when I was trying to get up and running after the fire. Thanks to Gates, Corin, Gilberto, Mike, Iain, Ed, and many more. Apologies here to anyone I have not mentioned, as the support I received was overwhelming. Special thanks here must also go to Stuart Russell, who found room for me in his lab. For technical support I would like to thank Ed Weatherby and Mark Lessey for help both in Mountbatten and for getting the new lab up and running, and for help over the years I am also grateful to Rob Standish, Dave Sager, Simon Butler, Andrew Webb, Chris Nash and Tim McIntyre. A big thank you to the network staff, Dave Oliver, Kevin Sumner and Arthur Longhurst, for keeping the computers running, and to all the administrative staff, especially Eve Smith.

I would like to thank all the friends I have made at the ORC for their moral support, and finally I owe a huge thank you to Sarah for her moral and emotional support throughout.

To
Sarah and Lily

Nomenclature

Abbreviations:

FSR	cavity free spectral range
FWHM	full width at half maximum
CCD	charge-coupled device
UV	ultraviolet
ECDL	external cavity diode laser
FBG	fibre Bragg grating
OSA	optical spectral analyser
LED	light emitting diode
ASE	amplified spontaneous emission
DC	direct current/non-oscillating component
PC	personal computer
WF	writing fluence
SD	standard deviation
SNR	signal to noise ratio
ICC	integrated coupling constant
NICC	normalised integrated coupling constant
AR	anti-reflection (coating)
PID	proportional-integral-derivative (control)
NA	numerical aperture of fibre
MFD	mode field diameter
FP	Fabry-Perot
FFP	fibre Fabry-Perot
QED	quantum electrodynamics

Symbols:

Chapter 2

α	amplitude of coherent light
η	pump rate
κ_T	rate of photon transmission through mirrors
p_{in}	rate of incident photons
Δ_a	atomic detuning
Δ_c	cavity detuning
σ_+, σ_-	atomic raising and lowering operators
$a^\dagger$, a	mode creation and annihilation operators
ρ	density operator
g	single-photon Rabi frequency
$\mathcal{L}$	evolution operator
N	mean cavity photon number
Γ	spontaneous decay half-width
κ_c	total loss rate from cavity
σ_a	atomic resonant scattering cross-section
A	cross-section of cavity mode
κ_{loss}	photon loss rate excluding mirror transmission
$N_{out,0}$	number of photons arriving at detector for empty cavity
N_{out}	number of photons arriving at detector
P	laser power
n_{rt}	average number of cavity round trips
M	number of spontaneously scattered photons during detection
ρ_{11}	probability of atom being in excited state
Δp	momentum broadening
Δz	spatial spreading
m	mass of atom

Chapter 3

a_n, b_n	electric field amplitudes, $n = 1, 2, ...$
n_1	effective refractive index of guided mode/grating effective index
L_{cav}	physical length of cavity between mirrors
k_0	freespace wavenumber
w_0	beam spot size
r	beam radius
Z	grating length/thickness of dielectric mirror

r_i	reflection coefficients, $i = 12, 21, etc.$
t_i	transmission coefficients, $i = 12, 21, etc.$
r	reflection coefficient of mirror/grating
t	transmission coefficient of mirror/grating
R	mirror/grating reflectivity
T	mirror/grating transmission
L	mirror/grating loss
r_c	cavity reflection coefficient
t_c	cavity transmission coefficient
ϕ	roundtrip phase shift
φ_r	mirror phase shift in reflection
ϕ'	roundtrip phase shift incorporating reflective phase shift of mirror
T_c	cavity transmission
$\mathcal{F}$	coefficient of finesse
τ	resonant cavity transmission (throughput)
γ	Lorentzian half-width
F	cavity finesse
λ_B	Bragg wavelength
δn_1	effective variation in refractive index
Λ	grating period
α	grating loss per unit length
$n(z)$	refractive index of grating
β	propagation constant in absence of grating
β_B	propagation constant at Bragg wavelength
$k(z)$	propagation constant in fibre (complex)
$E(z)$	electric field amplitude
$A(z), a(z)$	amplitude of mode in positive z-direction
$B(z), b(z)$	amplitude of mode in negative z-direction
Δ	detuning parameter (complex)
δ	wavelength detuning
κ	grating coupling coefficient
z_i	grating boundary positions, $i = 1, 2$
E_+	positive z-direction travelling field
E_-	negative z-direction travelling field
λ	freespace wavelength
$E_\parallel$	tangential component of electric field
$H_\parallel$	tangential component of magnetic intensity
d_H	physical thickness of high index dielectric layer

d_L	physical thickness of low index dielectric layer
τ_r	grating reflection delay time
L_e	grating penetration depth
B_λ	grating bandwidth
$A_\pm(r)$	complex Gaussian envelopes
$w(z)$	beam radius ($1/e^2$)
z_0	Rayleigh range
$\eta(z)$	Guoy phase shift

Chapter 5

ΔL	error in grating loss
ΔT	error in grating transmission
$\Delta\tau$	error in cavity resonant transmission (throughput)
ΔF	error in finesse
$\Delta\lambda$	wavelength separation due to grating stretching
$\lambda_{\max}$	wavelength of maximum reflectivity

Chapter 6

ϵ	cavity figure of merit
L_{gap}	single pass loss due to gap in fibre cavity
t	time
θ, A	temperature dependent parameters

Chapter 7

Γ	FWHM of resonance
t_{FSR}	time taken to scan across one FSR
t_Γ	time taken to scan across cavity linewidth
$L_1(t)$	Lorentzian function (cavity response)
A	area of Lorentzian
f_{det}	detector system response function
τ_c	detection system time constant
t_{det}	detection broadening time
$L_{1,\text{meas}}(t)$	measured Lorenzian function (fit to measured response)
t_{delay}	equipment induced time delay
Γ_{meas}	measured cavity linewidth
Γ_{det}	detection broadening factor (full width of Lorentzian)
a_{res}	amplitude of resonance
$a_{\text{res,meas}}$	measured amplitude of resonance

ν_s	sweep frequency
F_{real}	finesse in the absence of detector or laser broadening
τ_{real}	throughput in the absence of detector or laser broadening
Γ_{laser}	laser linewidth
t_{laser}	laser broadening time

Chapter 8

a_c	fibre core radius
λ_{cutoff}	cut-off wavelength of fibre
κ_{gap}	gap loss rate
η	coupling between fibres
β	fibre cleave angle
θ	angle between incident light and fibre axis
p_e	photoelastic constant
ϵ	strain
P_{11}, P_{12}, μ	strain tensor coefficients

Chapter 9

Ω_{S}	solid angle subtended by collection fibre's core
α	half angle subtended by fibre core
W_f	power collected by fibre

Chapter 1

Introduction and Background

This chapter contains the background and motivation for the work in this thesis. After the introduction of the atom chip, a brief overview of various fibre optic sensing techniques is given. General atom detection methods are discussed, leading onto more specific methods relating to the atom chip. The final part of the chapter gives a summary of the work presented in the thesis.

1.1 Laser cooling and trapping, and the atom chip

It is possible to use laser light to change the velocity of atoms, thus cooling them [1–4]. The use of radiation pressure to accelerate and trap particles, pioneered by Ashkin [5–7], was extended to neutral atoms [8]. The first experiments involving the deflection of atomic beams by laser light [9] led onto three-dimensional cooling, forming an optical molasses, where the temperature of alkali atoms was lowered to tens of microkelvin. The use of optical forces to trap atoms was enhanced by the addition of magnetic confinement forming a magneto-optical trap (MOT)[10] enabling researchers to trap and hold a cold cloud of atoms for long periods of time for use in atom optic experiments. Advancement in all optical trapping was also continued however, and the development of far-off-resonance trapping [11] techniques allowed full control of the internal degrees of freedom of the atoms [12]. By utilising a further process of forced evaporative cooling, the production of a Bose-Einstein condensate was also made possible [13–16].

The growing need to miniaturize and integrate matter wave optics resulted in

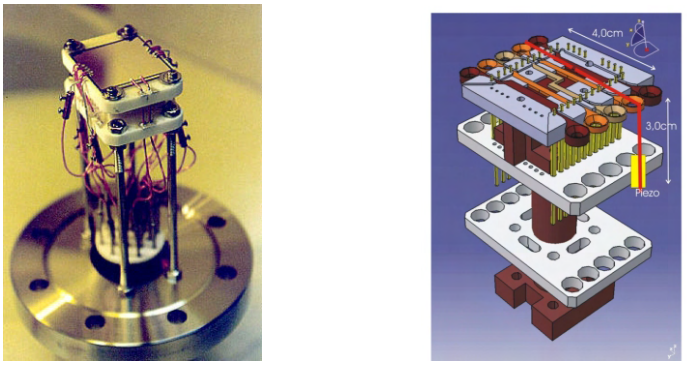

FIGURE 1.1: Atom chip from Heidelberg. (a) chip showing gold substrate; (b), schematic showing underlying wires used for loading and trapping atoms, with fibre cavity position shown in red. Atom guiding wires are etched into the gold surface. (Pictures courtesy of Heidelberg Atom Chip group).

the "atom chip"[17–20], a device engineered to guide and manipulate ultra-cold neutral atoms. The atoms are held and transported within the magnetic potentials created by the chip's current carrying wires, with further interaction possible using permanent magnetic elements [21]. The device marries the high precision available using modern nanofabrication techniques with the large body of knowledge associated with quantum and atom optics. It is believed that these devices will lead to major technological advancement in frequency standards, lithography, spectroscopy, gravitational and rotational sensing, and quantum information processing (QIP) or computing[18, 22–26]. Various configurations of atom chips have been produced by a number of research groups around the world, examples of which, from Heidelberg, are shown in Figure 1.1. It is believed that the miniaturization of atom optical elements will lead to the same type of gains enjoyed by the electronics industry. Small substrate mounted opto-magnetic traps have enabled researchers to produce Bose-Einstein condensates with much simpler equipment and at a much faster rate than was previously possible[19, 27]. A combination of various current carrying wires and passive magnetic components has allowed the construction of atom optical devices such as traps, guides, beam splitters and atomic mirrors [28–31].

Further development in this field requires further integration of the atom optical elements and the integration of light optics. For the most part, macro-scale optical components have been used to deliver the optical field necessary for coherent atom state manipulation and atomic investigation[32, 33]. Optical fibres present an ideal first step toward the introduction of micro-optical replacements for these

components due to their low loss and tight optical confinement. This thesis concentrates on the optical detection of atoms on a chip, specifically the construction, characterisation and theory of fibre gap cavities, and simple fluorescence schemes for the detection of single atoms.

1.2 Fibre optic sensors

The use of fibre optical sensors for biological, chemical or environmental sensing [34, 35] has gained widespread acceptance, with fibre optical technology offering several advantages over free space optics. Additionally, the use of optical fibre encompasses direct communication to, and from, the sensor/sensing region. This communication is immune from electrical interference and therefore offers an extra benefit over conventional wired sensors. Furthermore, the small diameter and light weight of optical fibres allows for the construction of small, compact, low volume devices. For these reasons, the implementation of fibre based optical devices onto the atom chip is highly desirable.

Fibre optical sensors can be broadly separated into two different types: intrinsic and extrinsic detectors. In the case of an intrinsic sensor, environmental information is impressed on the optical field whilst light is guided by the fibre. This can be achieved by the physical deformation of the fibre itself via temperature, pressure, strain or rotation, causing a change in optical phase and/or intensity in the signal. Here the signal can result from backscatter, such as the Rayleigh scattering used in optical time delay reflectometry, Raman or Brillouin scattering, or from a reflector or an array of reflectors. This type of technology allows for distributive sensing on a large scale. Extrinsic sensors, on the other hand, consist of a measurement "region" external to the fibre where information is imprinted upon the light field which is then coupled back into the fibre system. This signal can be encoded via intensity, phase, polarisation or frequency. The simplest type of such a detector would be a vibrational sensor based on an air gap between two fibres. Any change in alignment between the two fibres' ends would cause a change in intensity of the transmitted light. The use of external mirrors to couple light back into a fibre, or fibres, gives the potential for positional or displacement sensing, with the mirror connected to the object in question, or to measure pressure change.

The development of interferometric methods increased sensitivity and allowed for the measurement of weak physical fields. The areas of underwater acoustic sensing [36, 37] and rotational sensing [38, 39] were some of the first to benefit from this

fibre sensor technology. In an interferometric sensor phase information is converted to amplitude change which can be measured with a photo-detector. A great deal of early work focussed on the Fabry-Perot (FP) configuration and its use became widespread in the sensor industry. Early experiments using the reflection of cleaved fibre air gaps, or from the butt coupling of uncoated and metal coated fibre, led to the development of a fusion splicing method by Lee and Taylor [40] which entailed coating the end of one of the fibres with titanium oxide. This allowed the realisation of a multiplexed temperature sensor containing two FP sensors. Further work by this group led to multilayer TiO_2/SiO_2 internal mirrors using the fusion splicing technique leading to embedded temperature and ultrasound sensors [41, 42].

Much progress on the use of fibre FPs with bonded mirrors was also made by Stone, Marcuse, and Stulz, the application of which concerned filters for optical communication systems [43–47]. Furthermore extrinsic FPs were also developed for structural monitoring, with the FP formed by the faces of the two fibres within an alignment tube.

1.2.1 Fibre Bragg grating sensors

The invention and development of fibre Bragg gratings [48, 49] ushered in a new era of fibre sensing. The photo-imprinting of gratings allowed for the possibility of arrays working at different wavelengths, which were easy to produce and intrinsically robust. Furthermore, their distributive nature allowed the response of the reflector itself, either in transmission or reflection, to be used to modulate the signal. In this respect the Bragg wavelength exhibits a dependence on both strain and temperature: strain induces both a photoelastic index change and also a change in grating pitch, whilst temperature induces a change in refractive index and also thermal expansion, again causing a change in grating pitch. Additionally it was also possible to use fibre gratings in a FP configuration either as the sensing element itself, or as a scanning filter used to interrogate an array of gratings with different Bragg wavelengths. Various configurations of these filters have been used either intrinsically [50] or extrinsically [51].

1.3 Atom detection

The methods for atomic detection vary considerably within the scientific community, depending on purpose. For instance, in the case of relatively large clouds of atoms, such as a Bose-Einstein condensate that may be several tens of micrometres in diameter, absorption imaging can be used, whereby resonant light is scattered out of a probe beam and the decrease in intensity is measured by focusing the shadow onto a CCD device [52]. More information can be gathered by using more complex techniques such as phase contrast imaging [53] or polarisation (phase contrast) contrast imaging [54]. However for smaller numbers of atoms, various experimental methods have been devised. These can be broadly separated into two categories: optically prepared but not optically detected, and optically prepared with optical detection.

The non-optical detection schemes are all destructive, in the sense that although an atom is detected, the atom is lost and cannot be further manipulated. These methods include hot wire thermal ionisation or low voltage field ionisation, using close packed nanotubes [55, 56] or a single walled carbon nanotube[57]. After each of these ionisation methods, the detection event is registered using conventional ion detection.

The optical detection of atoms, on the other hand, offers minimal destruction to cold atoms. Numerous methods and schemes have been used, or are in use. These include spatial heterodyne imaging [58], frequency modulation spectroscopy [59], offset Sagnac interferometry [60], dipole blockade mechanisms, near field imaging, optical fluorescence imaging, or single photon optical traps (SPOT) [61]. Fabry-Perot cavities are routinely used [62–66] to trap, detect, or cool atoms in QED experiments, or to generate single photons. Various other cavity detection schemes have also been proposed, or are in use, including the use of photonic bandgap cavities [67], high-Q multimode cavities [68], and ring resonators. In the case of single atoms, their presence has been inferred statistically whilst the atoms are falling through a high finesse cavity [69, 70], or launched from an atomic fountain [71]. The Caltech[1] group of H. J. Kimble and the MPQ[2] group of G. Rempe are responsible for much work in this area and have also published experimental results pertaining to atomic positional information and dynamics within the cavities [71, 72]. In addition to detecting atoms falling through a cavity, Haase et al. [32] have

[1] California Institute of Technology
[2] Max-Planck-Institut für Quantenoptik, Garching

also shown that it is possible to detect magnetically guided atoms with a moderate finesse macroscopic cavity, a progression towards the integration of cavities on atom chips.

Considering methods more specific to the atom chip, single pass detection of several hundreds of atoms has been achieved [30] using fibres with semi-hemispherical lenses, and proposals to use tapered lensed fibres for single pass detection using both resonant and off-resonant light [28] have been reported. Takamizawa et al. have introduced a miniature fluorescence detector to the atom chip [73], whilst more complex detection schemes have been constructed using plano-concave optical microcavities [28, 74] or using pyramidal micro-mirrors [75], with the additional aim of cooling and trapping of atoms. Teper et al. [33] have shown that medium-finesse macroscopic cavities can be used to detect magnetically trapped atoms via fluorescence and absorption detection, and Steinmetz et al.[76] have developed a tunable fibre gap cavity with concave dielectric mirrors on the fibre faces which has been used to detect tens of atoms.

An alternative direction that has been proposed is to couple atoms to an evanescent light field. In this case there have been proposals to utilise the whispering gallery modes of microspheres [31, 77–80], and much work has been done towards coupling to and tuning [81–84] these resonators. A similar concept concerns the use of microdisk resonators [85–90] for atom detection, and the integration of these with the atom chip has already been realised [91].

1.4 Thesis overview

The work in this thesis describes the investigation, characterisation and construction of fibre Fabry-Perot gap cavities for the aim of single atom detection on an atom chip. Unlike the previously mentioned fibre resonator schemes, here the idea is to have implanted reflectors rather than mirrors on the fibre faces. The advantages here are a small mode waist at the position of the atom, offering strong coupling to the atom, and a simple robust design which requires no active alignment. The modes are stable due to internal fibre guiding and the extended length of the cavities offer a relatively low cavity damping rate despite the diffraction loss and mode-mismatch due to the gap. Figure: 1.2 illustrates the concept. The arms of the fibre gap cavity are designed to sit each side of the wire guide on the chip so that the atoms can be directed into the gap and detected.

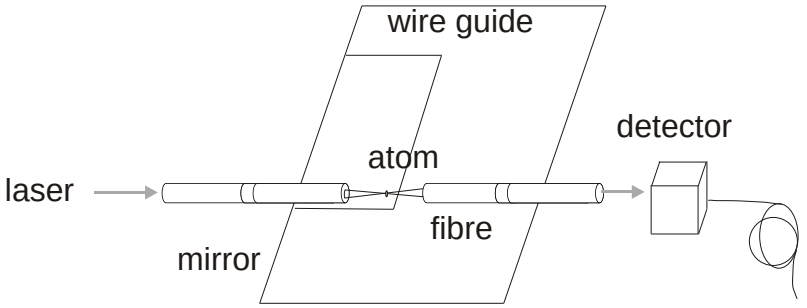

FIGURE 1.2: Schematic of a fibre gap cavity on an atom chip. The atoms are introduced into the cavity via the magnetic potentials created by the atom chip's wire guides and additional bias fields. The detection of an atom is indicated by a change in the cavity transmission.

The following chapter (Chapter: 2) describes the theory behind the fibre gap cavity detection scheme, published in a paper by Horak et al.[92]. This paper is the basis for all of the work discussed in this thesis. Both resonant and off-resonant detection are described and the merits of each are considered.

Chapter 3 is concerned with the optical theory and computational modelling of the fibre cavity itself. A matrix model is developed, and the transmission/reflection characteristics of the cavities are discussed. A derivation of the reflection and transmission coefficients for uniform Bragg gratings is given and the effect of using distributed reflectors in a fibre FP is discussed, in connection with the cavity bandwidth and free spectral range. The expressions used in the following chapters, for closed cavity and mirror characterisation, are also developed, and theoretical justification for the various mathematical fits used in the data analysis is given. The mode mismatch due to the gap is introduced, and connections with the FP detection theory are made.

Initial work on fibre gap cavities, using evaporated gold mirrors and dielectric coatings, is related in Chapter 4. Following this, "proof of principle" work with fibre Bragg gratings at 1550 nm is discussed. The favourable results gained here with these cavities paved the way for the use of Bragg gratings at the required wavelength of 780 nm.

Chapter: 5 describes fibre Bragg cavities at 780 nm. A description of both single grating characterisation and closed cavity characterisation methods is given, followed by results and analysis. The issue of grating loss is uncovered and its

possible cause is discussed. A solution to this problem, via thermal annealing, is offered in Chapter: 6. Both single grating and cavity annealing experiments are described and the results are discussed in context with atom detection.

Towards the end of 2005 a fire completely destroyed the building containing the laboratory where I carried out my work. Unfortunately all of my equipment, set-ups, experiments, cavities, samples etc., were destroyed. The position of the lab, next to the clean rooms where the fire started, meant that it was not possible to salvage anything. Although some experiments were attempted using borrowed equipment and spare corners of other people's labs, no real experimental progress could be made for about a year. This was when new temporary labs became available. Some equipment was borrowed, but new replacement equipment was obtained over time. New computer programs had to be written in order to control and extract data from these instruments and Chapter: 7 describes the new set-ups and the changes to experimental procedures necessitated by the use of this different equipment. The characterisation of new cavities, written in replacement fibre, uncovered an issue concerning detector bandwidth limitations to previous results. Since this could not be investigated directly, a set of experiments were conceived and the experimental results were used to provide the parameters for a corrective model. Comparison between the new cavities and the old cavities is then made.

Chapter: 8 gives details on fibre parameters and reconsiders the effects of the introduction of a gap in a fibre Fabry-Perot, specifically from an experimental or engineering point of view. In this chapter mounting schemes and experiments are discussed, and it is shown that it is possible to mount a fibre gap cavity, containing integrated Bragg reflectors, which would provide the fidelity to detect single atoms. The chapter concludes with a consideration of the tuning of the gratings and cavity locking.

Chapter: 9 describes an alternative direction for on-chip atom detection. Early in my PhD, work was carried out in parallel on a fluorescence detection scheme, and the experimental work concerning this is discussed. Unfortunately work in this direction was curtailed due to the fire, after which my efforts were directed solely towards the fibre cavities. However, progress by collaborators and groups within the cold atom community has been made and this is remarked upon at the end of the chapter. The thesis is concluded in Chapter: 10 with a summary of my work and a discussion of future improvements or directions which could be taken in order to construct a detector for the atom chip.

Chapter 2

Fibre Fabry-Perot Detection Theory

The use of an optical cavity to enhance atom-light interactions is a well known technique, with the Fabry-Perot (FP) resonator being the workhorse of cavity QED experiments. For atom detection, cavities offer many advantages over a simple fluorescence scheme. In a cavity the photons are recycled and each photon has a much greater probability of interacting with the atom; the higher the finesse of the cavity, the greater the probability of interaction. Also, due to the standing wave nature of the interaction field, the atom will not undergo any net radiation pressure force in the direction of the light propagation, so there is a lower probability of evicting the atom from the interaction region. In general it will be possible to detect the atom with much less disturbance since the detection method generates far fewer scattered photons. This chapter describes the cavity detection theory published by Horak et al.[92], considering both resonant and off-resonant detection, and compares the merits of both methods.

2.1 Model

The coherent coupling of the atom to the radiation field, indicated by g in Fig.2.1, is directly proportional to both the amplitude of the electric field at the position of the atom, and the dipole moment of the atom, which is small. In order to increase g it is therefore necessary to increase the amplitude of the electric field at the atom, which can be achieved by using a cavity. Fibre FPs several centimetres long have been suggested for atom detection on atom chips, and it has been shown

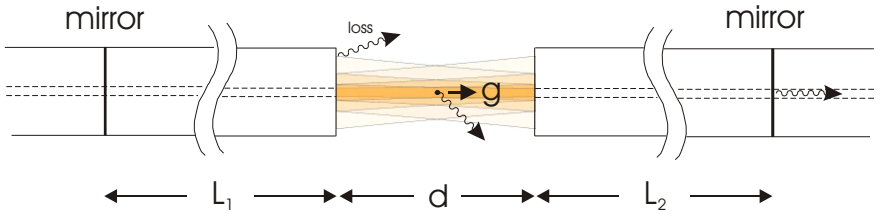

FIGURE 2.1: Fibre gap cavity model. The two implanted mirrors are separated by a distance $L_{cav} = L_1 + L_2 + d$, where L_1 and L_2 are the lengths of the fibre arms, and d is the width of the gap. The cavity decay rate, $\kappa_c = \kappa_T + \kappa_{loss}$, where κ_T and κ_{loss} represent the rate of loss through the cavity mirrors, and the rate of loss via other mechanisms, respectively. The single-photon Rabi frequency, g, represents the coherent coupling between the cavity field and the atom, whilst γ characterises the cavity damping due to spontaneous scattering from the atom.

theoretically that single atom detection is possible using a fibre resonator with a relatively modest finesse ($F \sim 100$)[92]. The finesse being a measure of the sharpness of the resonator's transmission fringes (see Subsection: 3.1.4). This sensitivity is possible due to the strong coupling between the atom and the cavity field afforded by the small radiation mode waist at the position of the atom (~ 2 µm), since g is inversely proportional to this mode waist.

For a two state atom and assuming a coherent light field with amplitude, α, with a cavity pump rate $\eta = \sqrt{p_{in}\kappa_T}$, where p_{in} is the rate of incident photons and κ_T is the rate of photon decay through the cavity mirrors, the Hamiltonian for the system can be written as

$$\begin{aligned} H &= H_{\text{atom}} + H_{\text{light}} + H_{\text{interaction}} + H_{\text{pump}} \\ &= \Delta_a \sigma_+ \sigma_- + \Delta_c a^\dagger a + jg\left(\sigma_+ a - \sigma_- a^\dagger\right) + j\eta\left(a^\dagger - a\right) \end{aligned} \tag{2.1}$$

in a frame rotating at the frequency of the pump and using both the rotating wave and electric dipole approximations. Here Δ_a and Δ_c are the respective atomic and cavity detunings, σ_+ and σ_- are the atomic raising and lowering operators, and $a^\dagger$ and a are the mode creation and annihilation operators. Also we ignore atomic motion and let $\hbar = 1$.

Using density operator formalism, the atom cavity system can be written as

$$\frac{d\rho}{dt} = \mathcal{L}\rho \tag{2.2}$$

where the evolution operator $\mathcal{L}$ incorporates both a commutator, $[H, \rho]$, containing the Hamiltonian given by Equation: 2.1, and collapse operators describing cavity leakage and spontaneous emission by the atom. Assuming the density operator to be factorised such that $\rho = \rho_{\text{atom}} \otimes \rho_{\text{light}}$, then the equations of motion for the system can be obtained from the reduced density operator relations

$$\dot{\rho}_{\text{light}} = tr_a \{\dot{\rho}\} \quad \text{and} \quad \dot{\rho}_{\text{atom}} = tr_l \{\dot{\rho}\} \ , \tag{2.3}$$

with tr_a and tr_l representing taking the traces with respect to the atom and light respectively. By solving the equations of motion the stationary state solution for α can be found to be [92]

$$\alpha = \frac{\eta}{(\kappa_c + \gamma) - j(\Delta_c - U)} \ , \tag{2.4}$$

where γ represents cavity damping due to the spontaneous scattering from the atom:

$$\gamma = \frac{g^2 \Gamma}{\Delta_a^2 + \Gamma^2 + 2g^2 N} \tag{2.5}$$

and $-U$, additional cavity detuning due to coherent scattering:

$$U = \frac{g^2 \Delta_a}{\Delta_a^2 + \Gamma^2 + 2g^2 N} \ . \tag{2.6}$$

$N = |\alpha|^2$ is the mean photon number in the cavity, 2Γ is the decay rate for the excited atom, and $2\kappa_c$ is the rate of intensity loss from the cavity.

The atoms are to be introduced into the cavity via a gap in the fibre cavity (see Fig. 2.1), and a change in the intensity or phase of the light output from the cavity due to the presence of an atom will be detected by direct or homodyne measurement, respectively. The atoms are to be guided through this gap within the potential well produced by guiding wires on the chip. This well can be considered to be harmonic, and the displacement from the centre of the trap is dependent on the trap depth, trap frequency, atomic temperature and atomic mass. To allow for variations in these, and the possibility of detecting other atomic species, a working gap size of around 5 µm has been decided upon.

The mean velocity of the atoms trapped on the chip is of the order of 1 $\text{cm}\,\text{s}^{-1}$, at a temperature of 1 µK, meaning that they would cross the cavity mode waist in around 300 µs. However it can be shown that heating effects due to the random recoil caused by spontaneously scattered photons can substantially reduce this time. Therefore a reasonable estimate for the atom detection time, τ, would be

of the order of 10 µs. This would also cover the case where the cavity could be tested by dropping the atoms through the gap under gravity from a distance of a couple of millimetres.

Two defining parameters of the atom-cavity system are the cooperativity parameter, the ratio of the damping due to the atom to the intrinsic damping of the cavity, $g^2/(\Gamma\kappa_c)$, and the atomic saturation, $2g^2N/\Gamma^2$. The cooperativity parameter can be written as [92]

$$\frac{g^2}{\Gamma\kappa_c} = 2\frac{\sigma_a}{A}n_{\mathrm{rt}} \tag{2.7}$$

where the resonant scattering cross-section for the atom $\sigma_a = 3\lambda^2/(2\pi)$, and A is the cross-section of the cavity mode. Here the cavity decay rate, κ_c, is such that

$$\kappa_c = \kappa_T + \kappa_{\mathrm{loss}} \tag{2.8}$$

where κ_{loss} accounts for photons that are lost from the cavity by other mechanisms rather than through the cavity mirrors. n_{rt} is the average number of photon round trips in the cavity. We can discuss a "good cavity limit", where $g^2/(\Gamma\kappa_c) \gg 1$ or a "bad cavity limit" for $g^2/(\Gamma\kappa_c) \ll 1$. Similarly, the extremes of atomic saturation can be defined by low saturation, when $2g^2N \ll \Gamma^2$, and high saturation for $2g^2N \gg \Gamma^2$.

Two possible methods of detection present themselves; either the laser is tuned to the atomic transition in question (in this case this is the transition from ground to first excited states in rubidium) or monochromatic light detuned from the atomic resonance is used. In the first case the detection measurement depends upon the dip in output intensity caused by the presence of an atom. In the "bad cavity limit" this is caused by photons being spontaneously scattered out of the cavity.

In the "good cavity limit" the atom shifts the cavity out of resonance with the laser, via normal-mode splitting or "vacuum Rabi splitting" [93, 94], due to the coupling between the cavity field and the atomic polarization, so that photons never enter the cavity. In principle this offers the possibility of detection without spontaneous emission. In the second case, the induced phase shift is measured by homodyne means. In both of these cases the cavity is assumed to be at resonance in the absence of an atom.

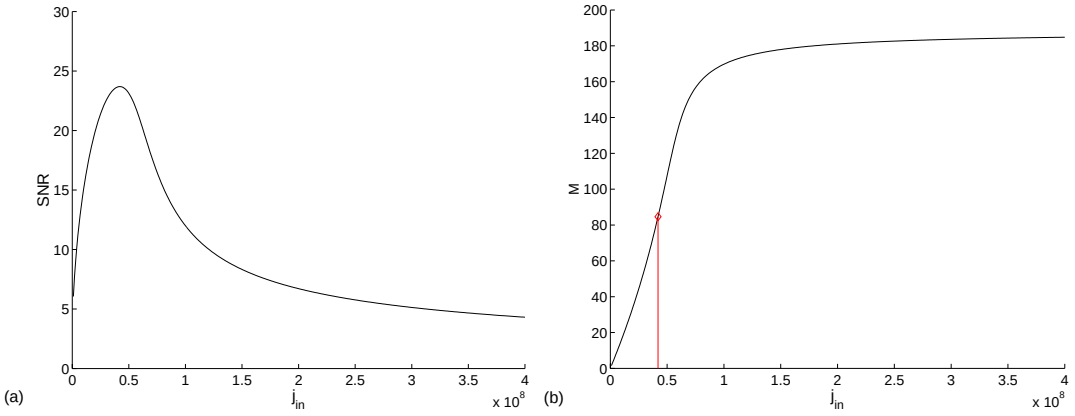

FIGURE 2.2: Single atom resonant detection example: (a) SNR; (b) number of spontaneously scattered photons, M. Red stem indicates number of photons scattered at maximum SNR. Cavity parameters: L_{cav} = 5 cm, T = 0.01, gap size = 5 µm (resonant). Detection time is 10 µs.

2.2 Resonant atom detection

For atom detection, it is necessary to obtain a signal-to-noise ratio, SNR, greater than unity where[92]

$$\mathrm{SNR} = \frac{N_{out,0} - N_{out}}{\sqrt{N_{out}}} \tag{2.9}$$

where $N_{out} = N\kappa_T\tau$, is the number of photons arriving at the detector, and $N_{out,0}$ is the number of photons arriving at the detector without the presence of the atom, and the difference is compared to the uncertainty in the detection photon number. For low saturation rates, with the cavity and the atom at resonance, we find that the SNR increases with the square root of the laser power, P, (and the square root of the detection time) but increases linearly with the number of round trips, n_{rt}, in the cavity. For highly reflective mirrors (or gratings) this means that the SNR increases with cavity finesse, since the finesse is proportional to the number of round trips. The sensitivity is degraded by cavity losses, however:

$$\mathrm{SNR} \propto \sqrt{P}\, n_{\mathrm{rt}} \frac{\kappa_T}{\kappa_c} \ . \tag{2.10}$$

For high saturation it is found that there is a inverse relationship with laser intensity; the SNR decreases with the square root of the laser power since there is a limit to the atomic scattering rate. Numerical calculations [92] have shown that the optimum sensitivity is different for different values of cavity transmission close to atomic saturation. On resonance the difference signal will be very weak since the atom will saturate with a small number of photons in the cavity.

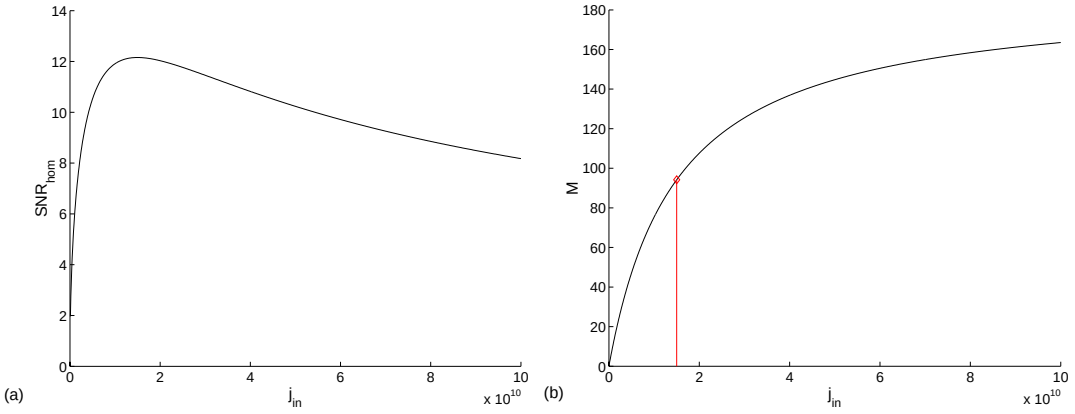

FIGURE 2.3: Single atom off-resonance detection example: (a) SNR; (b) number of spontaneously scattered photons, M. Red stem indicates number of photons scattered at maximum SNR. Cavity parameters: $L_{cav} = 5$ cm, $T = 0.01$, gap size = 5 µm (resonant), detuning = 50Γ. Detection time is 10 µs.

As an example, for a 5 cm cavity with a 5 µm gap and a mirror transmission of T=0.01, the coupling is such that $g^2/(\kappa_c\Gamma) \approx 4$, and a maximum SNR of 24 is obtained for a resonant pump with a power of about 10 pW. Here the gap is chosen to be at resonance, and the fibre parameters used are described in Subsection: 8.1.1. A numerical solution to Eq: 2.9, for these fibre parameters, is shown in Fig. 2.2(a). However, the expected signal, N_{out}, in this case is only around 10 photons for a 10 µs detection time compared to about 80 photons for a cavity without an atom. For this reason it would seem that working-off resonance with higher powers would be a better option, despite requiring a more complex homodyne detection scheme [95].

2.3 Off-resonant atom detection

The use of off-resonant light produces a phase shift due to dispersion. If we consider the case where the detuning from the atomic resonance is much greater than the natural linewidth of the atom ($\Delta_a \gg \Gamma$), then the amplitude of the light field in the cavity (Eq: 2.4) can be written as [92]

$$\alpha \approx \frac{\eta}{\kappa_c} \exp\left(-j\frac{U}{\kappa_c}\right). \tag{2.11}$$

Using a 50-50 beam splitter, the cavity output can be mixed with coherent light, of the same frequency, that has not interacted with the atom. It can be shown

[92] that the signal to noise ratio, $\mathrm{SNR}_{\mathrm{hom}}$, can be written as

$$\mathrm{SNR}_{\mathrm{hom}} \approx 2\sqrt{N_{\mathrm{out}}}\frac{|U|}{\kappa_c} \ . \tag{2.12}$$

For low atomic saturation $\mathrm{SNR}_{\mathrm{hom}}$ increases linearly with the number of cavity round trips, as in the resonant case, but is comparibly smaller for the same pump power. The situation is reversed for high atomic saturation, with the signal-to-noise ratio being higher than the resonant case for the same pump power. If we consider the same cavity, as discussed in the resonant case, then working with a detuning of 50 Γ gives a maximum SNR of 12 for a pump power of 4 nW and a resulting signal of around 30000 photons in a 10 µs window (∼1 nW). A numerical solution to Eq: 2.12 for these fibre parameters, using a detuning of 50 Γ, is shown in Fig. 2.3(a). So, the advantage of using off-resonant light is that a much larger pump power can be used, but homodyne techniques [95] are required, whereas low photon numbers are needed for a strong signal-to-noise ratio in the resonant case.

2.4 Atomic heating comparison

An important consideration for a detection event is the number, M, of photons spontaneously scattered during the measurement period, τ. These scattered photons cause atomic heating, reducing the detection time because of loss of the atom from the detection region. This scattering number can be written as [92]

$$M \equiv 2\Gamma\tau\rho_{11} \ , \tag{2.13}$$

where ρ_{11} is the probability of the atom being in an excited state. With reference to the cavity damping, γ (Eq: 2.5), we find

$$M = 2N\tau\gamma \ , \tag{2.14}$$

so M is related to the number of photons in the cavity and the effect that these cavity photons have on the atom, i.e. the coupling of the atom to the cavity field, directly affects the rate of spontaneous emission.

Let us consider the examples given previously for a cavity with equal arms of 2.5 cm (see Fig. 2.1), $T = 0.1$, and a 5 µm resonant gap. On resonance with the atomic transition, the number of photons scattered by the atom is $M = 85$ for the

maximum SNR mentioned in Subsection 2.2 (see Fig. 2.2(b)). The atom therefore scatters about eight times the number of signal photons. For the off resonant case (Subsection: 2.3) $M = 94$ for maximum $\mathrm{SNR}_{\mathrm{hom}}$ (Fig. 2.3(b)), about 0.3 % of the signal. So, for the maximum SNR in either case the number of scattered photons during the chosen detection time is similar. This can be put into context by considering a fluorescence scheme such as described in Chapter: 9 where about 2 % of scattered photons are captured by a collection fibre. In this case there are fifty times as many scattered photons as signal photons (more when photon detection efficiency is taken into account).

Horak et al. [92] discuss the momentum diffusion of an atom with respect to its position within the cavity light field, deriving spatially averaged expressions for the SNR, M, and the momentum diffusion. However, to get an approximate idea of the effect of this photon scattering we can simply consider the atom to be at an antinode of the light field, so that the momentum broadening can be given as [92]

$$\Delta p = \hbar k_0 \sqrt{M} \ , \tag{2.15}$$

leading to a spatial spreading due to a positional random walk

$$\Delta z = \frac{\Delta p}{m} \frac{\tau}{\sqrt{3}} \ , \tag{2.16}$$

where m is the mass of the atom. For the figures given in this section, $\Delta z \approx 3$ µm, about the size of the mode waist of the light in the gap, justifying the choice of $\tau = 10$ µs.

2.5 Conclusion

Using the parameters of the fibre used in this thesis work, single atom detection signal to noise ratios of up to 24 are theoretically possible for a 5 cm cavity, with mirror transmissions of 0.01 and a resonant 5 µm gap, whilst considering a 10 µs detection period. Working off-resonance, with a detuning of 50 Γ, theoretically gives a maximum SNR of 12, for homodyne detection using the same detection time. In both cases the atom spontaneously scatters about 90 photons in this time period. The advantages of the off-resonant scheme, however, would be that the maximum SNR for the off-resonant case produces a signal almost 400 times greater than for the maximum SNR on resonance since a greater pump power can be used. This would appear beneficial because, in addition to the signal shot

(photon) noise, when considering the signal detection the signal must be greater than the photodetector thermal noise and the noise generated in the amplifier used. However further investigation into each method is necessary to compare additional inherent technical noise, such as any noise generated by stabilising the fibre arms in a homodyne system.

Chapter 3

Fibre Cavities - Theory and Model

In many ways the model for a fibre Fabry-Perot (FFP) is equivalent to the plane wave model of a parallel plate Fabry-Perot (FP) with the light impinging at normal incidence. Before the gap is introduced there is no divergence of the beam since it is confined in the transverse direction. This confinement also prevents beam walk-off, a problem which occurs with bulk FP interferometers due to mirror misalignment. Before introducing the gap to the system, the fibre cavities are characterised in order to measure the properties of the reflectors, which in turn govern the properties of the cavity as a whole. In this chapter, I first introduce a closed cavity model and describe both a computational model and the theory used for experimental measurements.

3.1 Closed cavity - no gap

A schematic of the cavity model is shown in Figure: 3.1 where the electric fields in the fibre are represented by the various amplitudes a_n and b_n. Equating the magnitudes of the electric field at each side of each boundary for right and left travelling waves, a system of equations can be generated which can be represented by matrices, with the electric fields each side of the cavity related via

$$\begin{bmatrix} a_1 \\ b_1 \end{bmatrix} = \mathbf{M_1 M_2 M_3} \begin{bmatrix} a_4 \\ b_4 \end{bmatrix} \tag{3.1}$$

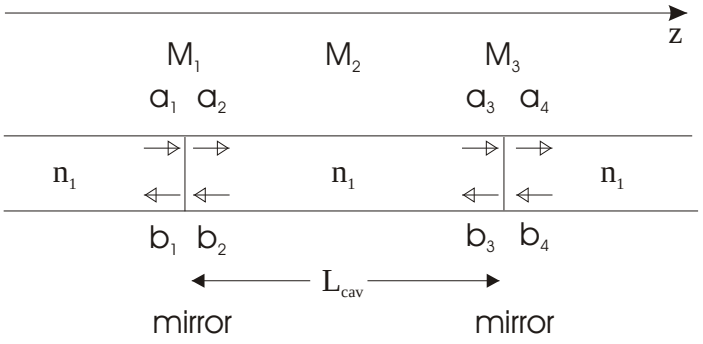

FIGURE 3.1: Schematic of closed cavity model. The amplitudes of the electric fields within the fibre are represented by a_n and b_n and are related by the matrices $\mathbf{M_i}$. L_{cav} is the total length of the cavity between the reflectors, whilst n_1 is the effective index of the fibre. The longitudinal z-axis is taken to be parallel with the fibre axis.

Here the matrices $\mathbf{M_1}$ and $\mathbf{M_3}$ are considered to be reflector or boundary matrices, with $\mathbf{M_2}$ describing the phase change due to light propagation along the resonator as discussed in the following. The mirror separation is L_{cav}.

3.1.1 Fibre propagation

Within the fibre a travelling mode can be approximated by a plane wave with a Gaussian transverse profile [96]. For light travelling in the positive and negative z-directions the spatial parts of the wavefunctions can be written as

$$U_+(r,z) = A_0 e^{-r^2/w_0^2} e^{-jn_1k_0z} \quad \text{and} \quad U_-(r,z) = A_0 e^{-r^2/w_0^2} e^{jn_1k_0z} \tag{3.2}$$

where n_1 is the effective fibre index for the mode, k_0 the free space wavenumber, w_0 the spot size, and for normalisation purposes

$$A_0 = \frac{1}{w_0}\sqrt{\frac{2}{\pi}}, \tag{3.3}$$

such that $\int dxdy|U_+|^2 = 1$. The fibre propagation matrix can therefore be defined as

$$\mathbf{M_2} = \begin{bmatrix} e^{jn_1k_0L_{\text{cav}}} & 0 \\ 0 & e^{-jn_1k_0L_{\text{cav}}} \end{bmatrix}. \tag{3.4}$$

Although it is possible to include an attenuation factor in $\mathbf{M_2}$ this is neglected here since the cavities are relatively short, $L_{\text{cav}} \sim 5$ cm, with the highest attenuation value of 19 dB km^{-1} at 780 nm, quoted for the fibre used.

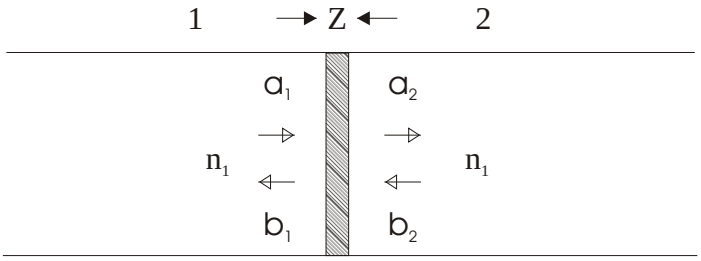

FIGURE 3.2: Generic boundary of extent, Z, between regions 1 and 2, each having a refractive index n_1. The amplitudes of the right and left travelling modes are defined by a_n and b_n respectively.

3.1.2 Boundaries and mirrors

A generic boundary can be defined which can account for metallic films, or distributed reflectors such as Bragg gratings or dielectric quarter wave stacks. This is illustrated in Fig: 3.2. The boundary occupies a physical extent, Z, which is equal to the thickness of a metallic film or the length of the distributed reflector, and the electric field amplitudes are related by

$$\begin{bmatrix} a_1 \\ b_1 \end{bmatrix} = \frac{1}{t_{12}} \begin{bmatrix} 1 & -r_{21} \\ r_{12} & -r_{12}r_{21} + t_{12}t_{21} \end{bmatrix} \begin{bmatrix} a_2 \\ b_2 \end{bmatrix} = \mathbf{M_1} \begin{bmatrix} a_2 \\ b_2 \end{bmatrix} \tag{3.5}$$

where the r's and t's are the reflection and transmission coefficients. The subscripts denote the direction of the travelling waves. These coefficients are complex, in general, possessing both a magnitude and a wavelength dependent phase,

$$r_{12} = |r_{12}|e^{j\varphi_{r_{12}}} \quad \text{and} \quad t_{12} = |t_{12}|e^{j\varphi_{t_{12}}} \quad \text{etc.},$$

where $|r_{12}| = |r_{21}|$, $|t_{12}| = |t_{21}|$, and energy conservation dictates that $R+T+L = 1$ where $R = |r_{12}|^2$ and $T = |t_{12}|^2$. The loss, L, accounts for scattering loss or absorption in dielectric films and Bragg gratings, and absorption in metallic films. Similarly, we can relate the fields either side of the other mirror, from region 2 to 3, via

$$\mathbf{M_3} = \frac{1}{t_{23}} \begin{bmatrix} 1 & -r_{32} \\ r_{23} & -r_{23}r_{32} + t_{23}t_{32} \end{bmatrix}$$

3.1.3 Cavity coefficients

Setting $b_4 = 0$ and letting $\mathbf{M_{tot}} = \mathbf{M_1 M_2 M_3}$ in Eq: 3.1 then the transmission coefficient for the cavity as a whole is given by

$$t_c = \frac{a_4}{a_1} = \frac{1}{M_{tot}^{11}} = \frac{t_{12}\, t_{23}\, e^{-j\phi/2}}{1 - r_{21}\, r_{23}\, e^{-j\phi}}\,, \tag{3.6}$$

whilst the reflection is defined by

$$r_c = \frac{b_1}{a_1} = \frac{M_{tot}^{21}}{M_{tot}^{11}} = \frac{r_{12} + r_{23}\,(-r_{12}\, r_{21} + t_{12}\, t_{21}) e^{-j\phi}}{1 - r_{21}\, r_{23}\, e^{-j\phi}}\,, \tag{3.7}$$

where the subscripts $_{23}$ and $_{32}$ describe transmission and reflection at the right hand mirror and $\phi = 2n_1 k_0 L_{cav} = 4n_1 \pi L_{cav}/\lambda_0$. For symmetrical reflectors such as Bragg gratings, metallic films, or HL dielectric films with odd numbers of layers, the phase shifts in reflection are the same in each direction for each mirror, and also in transmission, since the refractive index is the same in the input/output fibres and within the cavity. If both mirrors are assumed to be identical, these expressions take on a simpler form:

$$t_c = \frac{t^2\, e^{-j\phi/2}}{1 - r^2\, e^{-j\phi}} \quad \text{and} \quad r_c = \frac{r + r\,(-r^2 + t^2)\, e^{-j\phi}}{1 - r^2\, e^{-j\phi}}\,. \tag{3.8}$$

When considering the above expressions it can be seen that, when loss and mirror phase shift is taken into account, the transmission takes a simpler form. Furthermore, it is simpler to work in transmission because in reflection the light reflected directly from the cavity is out of phase with the light being transmitted back out of the cavity in the same direction. The intensity transmission of the cavity is such that

$$T_c = t_c t_c^* = \frac{T^2}{1 + R^2 - 2R\cos(\phi - 2\varphi_r)} \tag{3.9}$$

$$= \left(\frac{T}{1-R}\right)^2 \frac{1}{1 + \mathcal{F}\sin^2(\phi'/2)}, \tag{3.10}$$

$$= \left(\frac{T}{1-R}\right)^2 \mathcal{A}(\phi'), \tag{3.11}$$

where $\mathcal{F} = 4R/(1-R)^2$ is the coefficient of finesse [97], $\mathcal{A}(\phi')$ is the Airy function of the cavity, and the round trip phase, $\phi' = \phi - 2\varphi_r$, incorporates the reflective phase shifts of the mirrors ($\varphi_r = \arctan(\mathrm{Im}(r)/\mathrm{Re}(r))$). On resonance ($\phi' = 2m\pi$, for m= 1,2,3,....) the cavity throughput τ, i.e., the resonant cavity transmission,

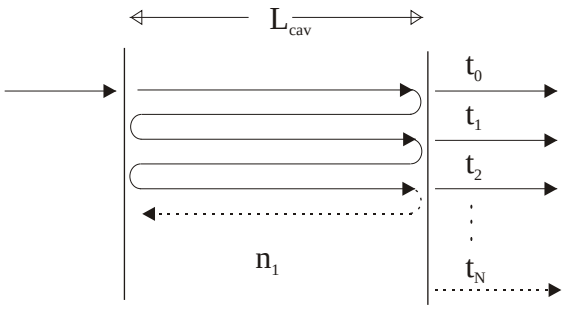

FIGURE 3.3: Summation of transmitted waves. The light transmitted through the cavity can be considered to be a summation of travelling waves which have traversed the cavity in odd numbered multiples undergoing multiple reflections.

can be written as

$$\tau = T_c|_{\phi'=2m\pi} = \frac{T^2}{(1-R)^2} = \frac{1}{(1+L/T)^2} \ , \tag{3.12}$$

where $R = |r|^2$, $T = |t|^2$, and L are the parameters for a single mirror such that R+T+L=1.

An alternative derivation of the transmission coefficient offers a different perspective on the transmission function of the Fabry-Perot, which in turn offers an experimental fit for measuring and characterising the gratings. If we consider the sum of transmitted waves which traverse the cavity in odd numbered multiples (Fig: 3.3), then

$$\begin{aligned} e^{j\theta/2}\, t_0 &= t^2 \\ e^{j\theta/2}\, t_1 &= t^2\, r^2\, e^{-j2\theta} \\ e^{j\theta/2}\, t_2 &= t^2\, r^4\, e^{-j4\theta} \\ &\vdots \\ e^{j\theta/2}\, t_N &= t^2\, r^{2N}\, e^{-j2N\theta}, \end{aligned}$$

with $\theta = 2k_0 n_1 L_{\text{cav}}$. Therefore

$$e^{j\theta/2}\, t_c = \lim_{N\to\infty} t^2 \sum_{m=0}^{N} r^{2m}\, e^{-jm\theta}$$

so that the transmitted cavity intensity, T_{cav} is such that

$$\begin{aligned} T_c &= t_c t_c^* \\ &= T^2 \sum_{m=0}^{\infty} \sum_{n=0}^{\infty} r^{2m} (r^*)^{2n} e^{-jm\theta} e^{jn\theta} \\ &= \frac{T^2}{1-R^2} \sum_{l=-\infty}^{\infty} R^{|l|} e^{jl\theta}, \end{aligned}$$

where $l = m - n$. Letting $R = e^{-\gamma}$, the product of exponentials on the right hand side becomes the characteristic function of the Cauchy (Lorentzian) distribution. The definition of the probability distribution allows us to write

$$\sum_{l=-\infty}^{\infty} e^{-\gamma|l|+jl\theta} = \int_{-\infty}^{\infty} \frac{1}{\pi} \frac{\gamma}{(\theta-\theta')^2+\gamma^2} \sum_{l=-\infty}^{\infty} e^{-jl\theta'} d\theta'$$

so that [98]

$$T_c = 2\pi \frac{T^2}{1-R^2} D_{2\pi}(\theta) * \frac{1}{\pi} \frac{\gamma}{\theta^2+\gamma^2}, \tag{3.13}$$

i.e. the cavity intensity transmission function is the convolution of a Dirac comb, consisting of a series of delta functions separated by $\theta/2\pi$, and a Lorentzian with half-width γ.

The Lorentzian nature of the resonances can also be seen from Eq: 3.10. In the vicinity of a resonance $\phi'/2 - m\pi \ll 1$ so, using the small angle approximation,

$$T_c \approx \frac{T^2}{2\sqrt{R}(1-R)} \frac{1/\sqrt{\mathcal{F}}}{(\phi'/2-m\pi)^2 + (1/\sqrt{\mathcal{F}})^2}, \tag{3.14}$$

giving a series of Lorentzian functions with FWHM of $2/\sqrt{\mathcal{F}}$ separated by π. It can be noted that Equations 3.13 and 3.14 are essentially equivalent. From Eq. 3.14

$$\tau = T_c|_{\phi'=2m\pi} = \frac{T^2}{2\sqrt{R}(1-R)} \sqrt{\mathcal{F}} = T^2 \frac{1}{(L+T)^2},$$

equivalent to Eq. 3.12, or Eq. 3.11 with the Airy function of the cavity, $\mathcal{A}(\phi') = 1$. Whereas using Eq. 3.13 we find

$$\tau = T_c|_{\theta=2m\pi} = \frac{2\,T^2}{1-R^2} \frac{1}{\gamma} = T^2 \frac{2}{(R^2-1)\ln(R)}.$$

Using the fact that $R + T + L = 1$, and since T and L are small (R is large), we

can use a Taylor expansion in $T + L$ to write

$$\tau = T^2 \left(\frac{1}{(L+T)^2} - \frac{1}{12} - \frac{L+T}{12} + \mathcal{O}\left(L+T\right)^2 \right) .$$

Furthermore, using similar expansions, we can show that the linewidths are also approximately equal: from Eq. 3.14

$$\text{FWHM} = \frac{2}{\sqrt{\mathcal{F}}} = \frac{1-R}{\sqrt{R}} = (L+T) + \frac{1}{2}(L+T)^2 + \mathcal{O}(L+T)^3 ,$$

or using Eq. 3.13

$$\text{FWHM} = 2\gamma = -2\ln(R) = 2(L+T) + (L+T)^2 + \mathcal{O}(L+T)^3 .$$

The factor of two difference here arises from the fact that Eq. 3.14 is written in terms of half of the cavity round trip, $\phi'/2$. It can also be noted that θ in Eq. 3.13 can incorporate the mirror phase shifts without any loss in generality.

3.1.4 Closed cavity finesse

An important measure of any Fabry-Perot cavity is the sharpness of the resonances, a measure typically given by the cavity Finesse, F, a ratio of the resonance fringe separation, the free spectral range (FSR), to the full width at half of the maximum (FWHM) of the resonance. From Eq. 3.13 or Eq. 3.14 we find

$$F = \frac{\pi}{\gamma} = \frac{-\pi}{\ln(R)}, \tag{3.15}$$

or

$$F = \frac{\pi\sqrt{\mathcal{F}}}{2} = \frac{\pi\sqrt{R}}{1-R} . \tag{3.16}$$

So, Eq: 3.13 shows that Lorentzian functions can be fitted to experimental data, and by measuring both the FWHM of the resonances and the cavity FSR, the finesse can be calculated. On the other hand, for small intensity transmission and loss (large R) either Eq: 3.15 or Eq: 3.16 can be expanded to give [99]

$$F = \frac{\pi}{T+L} - \frac{\pi}{2}, \tag{3.17}$$

to allow the relation of the measured value of the finesse with the cavity mirror intensity transmission and loss. Furthermore, in conjunction with Eq: 3.12, experimental measurements of the cavity throughput at resonance allow the separation

of the intensity transmission and loss, thus characterising the reflectors in question and the cavity as a whole, prior to the introduction of a gap.

3.1.5 Films and gratings

In the main, the reflectors used in this project have been distributive, either dielectric stack films or Bragg gratings. This subsection describes, theoretically, the properties of these reflectors and defines transmission and reflection coefficients which can be used in the boundary matrices introduced in Subsection 3.1.2.

3.1.5.1 Bragg gratings

The presence of a periodic perturbation (periodicity Λ) of the refractive index in the core of a single mode optical fibre couples forward and backward guided modes[100]. Despite the relatively small index change of the perturbation $\delta n_1 \sim 10^{-5}$ to 10^{-3}, the high number of periods and the phase matching at wavelengths close to the Bragg wavelength $\lambda_B = 2n_1\Lambda$, where n_1 is the effective index of the fibre, can lead to extremely high reflectivity.

The Bragg gratings considered here are uniform, and a common approximation method, involving a first order coupling coefficient, is applied to derive the reflection and transmission coefficients. The coupled mode equation approach allows the use of the amplitudes of forward and backward travelling modes, rather than the electromagnetic fields, in keeping with the model used so far. Here the derivation is approached along the lines of Finazzi and Zervas [101], although a simpler approach is considered where the amplitude loss per unit length, α, is constant along the grating. The different sign convention in Eq: 3.2 must also be noted. Letting the refractive index within the grating be

$$n(z) = n_1 + \delta n_1 \cos(2\beta_B z)\,, \tag{3.18}$$

and the propagation constant within the fibre be $k(z) = k_0\, n(z) - j\alpha$, where $\beta_B = \pi/\Lambda$, and Λ is the grating period, these functions can be substituted into the scalar wave equation

$$\frac{\partial^2 E}{\partial z^2} + k^2 E = 0 \tag{3.19}$$

along with a solution of the form

$$E(z) = A(z)\exp(-j\beta z) + B(z)\exp(j\beta z)\,, \tag{3.20}$$

where $A(z)$ and $B(z)$ are the amplitudes for modes travelling in the positive and negative z-directions respectively and β is chosen to be the propagation constant in the absence of the grating. The mode amplitudes are permitted to vary slowly, neglecting their second derivatives, the slowly varying envelope approximation (SVEA), and small perturbations, $\alpha \ll k_0\, n_1$ and $\delta n_1 \ll n_1$ are assumed. In accordance with the SVEA the rapidly varying terms in $k^2 E$ are also discarded. After defining a detuning parameter $\Delta = \beta - \beta_B = k_0\, n_1 - \beta_B - j\alpha$, and a coupling coefficient $\kappa = k_0 \delta n_1/2$, the synchronous terms are equated in order to arrive at the coupled mode equations for contra-directional modes

$$\frac{\partial A(z)}{\partial z} = -j\kappa B(z) e^{-j2\Delta z} \tag{3.21}$$

$$\frac{\partial B(z)}{\partial z} = j\kappa A(z) e^{\,j2\Delta z}\,. \tag{3.22}$$

Using the change of variables, $A(z) = a(z)\exp(j\Delta z)$, and $B(z) = b(z)\exp(-j\Delta z)$, and putting $p = \sqrt{\kappa^2 - \Delta^2}$, a solution

$$\begin{bmatrix} a(z) \\ b(z) \end{bmatrix} = C_1 \begin{bmatrix} \frac{p-j\Delta}{j\kappa} \\ 1 \end{bmatrix} e^{pz} + C_2 \begin{bmatrix} \frac{p+j\Delta}{-j\kappa} \\ 1 \end{bmatrix} e^{-pz}\,, \tag{3.23}$$

can be found for some constants C_1 and C_2, enabling the forward and backwards fields either side of the grating to be related by

$$\begin{bmatrix} E_+(z_1) \\ E_-(z_1) \end{bmatrix} = \begin{bmatrix} M_{11} & M_{12} \\ M_{21} & M_{22} \end{bmatrix} \begin{bmatrix} E_+(z_2) \\ E_-(z_2) \end{bmatrix} \tag{3.24}$$

where

$$\begin{aligned} M_{11} &= \left[\cosh\left(p(z_2 - z_1)\right) + \tfrac{j\Delta}{p}\sinh\left(p(z_2 - z_1)\right)\right] e^{j\beta_{\mathrm{B}}(z_2 - z_1)} \\ M_{12} &= j\tfrac{\kappa}{p}\sinh\left(p(z_2 - z_1)\right) e^{-j\beta_{\mathrm{B}}(z_2 + z_1)} \\ M_{21} &= -j\tfrac{\kappa}{p}\sinh\left(p(z_2 - z_1)\right) e^{j\beta_{\mathrm{B}}(z_2 + z_1)} \\ M_{22} &= \left[\cosh\left(p(z_2 - z_1)\right) - \tfrac{j\Delta}{p}\sinh\left(p(z_2 - z_1)\right)\right] e^{-j\beta_{\mathrm{B}}(z_2 - z_1)} \end{aligned} \tag{3.25}$$

and z_1 and z_2 define the positions of the grating boundaries such that $z_2 - z_1 = Z$ is the grating length. To preserve symmetry the boundary conditions $E_+(-Z/2) = 1$ and $E_-(Z/2) = 0$ are chosen, which stipulates that all reflection occurs within the

physical extent of the grating for a mode (normalised to one) initially travelling in the positive z-direction. Using Eq: 3.24 the amplitude reflection and transmission coefficients are found to be

$$r = \frac{E_-(-Z/2)}{E_+(-Z/2)} = \frac{-j\kappa \sinh(pZ)}{p\cosh(pZ) + j\Delta \sinh(pZ)} e^{-j\beta_B Z} \tag{3.26}$$

and

$$t = \frac{E_+(Z/2)}{E_+(-Z/2)} = \frac{p}{p\cosh(pZ) + j\Delta \sinh(pZ)} e^{-j\beta_B Z} \tag{3.27}$$

with

$$\Delta = \delta - j\alpha. \tag{3.28}$$

Here the detuning from the Bragg wavelength is given by

$$\delta = k_0 n_1 - \beta_B = 2n_1\pi \left(\frac{1}{\lambda} - \frac{1}{\lambda_B}\right). \tag{3.29}$$

The choice of boundary conditions allows the use of the same coefficients for a mode travelling towards the grating in the opposite direction, and enables the substitution of Eq: 3.26 and Eq: 3.27 directly into Eq: 3.5 (M_1 and M_3) for modelling purposes, or Eqs: 3.8, 3.9, and 3.12 for calculating reflection and transmission magnitudes for the cavity.

A few points need to be made here: Firstly, the background (unperturbed) refractive index of the gratings is taken to be equal to the effective index of the fibre, n_1. This can be justified since the average index of the fibre gratings is only $\sim 10^{-4}$ higher than the effective index of the fibre, so that Fresnel reflection due to this tiny discontinuity is negligible. Secondly, the range of effective index variation within the grating is $2\delta n_1$, and lastly, there is no wavelength dependence for α as we are only concerned with a narrow wavelength window. A more thorough analysis by Sipe et al.[102] and Judge et al.[103] has shown that the heuristic derivation of the coupled mode equations via the SVEA gives valid results for uniform gratings when considering weak index modulation.

After expanding Eqs. (3.26) and (3.27) to first order in α/κ, and defining the single-grating reflectivity $R = |r|^2$, transmission $T = |t|^2$, and loss $L = 1 - R - T$, κ and α can be expressed in terms of measurable quantities as

$$\tanh^2(\kappa Z) = \frac{R'}{1 - L'} \tag{3.30}$$

and

$$\frac{\alpha}{\kappa} = \frac{1}{2}L'\sqrt{\frac{1-L'}{R'}}. \tag{3.31}$$

Here, R' is the maximum reflectivity, which occurs at zero detuning $\delta = 0$ ($\lambda = \lambda_B$), and L' is the grating loss at this wavelength.

3.1.5.2 Multilayer dielectric coatings

Like Bragg gratings, dielectric quarter-wave stacks are distributive reflectors, however the index change between layers is several orders of magnitude higher, and the larger ratio of high index to low index leads to bandwidths several orders of magnitude higher than Bragg gratings. Consequently the physical number of periods and hence the physical extent of the reflector is much smaller. The use of multilayer dielectric coatings on fibres has been reported in the literature, applied by vacuum evaporation [104] or by "pull-off" films . The coating of fibre end faces, either flat or concave for micro cavities has been reported [28, 76, 105]. Here their use as integrated reflectors in FFPs is described.

The high reflectivity, and the availability of "pull-off", coatings are desirable for our purposes but the drawbacks include losses in the glue layers and the fact that light is not guided in the dielectric layers. In order to model these reflectors a simplifying assumption is made: Although the light is divergent, normal incidence is considered and the boundary conditions $E_{\|}$ and $H_{\|}$ are considered to be continuous across each layer. This assumption allows a simple relationship between the electric field amplitudes across a boundary between different refractive index layers

$$\begin{bmatrix} a_m \\ b_m \end{bmatrix} = \frac{1}{t_{\text{if}}} \begin{bmatrix} 1 & r_{\text{if}} \\ r_{\text{if}} & 1 \end{bmatrix} \begin{bmatrix} a_{m+1} \\ b_{m+1} \end{bmatrix},$$

where

$$r_{\text{if}} = \frac{n_{\text{i}} - n_{\text{f}}}{n_{\text{i}} + n_{\text{f}}} \quad \text{and} \quad t_{\text{if}} = \frac{2n_{\text{i}}}{n_{\text{i}} + n_{\text{f}}}.$$

The subscript $_{\text{if}}$ refers to the initial and final refractive indices across index change boundaries. This can be derived from the Fresnel relations and can be related to the generic boundary matrix, Eq: 3.5, by noting that there is a π phase shift in reflection when light is reflected from higher to lower index mediums or zero in the reverse direction. Energy conservation across each boundary is also assumed, allowing for further simplification. Note here that losses can be attributed to phase front and spot-size mismatch in transmission on entering the output fibre, due to the loss of guiding and any phenomenological loss due to the two glue layers.

Divergence losses due to Fabry-Perot effects within the coating are ignored.

The optical thickness of the layers are one quarter of the design wavelength, λ_0, giving a physical thickness $d_H = \lambda_0/4n_H$ and $d_L = \lambda_0/4n_L$ for high-index and low-index layers respectively, and propagation through the layers can be accounted for by using the propagation matrix, Eq: 3.4, after substituting d_H or d_L for L_{cav}. Each pair of layers, HL, can be defined with these four matrices and can be simply computed.

3.1.6 Free spectral range

The FSR of an FP is usually given in terms of measurable units such as wavelength or frequency, and often the frequency difference between successive fringes is given by FSR $= c/(2nL_{cav})$. For resonators constructed with distributed reflectors the situation is more complicated and can be treated by considering a reflection time delay or equivalent penetration depth in both fibre Bragg grating FFPs [106, 107] or FPs with dielectric mirrors [108], with this penetration depth being dependent on the strength of the grating. Here a treatment similar to that given by Barmenkov et al. [107] is considered, and any effects due to lossy gratings are taken into account. The phase velocity and group velocity are assumed to be equivalent, such that $n_1 = n_{\text{g}}$. The reflection delay time, τ_{r}, is given by [100, 109]

$$\tau_{\text{r}} = \frac{\lambda^2}{2\pi c}\frac{d\varphi_r}{d\lambda}\,, \tag{3.32}$$

giving an equivalent penetration length

$$L_{\text{e}} = \frac{c\,\tau_{\text{r}}}{2n_1} = -\frac{1}{2}\frac{d\varphi_{\text{r}}}{d\delta} \tag{3.33}$$

with

$$\varphi_{\text{r}} = \arctan\left(\frac{\text{Im}(r)}{\text{Re}(r)}\right)$$

and r and δ are given by expressions 3.26 and 3.29 respectively. Since the loss per unit length, α, is much smaller than the coupling constant, κ, around the Bragg wavelength the real part of the arguments of the hyperbolic functions in r are much greater than the imaginary parts, i.e. $\text{Re}(pZ) \gg \text{Im}(pZ)$ so, ignoring the constant phase term,

$$\varphi_{\text{r}} \approx \arctan\left(\frac{-p'\cosh(p'Z) - \alpha\sinh(p'Z)}{-\delta\sinh(p'Z)}\right) \tag{3.34}$$

with $p' = \sqrt{\kappa^2 + \alpha^2 - \delta^2}$. Considering the FSR around the Bragg wavelength, then differentiating Eq: 3.34, setting $\delta = 0$, and expanding to first order in α/κ results in an effective penetration distance

$$L_{\mathrm{e}} = \frac{1}{2\kappa}\tanh(\kappa Z) - \frac{\alpha}{2\kappa^2}\tanh^2(\kappa Z) \tag{3.35}$$

which shows that, as expected, a small α does not significantly affect the penetration distance and hence the FSR. The dispersion, $d\tau_{\mathrm{r}}/d\lambda$, of uniform Bragg gratings is zero at the Bragg wavelength [109] so the FSR can be considered uniform around this, the region of interest for a working device, giving

$$\mathrm{FSR} = \frac{c}{2n_1(L_{cav} + 2L_e)}\,. \tag{3.36}$$

The dispersion is however considerable around the band edges, so it is necessary to compute the penetration depth here if needed.

A similar result was obtained by Babic and Corzine [108] who developed a model for a Fabry-Perot using dielectric mirrors, whereby the mirrors were modelled by fixed phase mirrors each set a fixed distance L_{τ_r} into the distributed reflectors.

3.1.7 Reflector bandwidth

The reflectivity of metallic mirrors and commercial dielectric quarter wave stacks can be considered to be approximately constant over several nm, however this is not the case for highly distributed reflectors such as Bragg gratings. Due to the required mode matching conditions, the bandwidth of such gratings can be considerably smaller than the bandwidth of these other types. The wavelength bandwidth can be calculated by considering Eq. 3.26. Outside of the bandgap, the argument pZ becomes imaginary, so that $\sinh(pZ) \rightarrow \sin(|pZ|)$. Ignoring the loss per unit length, α, which has a negligible effect on the bandwidth (provided that $\alpha \ll \kappa$), we equate $|pZ|$ with π [100] and solve for δ in order to find the first zero. The bandwidth is twice this value and, in terms of wavelength, can be written as

$$B_\lambda = \frac{\lambda^2}{\pi n_1 Z}\sqrt{\kappa^2 Z^{\,2} + \pi^2} \tag{3.37}$$

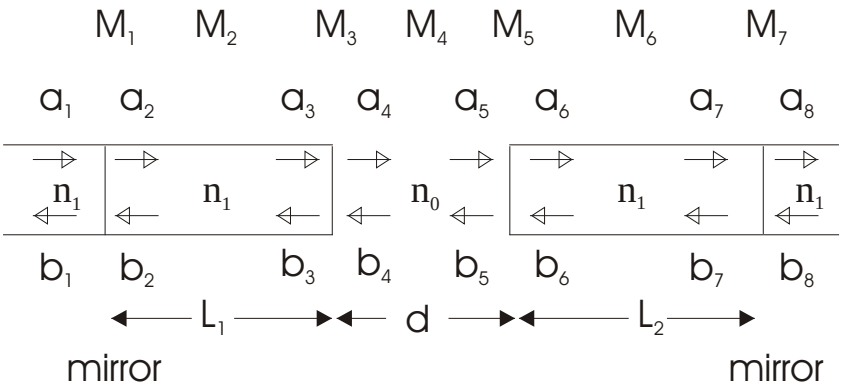

FIGURE 3.4: Gap cavity model. The total length of the cavity $L_{cav} = L_1+L_2+d$, where L_1 and L_2 are the lengths of the fibre arms, and d is the width of the gap. The amplitudes of the right and left travelling modes are defined by a_n and b_n respectively, and these amplitudes are related by the matrices $\mathbf{M_i}$. The effective refractive index of the fibre is n_1, whilst n_0 is the free space refractive index.

3.2 Gap cavity model

A schematic of the gap cavity model is shown in Figure: 3.4, with the electric fields each side of the gap cavity related via

$$\begin{bmatrix} a_1 \\ b_1 \end{bmatrix} = \mathbf{M_1 M_2 M_3 M_4 M_5 M_6 M_7} \begin{bmatrix} a_8 \\ b_8 \end{bmatrix}, \tag{3.38}$$

where $\mathbf{M_1}$ and $\mathbf{M_7}$ represent the boundary or reflector matrices, defined in Subsection 3.1.2, and $\mathbf{M_2}$ and $\mathbf{M_6}$ are fibre propagation matrices, defined in Subsection 3.1.1. The matrix product $\mathbf{M_3 M_4 M_5}$ relates the electric field amplitudes within the fibre each side of the gap and is derived in the following subsection.

3.2.1 The gap

The light in the gap is modelled as Gaussian travelling waves

$$U_{\pm}(r,z) = A_{\pm}(r,z)e^{\mp jn_0k_0z}$$

where the complex Gaussian envelopes $A_{\pm}(r)$ are defined by[95]

$$A_{+}(r,z) = \frac{A_1}{q(z)} \exp\left(\frac{-jn_0k_0r^2}{2q(z)}\right); \quad q(z) = z + jz_0.$$

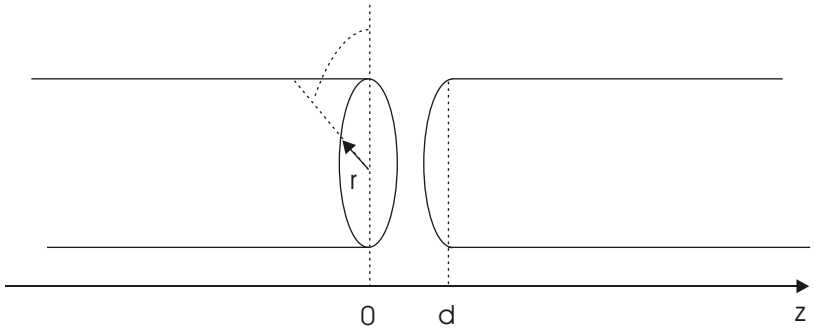

FIGURE 3.5: Overlap calculation coordinates: r, ϕ, and z are cylindrical polar coordinates with the z-axis parallel to the fibre axis. The left-hand fibre face is taken to be at $z = 0$ with the right-hand fibre face at $z = d$.

and

$$A_-(r,z) = A_+^*(r,z),$$

with $A_1 = jz_0A_0$ when normalised. There is a mode mismatch due to the diffractive nature of the Gaussian travelling wave. To calculate the coupling and losses involved, the mode overlap on entering the other fibre is calculated. Taking the zero of z to be at the left-hand fibre face (see Fig. 3.5), the coupled part of the wave, Q, is given by [92]

$$\begin{aligned} Q &= \int_0^{2\pi} d\phi \int_0^{\infty} dr\, U_+(r,z)|_{z=d}\, U_-^*(r,z-d)|_{z=d} \\ &= \int_0^{2\pi} d\phi \int_0^{\infty} dr\, U_-(r,z-d)|_{z=0}\, U_+^*(r,z)|_{z=0} \\ &= 2\pi A_1^2 e^{-jk_0d} \int_0^{\infty} dr\, \frac{1}{d+jz_0} \exp\left(\frac{-jk_0r^2}{2(d+jz_0)}\right) \frac{1}{jz_0} \exp\left(\frac{-k_0r^2}{2z_0}\right) \\ &= \frac{w_0}{w\,(d/2)} \exp\left(j\eta(d/2) - jk_0d\right) \end{aligned} \tag{3.39}$$

where

$$w(z) = w_0\sqrt{1+(z/z_0)^2}\ , \quad z_0 = \pi w_0^2/\lambda_0\ , \text{ and } \ \eta(z) = \arctan\left(z/z_0\right),$$

and $n_0 = 1$. For an electromagnetic wave impinging on a dielectric boundary (change of refractive index) at normal incidence, the boundary conditions $E_\parallel$ and $H_\parallel$ are continuous. For a single mode fibre, this is the situation for both the polarisation components of a guided mode. Across a boundary we have the following

relationship

$$\begin{bmatrix} a_m \\ b_m \end{bmatrix} = \frac{1}{t_{if}} \begin{bmatrix} 1 & r_{if} \\ r_{if} & 1 \end{bmatrix} \begin{bmatrix} a_{m+1} \\ b_{m+1} \end{bmatrix},$$

where

$$r_{if} = \frac{n_i - n_f}{n_i + n_f} \quad \text{and} \quad t_{if} = \frac{2n_i}{n_i + n_f}. \tag{3.40}$$

The subscript $_{if}$ refers to the initial and final refractive indices across index change boundaries. Therefore the gap can be modelled as the matrix product

$$\mathbf{M_3 M_4 M_5} = \frac{1}{2n_1} \begin{bmatrix} n_0 + n_1 & n_1 - n_0 \\ n_1 - n_0 & n_0 + n_1 \end{bmatrix} \begin{bmatrix} 1/Q & 0 \\ 0 & Q \end{bmatrix} \frac{1}{2n_0} \begin{bmatrix} n_0 + n_1 & n_0 - n_1 \\ n_0 - n_1 & n_0 + n_1 \end{bmatrix}.$$

It should be noted here that conservation of energy requires that $R_{\text{if}} = |r_{\text{if}}|^2$ and $T_{\text{if}} = (n_{\text{f}}/n_{\text{i}})|t_{\text{if}}|^2$ from fibre to air, or vice versa.

3.2.2 Resonance

The introduction of a gap into the cavity adds extra loss due to diffraction and mode mismatch, as mentioned above, but also changes the resonant structure of the cavity. Effectively, the fibre cavity becomes three coupled cavities. The derivation of the transmission coefficient for such a system can be carried out using a variety of methods, but applying Z-domain techniques from digital filter theory [110] allows for a tractable rational solution via Cramers rule. We find

$$t_c = \frac{t^2\, t_{12} t_{23}\, z^{-(m+n+p)}}{\left\{ \begin{array}{ll} 1 - r\, r_{12}\, (z^{-2m} & +z^{-2p} - z^{-2(m+n)} - z^{-2(n+p)}\,) \\ & -r_{12}^2\, z^{-2n} + r^2\, r_{12}^2\, z^{-2(m+p)} - r^2 z^{-2(m+n+p)} \end{array} \right\}} \tag{3.41}$$

where the solution to the optical problem is gained by substituting the phase shifts for the z-delay blocks:

$$z^{-m} \mapsto \exp(-jk_0 n_1 L_1), \;\; z^{-n} \mapsto \exp(-jk_0 n_0 d) \;\; \text{and} \;\; z^{-p} \mapsto \exp(-jk_0 n_1 L_2), \tag{3.42}$$

r and t are the grating coefficients and r_{12}, t_{12}, and t_{23} are given by the Fresnel relations (Eqs. 3.40). By comparison with the amplitude transmission given by Eq: 3.8 it can be noted that the dominant term in the denominator here relates to the total optical group length and so the average FSR is the same as in the closed cavity case, Eq. 3.36 (except for the small additional gap length). However the other terms involved mean that the FSR varies about this value. The resonance

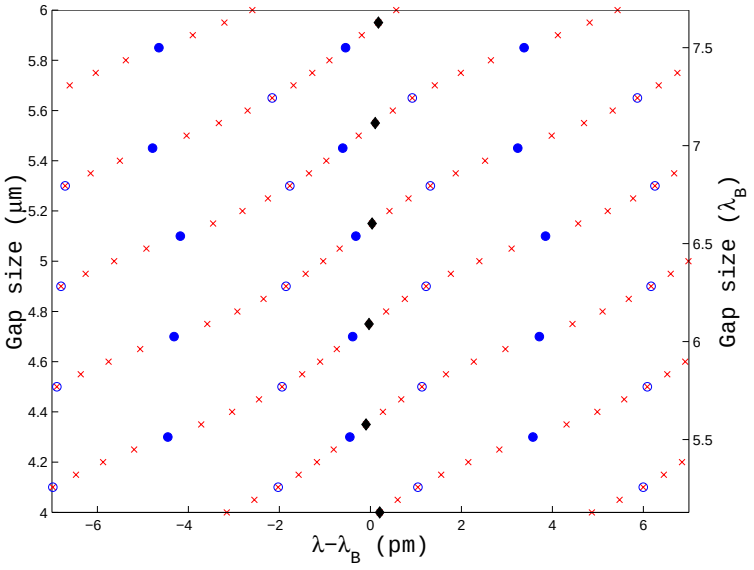

FIGURE 3.6: Resonance positions (red crosses) against gap size calculated for a cavity with a uniform arm-length of 2.5 cm and grating coupling coefficient $\kappa = 500$, λ_B=780 nm. Positions are calculated in gap size increments of 0.05 µm. Closed blue circles indicate positions with approximately uniform FSR (gap in resonance), and the open blue circles indicate maximum FSR asymmetry (gap out of resonance). Black diamonds relate to the resonance condition given by Eq. 3.43.

condition for a gap cavity with equal length arms was given by Horak et al., via a first order expansion in $d/2z_0$ [92]

$$d\left(k_0 - \frac{1}{2z_0}\right) = m\pi - 2\arctan\left[\frac{1}{n}\tan(n_1 k_0 L_1)\right]. \tag{3.43}$$

Figure: 3.6 illustrates, theoretically, how the positions of the resonance orders about the Bragg wavelength change with gap size for a cavity with equal 2.5 cm arms and 5 mm gratings, grating coupling coefficient $\kappa = 500$. The closed blue circles show positions with approximately uniform FSR which occur for multiples of $\lambda_B/2$. Between these positions, the FSR is asymmetric (open circles), with a ratio of approximately 5:3 between adjacent ranges. The black diamonds relate to the resonance condition, Eq: 3.43, for resonance near to the Bragg wavelength and for each point, the order, m, increases by one. The computed grating penetration depth is approximately 1 mm and this is included in the resonance calculation.

3.3 Connection with atom detection theory

To relate the experimental data, from cavity characterisation, to the fibre Fabry-Perot detection theory described in Chapter 2, it is necessary to relate the various time rates with the single pass losses. Now, the intensity, I, of the light field inside a cavity is such that

$$I = I_0 e^{-2\kappa_c t} \ , \tag{3.44}$$

for a cavity loss rate κ_c and time t. Considering the cavity decay as being due to leakage through the mirrors only, and ignoring any other loss for the moment, then the loss rate through each mirror is simply κ_T. The mirror transmission, T, is the product of the cavity round trip time and this loss rate, therefore

$$T = \frac{\kappa_T}{\mathrm{FSR}} \ . \tag{3.45}$$

Similarly, including other losses, we find that $L + L_{\mathrm{gap}} = \kappa_{\mathrm{loss}}/\mathrm{FSR}$, where L_{gap} is the single pass gap loss. However, as noted in the last section, once the gap is introduced into the cavity the result is three coupled cavities and the FSR is not a constant, except under certain circumstances, so it is necessary to consider an average, $\overline{\mathrm{FSR}} = c/(2n_1 L_{\mathrm{cav}})$. We can also relate the cavity loss rate to an average finesse:

$$\kappa_c = \pi \frac{\overline{\mathrm{FSR}}}{\mathrm{F}} \tag{3.46}$$

where the $\pi/2$ term from Eq. 3.17 has been omitted for brevity. In the experimental case the finesse is taken to be the average of two values calculated from the free spectral ranges each side of the resonance and the cavity linewidth.

3.4 Conclusion

A model for both closed fibre cavities and fibre gap cavities has been established, and the expressions used for cavity and grating analysis in forthcoming chapters have been developed and justified. The complexity of coupled cavity resonances has also been introduced. Finally, connections between the various time rates used in the FFP detection theory of Chapter 2 and the single pass losses introduced in this chapter were made by considering an average free spectral range.

Chapter 4

Initial Cavity Development

This chapter relates the first attempts at fibre gap cavity construction. The early use of evaporated gold coatings is followed by a description of the method of development, and the issues involved with using dielectric film reflectors. Fibre Bragg gratings, on the other hand, offer a less complex and more integral solution for an on-chip atom detection device, and a "proof of principle" is demonstrated using gratings at the wavelength of 1550 nm.

4.1 Gold coated mirrors

The first attempts at making fibre cavities entailed the use of evaporated gold mirrors. Single mode fibre was cleaved to produce 2cm lengths, with each piece being visually inspected under a microscope to check for signs of damage or angle cleaves. Only short lengths of fibre with two good faces were accepted as one side was to be coated, with the other forming one side of the gap. After a three stage cleaning process in an ultrasonic bath, the fibres were attached to a mount, constructed from microscope slides, using a soft photo resist and baked in an oven. The gold was evaporated onto the fibre ends under vacuum in an Edwards Evaporator, and the coating thickness was measured to be approximately 65 nm (the measurement was made on a plain microscope slide mounted alongside the fibres in the coating machine). A rough measure of the transmission/reflection properties of the coated fibres was gained by measuring the properties of the coated slide. At 780nm the losses were measured to be $6.2 \pm 0.8\%$ with a power reflectivity of $93.5 \pm 0.8\%$.

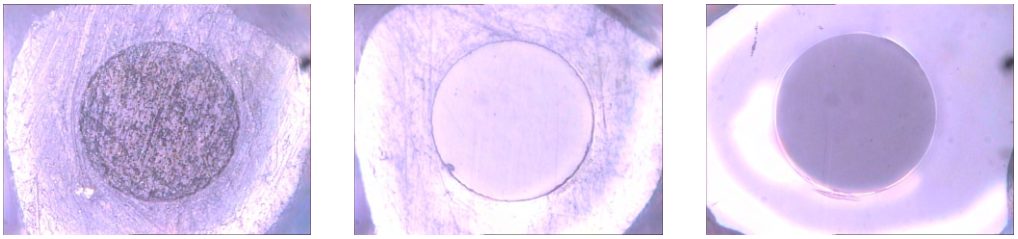

(a) (b) (c)

FIGURE 4.1: Fibre face showing the result of hand polishing with (a) 5 µm grit size paper, (b) 1 µm grit size paper, and (c) 0.05 µm grit size paper.

As an initial rule of thumb, the aim was a minimum finesse around F∼100 corresponding to a mirror reflectivity of around 98 % to 99 %, and allowing for a single pass loss of approximately 1% for a 5 µm gap, as these parameters had been shown [92] to be sufficient for single atom detection. So, although it was possible to construct gap cavities using these coated fibres, it was not possible to achieve a high enough finesse ($F > 100$) since this was limited both by the reflectivity of the mirrors, and by the losses. In fact, initial finesse measurements were only $F = 10$ to $F = 20$ for a gap cavity, when the gap was scanned using a piezo stage, however it did indicate that coated fibres may be a possible direction. The poor performance of the gold coated cavities was attributed to absorption and fibre misalignment.

4.2 Dielectric coatings

The switch to dielectric coatings for cavity construction saw a marked improvement in reflectivity, and hence finesse. The coating, was a "peel off" type manufactured by OIC (Optical Interference Components). The dielectric coating, consisting of alternate layers of quarter wavelength SiO_2 and TiO_2, is adhered to a circular glass substrate using salt. The nominal reflectance for the coatings was 98-98.5 %. The method of coating involves the preparation and mounting of the fibre, active alignment, gluing and coating transfer.

4.2.1 Preparation

Single mode fibre (SM750) was stripped and thoroughly cleaned, then cleaved, to leave about 8 mm of uncoated fibre. The cleaved face was then inspected under a microscope. Both hand-polished fibres, and plain cleaved fibres have been

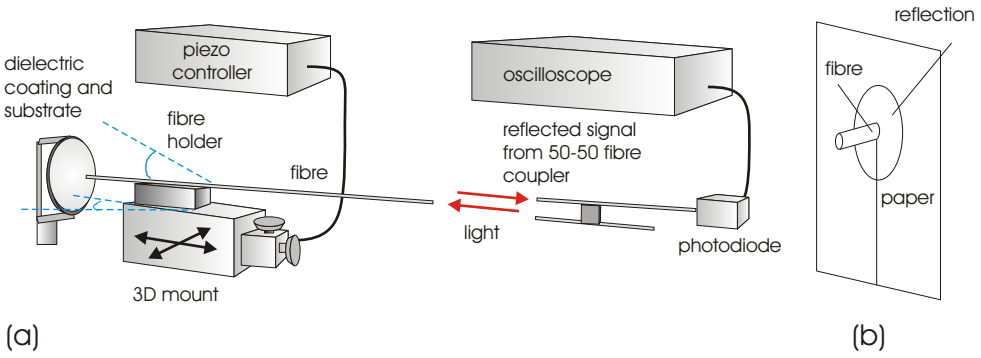

FIGURE 4.2: Dielectric coating transfer set-up. (a) Prior to gluing, the fibre end is aligned so that the fibre face and the dielectric coating substrate are parallel. This is achieved using a 3-axis stage and pitch and yaw control. The alignment of the fibre face and the substrate is monitored using the reflected signal from the cavity formed between the fibre face and the dielectric coating. (b) Initial rough alignment is achieved by monitoring the reflection on a small piece of paper positioned on the fibre.

coated, but there is insufficient data to compare the losses between these two. The hand polishing was initially carried out using a bare fibre "Bullet" adaptor and a polishing puck, gradually reducing the paper grain size down to 1 µm. Polishing was also tried with the fibre glued into a bare fibre adaptor using "superglue" and finishing with 0.05 µm grain size. Figure 4.1 shows stages from a polishing process. The fibre was extracted from the adaptor after soaking in acetone.

4.2.2 Gluing and mounting method

The fibre was threaded through an adjustable fibre holder that was mounted upon a piezo controlled 3D-mount. It was mounted so that the fibre protruded a short distance (8mm) out from the holder and the fibre was moved close to the coating substrate using manual stage controls. The substrate was positioned vertically and adjusted to be perpendicular to the direction of fibre movement. Laser light was coupled into the fibre via a 50-50 beam-splitter and the light reflected from the mirror substrate was used for rough alignment. This reflection was observed on a small piece of paper with a slit, through which the fibre passed, Fig. 4.2(b), and rough alignment to the perpendicular was attained when the beam image was centred about the fibre.

The fibre holder allowed adjustment of the pitch and yaw angles of the fibre, indicated by θ and ϕ respectively, in Fig. 4.2(a). The fine tuning was monitored by scanning the small cavity, formed between the fibre tip and the dielectric coating,

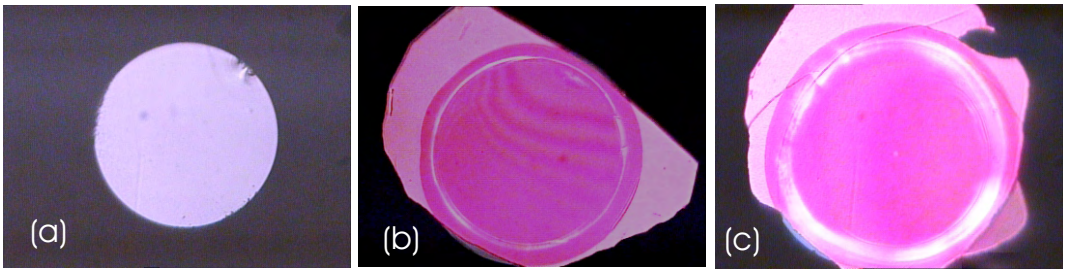

FIGURE 4.3: Dielectric coating mirrors. (a) cleaved but unpolished fibre; (b) unpolished fibre with resulting dielectric coating; (c) shows the result of coating a hand-polished fibre.

using the piezo driven stage and observing the reflected signal from the beam-splitter on an oscilloscope and the signal transmitted through the coating substrate (power meter not illustrated in diagram). The operation was monitored using two Watek CCD cameras, with extension tubes, oriented along the vertical and horizontal directions. The absolute position of the fibre was tracked by its position on the camera monitors. A trial and error method was used to optimise the fibre face position with respect to the coating substrate. The stage was scanned at 12Hz using a generated ramp voltage, producing about 1 µm of movement. Once adjustments had been made, the position on the horizontal stage micrometer was noted and the stage was backed off as far as possible (about 15mm) away from the substrate and then horizontally towards the side of the substrate. The function generator was disconnected from the piezo controller and UV glue (Norland 88 optical adhesive) was applied to the end of the fibre, using a scrap piece of fibre. Excess glue was removed by "blotting" on the side of the mirror coating (in an area unused for coating purposes) in several different places. The fibre was then returned to its original horizontal position and moved against the substrate. It was possible to judge the distance from the fibre to the substrate by reconnecting the piezo controller and "cycling" through the resonances until the distance between them appeared to change.

With the piezo off and the cameras blocked, the UV light used to cure the glue was directed both at the join itself, and also at the end of the fibre through the glass substrate and coating. The UV waveguides of the Novacure system were moved several times throughout curing and, since it was not known how much UV light passed through the substrate, the fibre-mirror join was irradiated in 40s periods with the intensity of the light source set at 4 Wcm^{-2} for a total time of 10-20 minutes. The fibre was then backed away from the substrate which removed a small portion of the dielectric coating. This was done in two stages, firstly

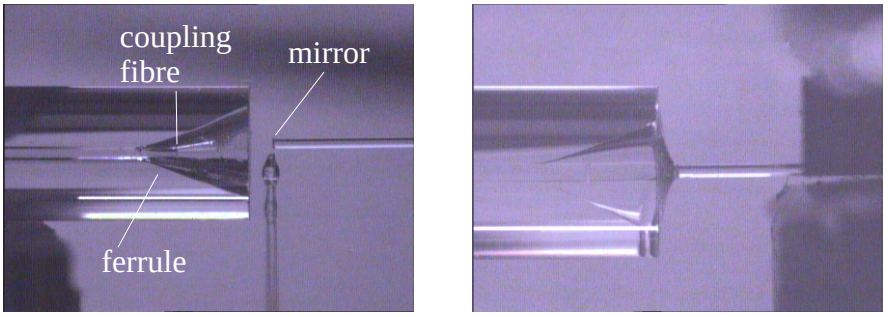

FIGURE 4.4: Dielectric cavity construction:(a) glue application and ferrule; (b) once the fibres are aligned in the ferrule the mirror is surrounded by glue which is cured using UV light.

the stage was moved a few tens of microns and left static to relax a little in the hope that the salt bonds would gradually loosen, then the stage was moved away manually. As can be seen from Figure 4.3 (b) and (c), the dielectric coating pulls off in an area that is a little larger than the area of the fibre end. Some of the excess material can be removed carefully, but care must be taken to avoid damaging the mirror surface.

The reflective coating was then washed with water to remove the salt. A visual inspection of the coating on some of the unpolished mirrors show signs of an uneven surface, an example of this is evident by the fringes seen in Fig. 4.3(b). It is also possible that hand-polishing sometimes produces a slightly convex surface, which is one explanation for image (c) in Fig. 4.3, but this may be an artefact due to the microscope lighting. Since it is the area around the fibre core which is important, in future it is proposed to lightly polish the fibres before coating transfer. To complete the cavity it is necessary to coat the other end of the fibre, and this was carried out in a similar manner, although alignment was easier since there are clear resonance peaks to aid signal monitoring.

4.2.3 Mirror protection in ferrule

Since the area of the end of a fibre is small, this type of join is very fragile and it is necessary to protect the join using a glass ferrule, as shown in Figure 4.4. This procedure was again carried out using stages and the whole of the connection, within the flange of the ferrule, was surrounded with glue. Figure 4.4 (b) shows the operation during final alignment, before the fibres were brought into contact.

There has been a problem with this method as a 4% transmission loss has been noted on the first application of UV light. This may be due to non-uniform curing of the glue and placing the UV waveguides symmetrically around the fibre may help. Closed cavities with a finesse, F$\sim$ 100, were produced and we provided our Heidelberg collaborators with one such cavity for testing purposes.

4.3 Bragg gratings

Although not a fully integrated optical solution, the fibre gap cavity is hoped to be a step towards this. Therefore the use of fibre Bragg gratings as reflectors appears to offer a more integral solution for atom detection. Compared to the dielectric mirrors and metallic coatings, the manufacture of Bragg gratings is quicker, requiring fewer steps and, in addition, there are no reflector alignment issues. Cavities made in this way are also more robust and offer more consistent characteristics. There is however one important point to consider concerning the use of these gratings: The bandwidth is considerably narrower when compared to either quarter wave stacks or metallic coated mirrors as explained in Subsection 3.1.7.

4.3.1 Second order gratings

Early trials, at our required wavelength of 780nm, were attempted using the second order reflection from gratings written for wavelengths around 1550nm. Unfortunately there were problems with consistency in both wavelength and strength and it was not possible to find a matching pair. Also, it appeared that the grating strength weakened over time and there was also a shift in wavelength, indicating the possible unsuitability of the fibre (HB800), wrong hydrogenation or incorrect writing. Breakages occurred and problems were compounded by the fact that the main laser did not tune smoothly and was not necessarily stable at the central wavelength of the grating in question. The purchase of a new Sacher external cavity diode laser eliminated this latter problem as it could be smoothly tuned from 775nm to 785nm. With the increased wavelength span of this laser it was possible also to investigate some other gratings that had been attained with central wavelengths of 774-778nm. These were type II gratings and did not appear to be suitable for our purposes, mainly because they were too strong and also they were unmatched with respect to their Bragg wavelengths.

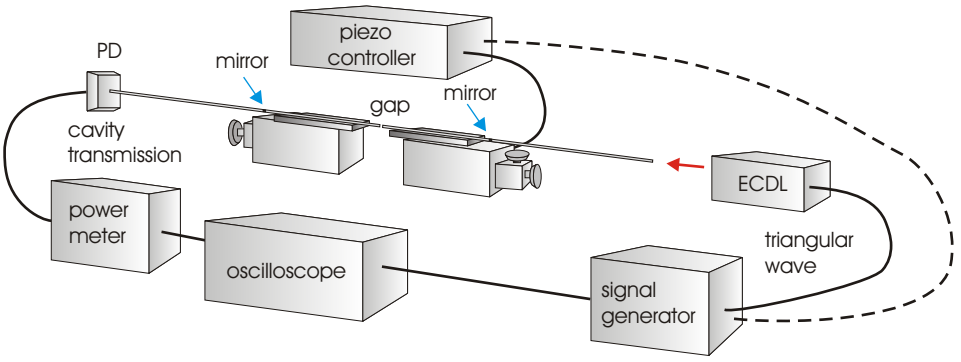

FIGURE 4.5: Equipment set-up for frequency sweep of cavity. The frequency of an external cavity diode laser is swept using a triangular wave generated by a function generator. The resulting cavity transmission spectrum is displayed on an oscilloscope. For closed cavities it is also possible to scan the cavity by stretching the fibre and keeping the laser wavelength constant.

4.3.2 1550 nm - proof of principle

In order to justify the purchase of a phase mask necessary for grating writing at 780 nm, gap cavities were constructed for tests at 1550 nm. This "proof of method" exercise entailed the writing of gratings in standard telecoms fibre. The cavities were initially analysed without a gap, then bisected and the fibre ends polished. Alignment of the fibres forming the gap cavity was carried out using a pair of three axis stages. One side used the same mounting set-up used for the dielectric coating, and the other was mounted either on a v-groove, or a rotatable fibre holder mounted on the other stage. Alignment was again carried out actively by monitoring either the reflected or transmitted signal.

4.3.3 Cavity analysis (closed cavity)

Analysis of the closed cavities was carried out by scanning the length of the cavity using a piezoelectric stretcher, or by sweeping the wavelength/frequency of an external cavity diode laser (ECDL). With the gap cavities it was necessary to either scan one arm of the cavity or to scan the laser frequency in order to have a constant gap size. A schematic diagram of the equipment set-up for frequency sweeping the cavity is shown in Fig. 4.5. It was possible to adjust the cavity gap size either manually or by using the piezoelectric control. The signal generator was connected to both an oscilloscope, in order to monitor the ramp signal produced by a triangular wave, and to the (Tunics Plus) ECDL to produce a frequency sweep about a central wavelength which was set manually on the laser control.

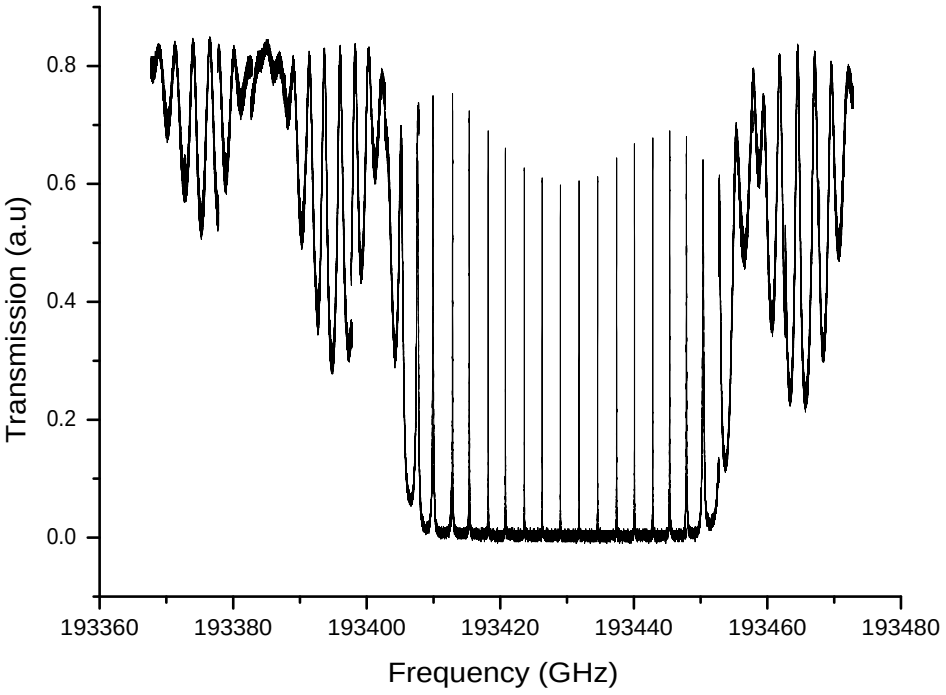

FIGURE 4.6: Frequency response of a closed cavity in 1550 nm single-mode fibre. The spectrum consists of 21 separate sweeps with their central frequencies spaced 5 GHz apart.

The transmission signal was measured using a power meter and this signal was recorded on the oscilloscope. By altering the central frequency of the scan in an incremental manner, over a chosen range, it was possible to obtain extra information about the cavity in addition to a finesse measurement. Figure 4.6 shows a stitched plot of 21 separate sweeps for a closed cavity, whose central frequencies are spaced 5GHz apart. The data was manipulated using a LabView program which initially cropped each data set so as to correspond to a single ramp (retaining 7717 points from the 10000 points recorded on each oscilloscope trace), high frequency to low. These sets were then reversed, in order to be stitched together in an increasing sequence. Each voltage ramp swept the frequency over a range slightly greater than 5GHz, so the traces had to be overlapped. By varying a scaling parameter for the frequency(oscilloscope time scale), each separate curve could be positioned a calculated distance along this axis from a datum point:

datum = central frequency of first trace
− 2.5GHz
− correction for sweep width
+ correction for voltage offset on function generator

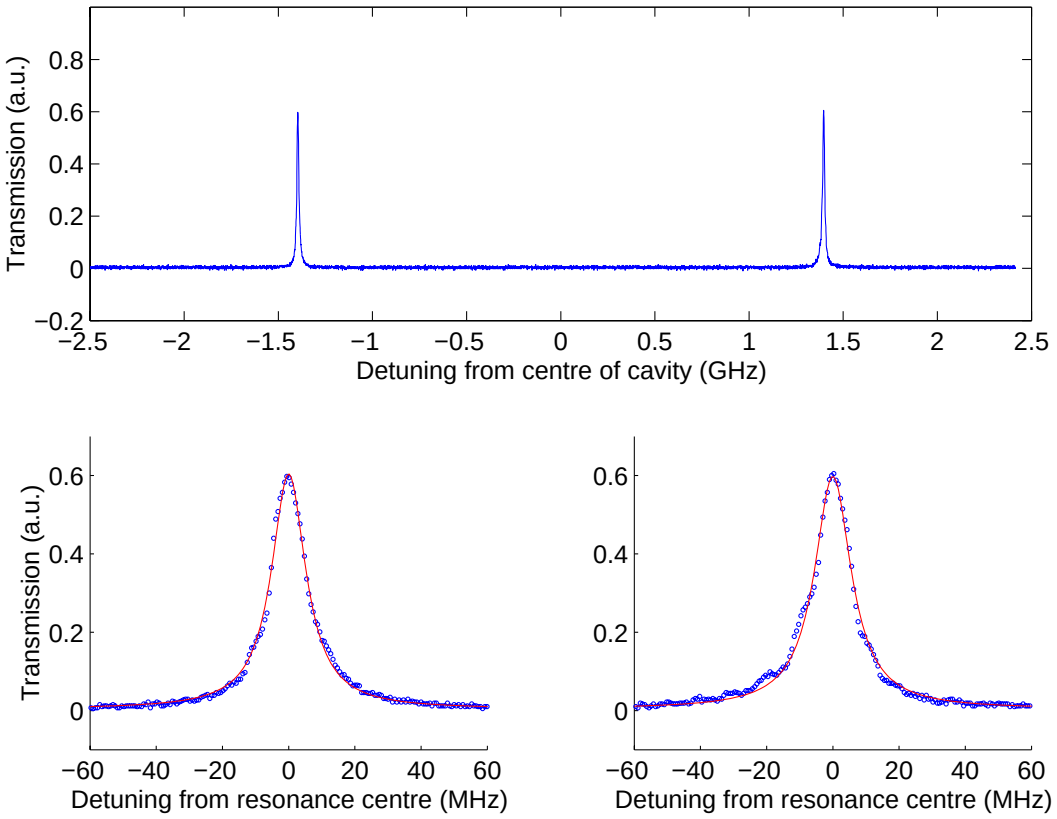

FIGURE 4.7: Central resonances of 1550 nm closed cavity, top, and Lorentzian fits to individual resonances (red), below. Measurements indicate a maximum cavity finesse of $F = 214$.

$$\text{frequency offset for each trace, data}_n = \frac{7717 \times n \times \text{ scaling parameter}}{\text{oscilloscope unit time (0.04)}}$$

$n = 0, 1...20$.

This procedure gives only a guide to the frequency scale due to uncertainty in the central frequency as read from the laser console, and the fact that the curves are fitted together by eye, however it is assumed that the span from the centre of the first trace to the centre of the last trace encompasses 100GHz. This plot then provides at least a qualitative description of the cavity transmission. The finesse measurements are relative, so there is no need for absolute values, but they can only provide snapshots of the cavity since they relate only to each separate data set and are not valid between data sets. It is assumed that there is a linear relationship between voltage and frequency for each separate trace since the frequency scan is small.

Finesse measurements from data sets within the bandwidth of the cavity were calculated by fitting Lorentzian curves to each pair of peaks, calculating the finesse using each peak in turn, then taking an average. The maximum finesse of the cavity

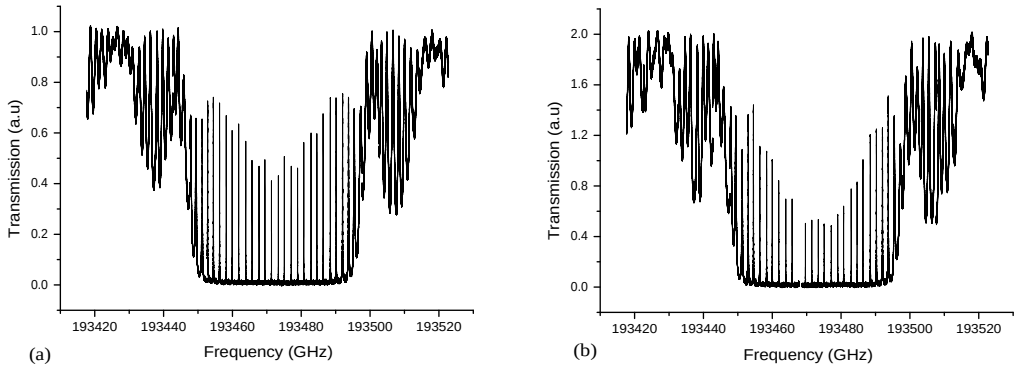

FIGURE 4.8: Frequency response for (a), a 1 µm gap cavity and (b), a 5 µm gap cavity.

occurs at the Bragg wavelength of the gratings. Figure 4.7 shows the central trace from Fig. 4.6, and the computed Lorentzian fits giving a finesse of $F = 214$ for the closed cavity. Qualitatively, a slight mismatch in the index modulation of the two gratings causes the fall off in the transmission intensities at resonances at the edges of the main bandgap (between 193410 GHz and 193450 GHz approximately) in Fig. 4.6, and the dip in the centre, about the Bragg frequency, is caused by attenuation in the fibre and loss in the gratings.

4.3.4 1550 nm with gap

With the introduction of a gap, the cavity loss is greater, as expected, which can be seen by the frequency sweeps in Figure 4.8. Graph (a) shows transmission against frequency for a 1 µm gap, whilst graph (b) shows the relationship for a 5 µm gap. Both of these graphs use the same FBGs and differ only in gap size. Although the closed cavity uses gratings from the same batch, the cavity length and hence FSR, is different. The closed cavity is also mounted on a stretcher to enable the cavity length to be swept and since this has a certain "DC" tension, the Bragg frequency is different to that of the other two sweeps. The resonant peaks in the latter two graphs do not show the same smooth modulation as that of the closed cavity, and it is thought that this is due to either gap resonances or the sampling rate, or both. A model of the cavity frequency response shows a similar effect when the number of points plotted drops below a certain threshold, and a program which models the sweeping of either a cavity arm, or the gap, shows an effect as the gap passes through resonance. Fitting Lorentzian peaks to these plots shows maximum finesses of $F = 195$ and $F = 145$, for the 1 µm and 5 µm gaps

respectively.

4.4 Conclusion

Using Figure 4.6, it is possible to get an approximate value for the throughput on resonance, τ, and using this, along with the finesse measurement (shown in Fig. 4.7), gives values for the grating transmission, $T = 0.012$, and grating loss, $L = 0.003$, via Eqs. 3.12 and 3.17. In this case, the finesse measurement for the 5 µm gap cavity and the approximate throughput value indicates an additional loss due to the gap of around 0.7 %. Using Eq: 8.4 and the FSR value from the scaled data of 2.79 GHz this would be consistent with a mode waist of about 4 µm. However, these parameters indicate a much smaller predicted single pass loss for a 1 µm gap of $L_{\text{gap}} = 3 \times 10^{-4}$, almost five times smaller than the calculated value taken from the throughput and finesse measurements for the 1 µm gap.

Since the resonant nature of the gap is not known it is not possible to directly relate the three sets of cavity measurements. Figures calculated for a resonant gap and an average FSR can only give an estimate of the loss per pass, which is dependent on the resonant condition of the gap and misalignment errors. The finesse measurements and approximate grating parameters were encouraging enough to go ahead and experiment with gratings written at 780 nm. Further analysis of the 1550 nm cavity was not carried out as this was not at the wavelength of interest, and a phase mask for writing gratings at 780 nm was ordered.

Chapter 5

Fibre Bragg Cavities at 780 nm

The results given by experiments at 1550 nm suggested that Bragg gratings were a favourable solution. Along with the intrinsic properties of robustness and manufacturing repeatability, the gratings' low loss was an additional desirable property. The acquisition of a phase mask for writing Bragg gratings at 780 nm permitted the construction of fibre cavities at the required wavelength (rubidium transition). This chapter recounts the development of the experimental methods used for characterisation of the cavities and gratings, and explains why it was necessary to change from using standard single mode fibre to a more photosensitive co-doped boron/germanium fibre. The discovery of an apparent significant loss in the gratings was thought to be a cause for concern and a discussion of the possible loss mechanism finalises this chapter.

5.1 Gratings written in SM750 fibre

On acquiring a phase mask (period = 267.5 nm) for writing Bragg gratings at 780 nm, four pairs of 5 mm gratings were side-written into standard single mode fibre (Fibercore SM750). Two pairs were written with writing speeds of 100 µm s^{-1}, and the other two pairs at 200 µm s^{-1}. The writing laser had a power output of 100 mW at a wavelength of 244 nm. To increase photosensitivity, the fibre had been hydrogenated under 150 atmospheres of pressure at 70° C for 2 weeks.

A cavity, consisting of gratings written at each speed, was investigated by both scanning the laser frequency and scanning the cavity length by stretching the fibre between the gratings. Similar results were obtained using each method. The

measured finesses were around 70 for the weaker gratings, and 150 for the stronger pair. However, from the very first measurements of the initial cavities it was noted that their throughput was extremely low (∼1.5 %) when compared to the 1550 nm cavities. When the peak to peak voltage of the ramp used to scan the laser was reduced so that the frequency range covered only one resonance, compared to the two FSR used for a finesse measurement, there was no clear difference in the amplitude of the resonances when scanned at the same speed. Therefore the small throughput was not judged to be due to any speed limitations of the detector used (Thorlabs DET 110). It appeared that there was some extraneous loss in the gratings written at 780 nm.

5.1.1 Single grating characterisation

A first series of single grating experiments was carried out with the aim of directly quantifying the apparent grating losses. The higher finesse cavity was bisected and, using a 50/50 fibre coupler, the transmission and reflection signals from one of the gratings were measured, in addition to the throughput from the other output leg of the coupler. Allowing for the insertion loss of the coupler (manufacturer's figures), the splitting of the reflection signal, and allowing for approximate insertion losses for the various fibre splices, loss measurements of the order of 10 % were calculated. These figures were too high for agreement with the throughput and finesse measurements calculated previously, for example using Eqs: 3.12 and 3.17, a finesse of F=150 and throughput of 1.5 %, gives a calculated figure of the order of 2 % for the grating loss. Although the same detector was used for each of the measurements and the signals were normalized to allow for a drift in power over time, there was a large uncertainty in the splice losses, insertion losses due to fibre pigtail mismatching, and coupling to the detector. An alternative method for accurately measuring the grating loss was required.

In order to have confidence in the loss measurements calculated via cavity measurements, it was necessary to verify at least one other grating parameter using a different experimental set-up. If the grating transmission was accurately measured, and this agreed with the transmission calculated from closed cavity measurements, then a high confidence could be given to the calculated loss figures from these cavity measurements. Additionally, it was necessary to measure the absolute power transmission of the gratings in order to give feedback to Dr. Morten Ibsen so that a new set of gratings could be written.

5.1.2 Grating transmission measurements

Initial attempts to measure the gratings' transmission, using an optical spectrum analyser (OSA) and various white light sources, were hampered by inefficient coupling into the fibre due to the small core of the fibre and the relative intensity of the light at 780 nm. Since the grating strengths were relatively high this led to unresolved transmission measurements due to restricted analyser sensitivity. Unfortunately it was not possible to source an LED at the correct wavelength in order to try using this as a light source. By detuning the laser away from the grating bandgap, it was possible to use the ASE of the laser diode to make measurements of the gratings using an optical spectrum analyser (OSA). Here the mode structure of the external cavity laser was evident although an approximate subtraction method was used to account for this. However, it was soon evident that the grating was not fully resolved. The difference between the peak transmission with the laser tuned to the centre of the bandgap, and the transmission with the laser tuned outside of the bandgap, was much larger than the extinction exhibited by the ASE measurement.

5.1.3 OSA scan grating measurement

Since the available OSA had a maximum resolution of 0.01 nm, this allowed a direct sampling method at discrete wavelengths using an attenuated laser. With this method it was possible to resolve the grating bandgap by taking measurements at fixed intervals across the bandgap. In order to automate this process a LabView computer program was written. A DC power supply (HP E3631A) was used to change the wavelength via the laser grating piezo. A diagram of the experimental set-up is shown in Fig. 5.1. The initial wavelength output from the laser was manually adjusted to a value estimated from the unresolved transmission "dip" of an OSA scan. After each wavelength (voltage) step, the OSA was scanned over a period of 0.6 nm to 1 nm, a peak detection was initiated, and the maximum transmission was recorded by computer. The width of the OSA scan was chosen so as to contain the peak transmission over all of the scanning wavelengths. The voltage range of the laser piezo was -20 V to 120 V and, since there was a 10 times gain for the externally input voltage, care was taken to ensure that the applied voltage did not exceed this range when taking into consideration the internal voltage set on the piezo driver itself. A separate "voltage bleed" routine was included in the LabView program to gradually return the applied voltage to zero at the end of

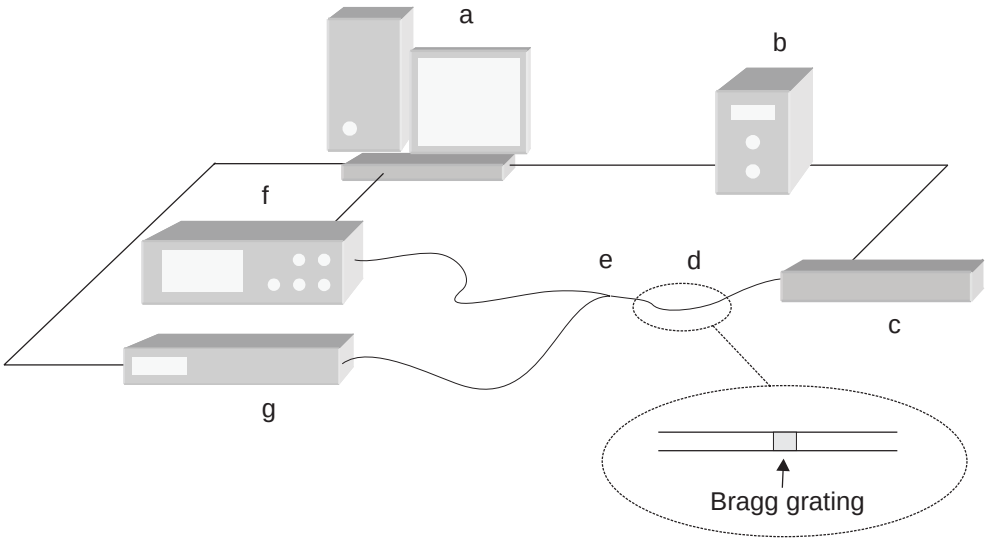

FIGURE 5.1: Schematic of grating transmission measurement set-up: (a) PC; (b) DC power supply; (c) ECDL, free space optics and fibre launch; (d) Bragg grating position; (e) 50-50 coupler (port 4 terminated in index matched fluid, not shown); (f) optical spectrum analyser; (g) wavemeter.

the scan in order to protect the laser cavity piezo and grating mount.

The power output and wavelength from the other port of the 50/50 coupler was measured using a wavemeter and this was also recorded. The voltage was then increased in linear steps across the bandgap. There was a difference of 0.12 nm between the OSA wavelength and the wavemeter wavelength. Since the wavemeter was self-calibrating these wavelengths were the ones chosen. The power reading from the wavemeter was used for normalisation purposes. Initial measurements were restricted to a 6 V external input and hence it was necessary to manually tune the laser grating in the middle of the characterisation and overlap the data. This iteration method was actually increased to three partial runs in order to capture the bandgap in a single unbroken stretch. Figure 5.2 shows examples of this, where the traces from the central partial sweeps are indicated in red. By changing to the 25 V output from the DC power supply this was avoided. Since the temperature of the lab was not stable over long periods of time there was a compromise to be made on the size of the voltage step and the desired resolution.

Each sequence of events: voltage step, OSA sweep, peak search, OSA reading, and wavemeter reading, took approximately 4 seconds, so the size of the wavelength step was chosen accordingly. For instance, a 0.04 V input corresponded to approximately 2 pm, so a scan over 0.6 nm at this resolution took about 20 minutes. A full wavelength scan of about 0.6 nm was used for each grating in order

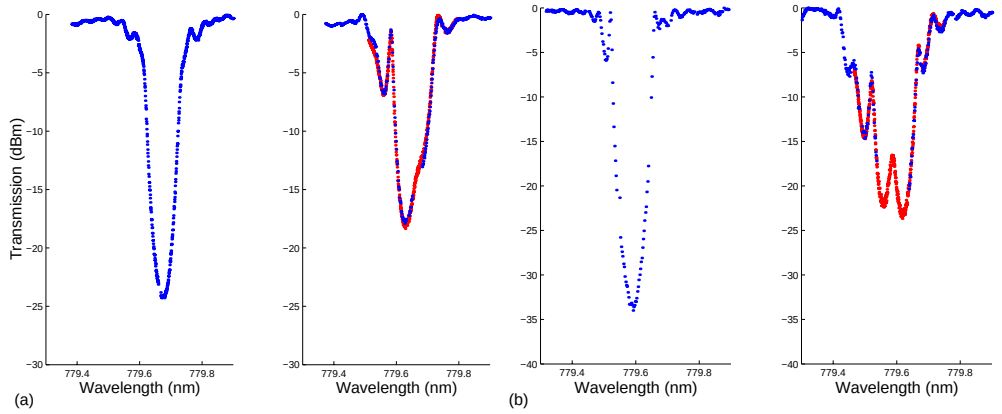

FIGURE 5.2: Grating transmission spectra in SM750 fibre for gratings written at: (a) 200 µm s^{-1}, and (b) 100 µm s^{-1}, normalised to 1 mW. Red traces indicate the central partial sweeps when spectra were recorded using a restricted laser piezo voltage.

to completely contain the bandgap and side lobes. After using a least squares fit of the grating transmission, $|t|^2$ (Eq: 3.27), with Matlab, a further agreement with the measurement could be gained from the size of the bandgap via Eq: 3.37. This Matlab fit is not sensitive to the grating loss per unit length, α, so this was set to zero for the analysis. Before commencing the characterisation, the wavelength range was checked to minimize mode-hops in the laser and, if necessary, the laser current or temperature was changed slightly to try to avoid the largest of these.

The gratings exhibited maximum extinctions of -34 dB and -24 dB, respectively, for the two different writing speeds but it was evident that the gratings were not uniform, showing deviations in grating strength, wavelength, and quality. This explains the lack of correlation between the initial finesse measurements and the transmission measurements. Figure: 5.2 shows examples of four gratings written at the two writing speeds, (a) 200 µm s^{-1}, and (b) 100 µm s^{-1}. The first trace of each shows relatively clean spectra, but the other two exhibit possible phase shifts in the gratings. Two further sets of gratings were written in the SM750 fibre, but problems with the writing laser and/or the fibre itself were evident in the grating transmission spectra. The spectra have been normalised to 1 mW for comparison.

5.2 Gratings in PS750

It was decided that using a more photosensitive fibre would allow for the use of a lower power output from the writing laser in order to produce repeatable gratings

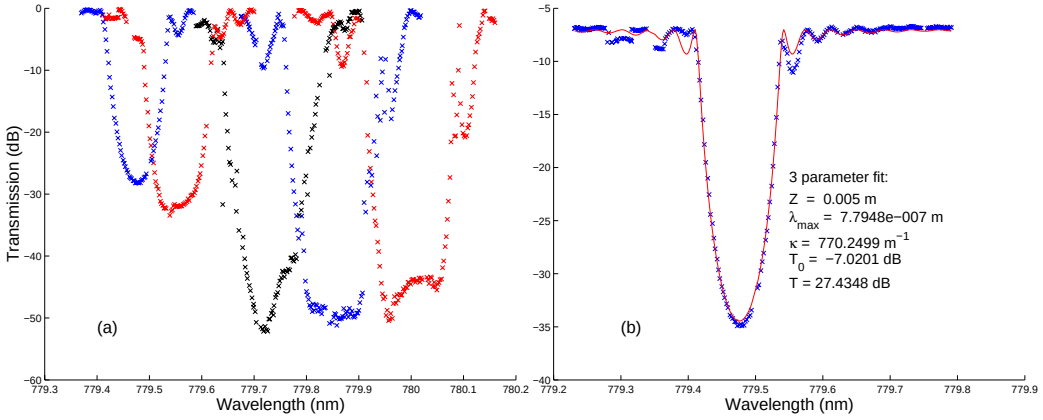

FIGURE 5.3: First gratings in PS750 fibre. (a) spectra for gratings written with fluences of 240, 320, 600, 1.2×10^3, and 2.4×10^3 J cm^{-2}, respectively (noise limited). (b) 3 parameter ($\lambda_{\max}$, κ, T_0) Matlab fit to grating written with fluence of 240 J cm^{-2}.

at our required wavelength. Figure: 5.3 illustrates the grating spectra from initial test gratings written in hydrogenated Fibercore PS750, a boron/germanium co-doped fibre. Fig: 5.3(a) shows the spectra for gratings written with fluences of, from left to right, 240, 320, 600, 1.2×10^3, and 2.4×10^3 J cm^{-2}. The photosensitive fibre allowed for a reduction by almost 2/3 of the power used previously for the SM750 fibre, with the fluence being governed by the writing speed. Figure: 5.3(b) shows the computed fit for the first grating written with a fluence of 240 J cm^{-2}, which shows a grating strength of 27 dB. For the gratings written at the slowest speeds, fits were made with the bottom section of the data omitted (below about -40 dB on the graph) to remove the points in the noise. The third grating, written at 600 J cm^{-2} showed a grating strength of 50±1 dB, with the fit showing good agreement at the band edges. Whilst the first three gratings show an apparent linear relationship between the wavelength of maximum reflectivity and the writing fluence, the last two gratings, written at the slowest speeds (largest fluence) show signs of saturation. The wavelength dependence on index change is given by

$$\lambda_{\max} = \lambda_B \left(1 + \eta \delta n_1 / n_1\right) \tag{5.1}$$

[100], where $\eta \approx 1$, so initially there is an almost linear relationship between writing fluence and index change (Erdogan et al. actually report a power law dependence in the growth of the UV index change with time [111]).

5.3 Test cavities

Using the data from the previous test set, four sets of six gratings were written[1], with each grating separated by approximately 5 cm. Each set was written with different writing parameters. The fluences for the four sets were 150, 185, 400 and 800 J cm^{-2}, with respective grating lengths of 5, 5, 4 and 2 mm. The wavelength of the writing laser was 244 nm in all cases. The grating length was chosen for a number of reasons. Firstly, very short gratings would require a high writing power and the writing laser stability would then be problematic, and secondly, it was still believed that loss could be a problem, so long gratings would exhibit more loss. To remove the hydrogen and thermally stabilize the gratings they were initially annealed at 100 ^{o}C for 19 hours. The gratings were separated into cavity pairs, and fibre was pigtailed to the cavities.

5.3.1 Closed cavity measurements

Although the fit used for the single grating measurements is not sensitive to the grating loss per unit length, α, the transmission measurement of a cavity is much more sensitive to losses due to cavity enhancement. By measuring the cavity finesse and throughput, the data could then be used to gather information about both the grating transmission and grating loss, as outlined in Chapter: 3, Eqs. 3.12 and 3.17. The measurement of cavity finesse was initially carried out by measuring the FWHM of the cavity resonances and the FSR by stopping the oscilloscope during a frequency or cavity length scan. The measurements were then made manually by using the "magnify" function of the oscilloscope. If the resonances did not look clean, the oscilloscope was run again, a measurement was recorded, and so forth, until a reasonable estimate of the finesse could be obtained. This method was not particularly accurate, and open to possible inadvertent subjectivity.

By saving the oscilloscope trace to a personal computer, a pair of Lorentzian curves could be fitted to the trace and a more accurate measurement could be made, however there was still the question of the magnitude of the experimental error and possible bias in the choice of when to make the actual measurement. To this end a LabView program was written to try to eradicate these issues. The experimental set-up used to characterize the cavities is shown in Fig: 5.4 and a diagram of the relevant features, from a cavity transmission experiment, is shown

[1]Gratings written by Dr Morten Ibsen

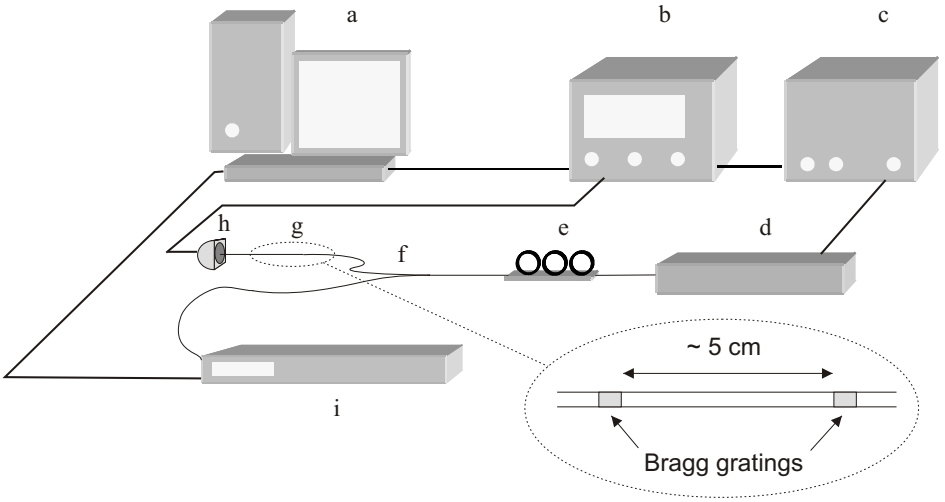

FIGURE 5.4: Schematic of fibre cavity characterization set-up: (a) PC; (b) oscilloscope; (c) function generator; (d) ECDL, free space optics and fibre launch; (e) polarization control; (f) 50-50 coupler (port 4 terminated in index matched fluid, not shown); (g) fibre cavity position; (h) photodiode; (i) wavemeter.

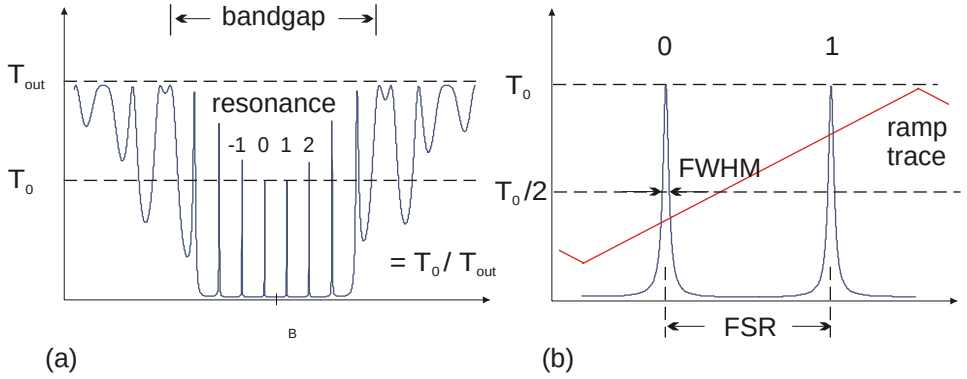

FIGURE 5.5: (a) Schematic illustration of the transmission spectrum of a fibre cavity with relevant throughput measurements, (b) pair of resonances used for finesse and throughput measurements (the finesse and peak transmission values for resonance 0 would be taken from the average of measurements made on the resonant pairs -1 and 0, and 0 and 1, for example). The ramp trace indicates the extent over which the wavelength is scanned.

in Fig: 5.5. Note here that the number of resonances drawn has been greatly reduced for clarity.

The measurements were taken using a Sacher tunable external cavity (Littman-Metcalf configuration) diode laser, the intensity of the light transmitted through the cavity was measured by a photodiode and the signal was displayed on a digital

oscilloscope. Initially the bandgaps of the cavities were identified by using the amplified spontaneous emission from the laser, in conjunction with an optical spectrum analyzer. Next, the wavelength of the ECDL was coarsely tuned to the grating bandgap by manual adjustment of the ECDL grating, and then it was adjusted to the centre using the DC voltage on the laser piezo driver. Finally the wavelength was scanned by applying a ramp voltage, or triangular wave, across the laser piezo via a function generator. This ramp voltage was adjusted so that the ramp covered two free spectral ranges of the cavity, see Fig: 5.5(b).

The cavity characterisation consisted of measuring several pairs of peaks within the centre of the cavity bandgap, covering a range of several FSR each side of the apparent maximum finesse position, in order to be sure of measuring the maximum finesse value and to get an indication of the uniformity of the gratings. The pairs were overlapped so that each resonance, discounting the first and last, was measured twice. Each oscilloscope trace, containing two resonances, was read into a personal computer and Lorentzian functions were fitted using a non-linear Levenberg-Marquardt (least-square) fitting function within LabView. From this fit, the finesse was calculated using the FWHM of each resonance and the FSR, and the amplitude for each peak was then calculated using the area under the Lorentzian peaks and the base level.

A secondary control set of these parameters was also measured from the raw data. The maximum value of the data around each resonance was recorded and the base level was subtracted for the amplitude, and the resonance width was calculated using rising and falling edge detection from a LabView trigger function, with the level set at half of the maximum data amplitude. The values from the fit were compared to these raw data values and where the FWHM values, or the amplitude values, of the data resonances differed from the fit by a set percentage, typically 5 %, the measurements were rejected. The program was written to register and save a set number of values (typically ten) for the finesse and amplitude of the peaks for each pair of resonances, in order to take an average and generate an error figure. The option to save the raw data was also included to allow for a double check. Additionally the power input to the wavemeter (via a 50/50 coupler) was recorded in order to normalize the throughput values upon analysis. The numerical fit, raw data, and finesse values were calculated in real time (subject to processor restrictions) and displayed on the computer for monitoring purposes.

In order to measure the resonant transmission, or throughput, τ, the transmission of the grating outside of the bandgap had to be measured. Again an average over

several measurements was taken. The laser was manually tuned to just outside of the bandgap and the transmitted intensity was recorded at both longer and shorter wavelengths. These measurements were taken at points where the oscilloscope traces had just "flattened out", outside of the first couple of oscillatory lobes of the grating transmission envelope. Wavemeter power readings were again used for normalisation.

The analysis part of the program calculated the finesse and amplitude values from each peak by taking the mean from each individual set of saved measurements and then taking a further average from the overlap of the next pair of peaks. In this way the finesse measurements for each peak were calculated from the average values of the FSR each side of each resonance. The mean amplitudes of each resonance were calculated in a similar way after normalisation. Effectively each resonance was measured at each side of the centre of the laser frequency sweep to account for any asymmetry in the sweep and, furthermore, a scan range of two FSR placed the measurements on the flattest part of an assumed laser piezo hysteresis curve.

The throughput, τ, was calculated from the ratio of the resonant transmission to the transmitted power outside of the bandgap. The normalised mean value for the throughput outside of the bandgap accounted for the slope in the gain curve of the laser. Although, in general, the measurements were made on a rising voltage ramp there was no discernible difference noted in the final results when the negative ramp was used, however care had to be taken to ensure that the overlapped measurements were averaged correctly. Using Equations: 3.12 and 3.17, the grating loss and transmission was computed and graphically displayed, in addition to the finesse and throughput values, so that a picture of the cavity resonant structure could be obtained. The errors in the finesse and the throughput measurements were taken to be the standard deviations from their respective mean values, with the relative uncertainties of the loss and transmission calculated by

$$\frac{\Delta L}{L} = \left\{ \frac{\Delta\tau^2}{4\tau(1-\sqrt{\tau}\,)^2} + \frac{\Delta F^2}{(F+\pi/2)^2} \right\}^{1/2} \tag{5.2}$$

and

$$\frac{\Delta T}{T} = \left\{ \frac{\Delta\tau^2}{4\tau^2} + \frac{\Delta F^2}{(F+\pi/2)^2} \right\}^{1/2}, \tag{5.3}$$

which have been derived from Equations: 3.12 and 3.17.

			Measured		Calculated	
No.	Z (mm)	WF (J cm^{-2})	F	τ (%)	L ($\times 10^{-3}$)	T (dB)
1a	2	800	73.5 ± 1.4	60 ± 2	9.3 ± 0.6	-14.9 ± 0.1
1b *	2	800	65.5 ± 1.3	64 ± 3	9.6 ± 0.9	-14.3 ± 0.1
1c	2	800	73.6 ± 1.4	60 ± 2	9.4 ± 0.6	-14.9 ± 0.1
2a	5	150	36.7 ± 0.4	58 ± 2	19.8 ± 1.1	-12.0 ± 0.1
2b	5	150	48.0 ± 0.6	49 ± 3	19.2 ± 1.4	-13.5 ± 0.2
3a	4	400	149.9 ± 10.0	6.5 ± 0.6	15.5 ± 1.1	-22.8 ± 0.4
3b	4	400	156.6 ± 10.0	2.6 ± 0.3	16.7 ± 1.1	-25.0 ± 0.4
3c	4	400	155.8 ± 10.5	3.4 ± 0.3	16.3 ± 1.1	-24.4 ± 0.4
4a	5	185	37.7 ± 0.3	56 ± 1	19.9 ± 0.5	-12.2 ± 0.1
4b	5	185	62.2 ± 0.7	33 ± 1	21.3 ± 0.7	-15.5 ± 0.1
4c	5	185	51.3 ± 0.4	42 ± 1	21.1 ± 0.4	-14.2 ± 0.1
* grating mismatch						

TABLE 5.1: Measurements and calculations from the first set of test cavities written in PS750 fibre. Grating length, Z; writing Fluence, WF; maximum cavity finesse, F; cavity throughput on resonance, τ; calculated grating loss, L; and calculated grating transmission, T.

5.4 Cavity analysis, results, and discussion

Table 5.1 summarizes the maximum finesse measurements, F, for the test cavities, in addition to the corresponding cavity throughputs, τ. The single-grating transmission, T, and loss, L, were calculated by using the measured values for the finesse, F, and throughput, τ, and inverting Eqs. (3.17) and (3.12). The cavities have been labelled 1 to 4 for the 2 mm grating cavities, written with a 800 J cm^{-2} fluence, 5 mm grating with 150 J cm^{-2} fluence, 4 mm with 400 J cm^{-2} fluence , and 5 mm 185 J cm^{-2} fluence gratings, respectively. The letters a to c represent cavities with similar writing parameters. Using Eqs. 3.30 and 3.31 the grating coupling strengths, κ, and loss coefficients, α, can be calculated. The results are shown in Table 5.2. As an example of the experimental results from a full cavity characterisation, Figure: 5.6 shows the measured cavity finesse, throughput and resulting loss values for cavities 3a and 4a over a range of cavity resonances close to the centre of the grating bandgaps. For wavelength-matched gratings, the highest cavity finesse occurs when $\delta \approx 0$, i.e., for the cavity resonance closest to the wavelength of maximum reflectance of the gratings. Any asymmetry in the cavity transmission peaks in this wavelength range points to a mismatch of the two cavity gratings. It is evident that the losses are nearly flat over the centre of the grating band gap and are approximately 1.6 % and 2.0 %, respectively, for the two cavities.

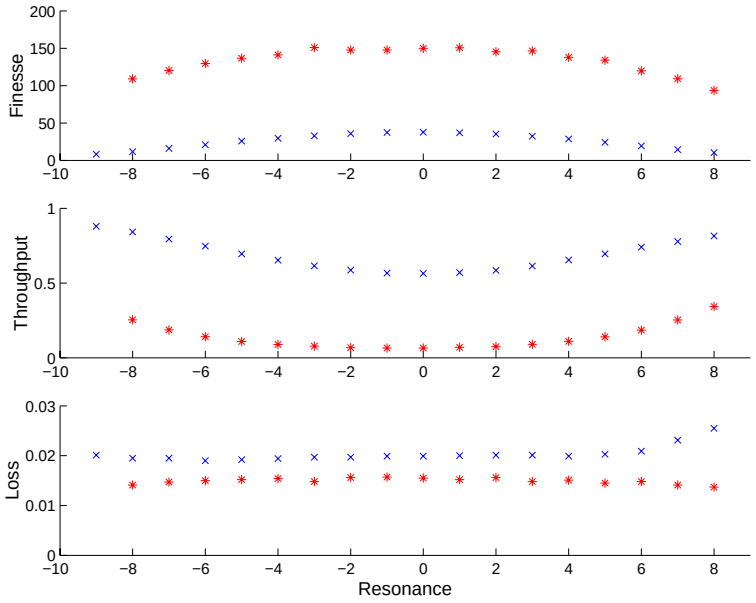

FIGURE 5.6: Measured cavity finesse, F, throughput, τ, and calculated loss, L, for cavities 3a (red stars) and 4a (blue crosses).

5.4.1 Test method agreement

To measure the transmission of a single grating from a closed cavity it is necessary to stretch the other cavity grating in order to shift its Bragg wavelength away from that of the grating under investigation. The fibre each side of one of the gratings was protected using two small diameter tubes of rubber and clamped, then the grating was manually stretched using a single axis stage. The transmission measurements were made using the method described in Subsection: 5.1.3. The coupling strength, κ, was calculated using a least squares fit of $|t|^2$ to the measured spectra, where t is given by Eq: 3.27. Since the loss coefficient, α, is too small to have a visible effect on a single path measurement, this was set to zero.

The values of κ for the first cavity in each set are shown in Table 5.2. When compared to the values from the cavity characterisation measurements, it can be seen that there is good agreement. This gives confidence in the grating loss values calculated from the cavity measurements. Fig: 5.7 shows examples of the transmission spectra of individual gratings from cavities 3a and 4a, together with fits to the data. It can be seen that the fits accurately model the bandgap and the minimum transmission, as well as some of the sidelobes of the spectra. The values for the coupling coefficient arising from the fit are: $\kappa = 840$ m^{-1} and $\kappa = 424$ m^{-1} for cavity gratings 3a and 4a, respectively.

In order to find out the effect that the stretched grating has on the numerical fit to

	Cavity measurement		Single-grating measurement
Cavity no.	κ (m $^{-1}$)	α (m^{-1})	κ (m^{-1})
1a	1198 ± 6	5.7 ± 0.4	1200 ± 23
1b	1163 ± 6	5.7 ± 0.5	
1c	1198 ± 5	5.7 ± 0.4	
2a	410 ± 3	4.2 ± 0.3	407 ± 5
2b	445 ± 5	4.4 ± 0.4	
3a	826 ± 12	6.4 ± 0.6	840 ± 6
3b	891 ± 12	7.4 ± 0.6	
3c	873 ± 12	7.1 ± 0.6	
4a	415 ± 3	4.3 ± 0.2	424 ± 14
4b	492 ± 2	5.3 ± 0.2	
4c	461 ± 3	5.0 ± 0.1	

TABLE 5.2: Coupling and loss coefficients for first cavity set in PS750, measured by two methods. Single grating measurements are an average of each pair.

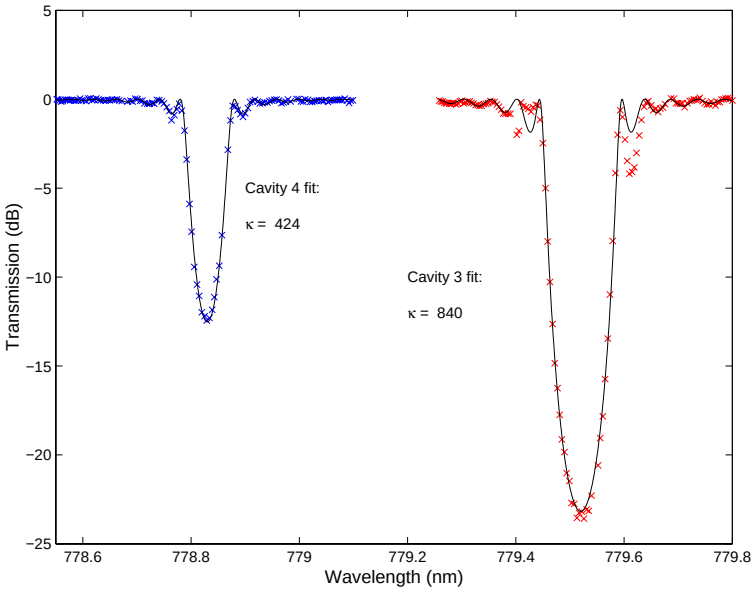

FIGURE 5.7: Transmission spectra of a single grating from cavity 3a and cavity 4a. Continuous lines are theoretical fits.

the transmission measurement of the other grating, an experiment was conducted using Cavity 1a. Since this set of cavities has the largest bandgap (see Eq: 3.37) it was expected that interference effects would be greatest with this set. One grating was stretched such that the wavelengths of maximum reflection for the cavity gratings were separated in wavelength by 0.4 nm, 0.7 nm, and 1.2 nm, and transmission measurements were made on each, the results of which are shown in Table: 5.3. It appears that the fitting routine is fairly robust, with very little apparent change in the values for κ for the unstrained grating. On the other

	$\Delta\lambda$ (nm)	$\lambda(nm)$	$\kappa(m^{-1})$	T (dB)
Unstrained grating	0	779.67	1195	-14.8
Stretched grating	0.39	780.06	1172	-14.4
Unstrained grating	0	779.68	1201	-14.9
Stretched grating	0.72	780.40	1178	-14.5
Unstrained grating	0	779.68	1197	-14.9
Stretched grating	1.23	780.91	1187	-14.7

TABLE 5.3: Effect of grating wavelength separation on OSA transmission measurements of Cavity 1a

hand there is a small change in κ evident in the strained grating, however this is only about 1 %. The experiment also indicates the extent of grating tuneability, although it seems prudent not to stretch gratings any more than necessary.

5.4.2 FSR measurement

The FSR of the first cavity from each set was measured by taking the average over eleven free spectral ranges in a window around the position of highest finesse. The values were calculated by measuring the wavelength of the twelfth resonance with a wavemeter and subtracting the wavelength of the first resonance. A comparison was made between the average FSR measured in this way and the calculated FSR using Eq: 3.36, including the penetration depth calculated using Eq: 3.35. When the gratings were written, their positions were indicated with a marker pen which covered an area larger than the extent of the grating. Therefore the measured cavity length (between gratings) was taken to be within the possible extremes of these marks, measured with a ruler, whilst taking into account the grating lengths. Table 5.4 gives the results of these measurements. Although the measured and calculated values correspond for cavities 1a and 3a, there is a discrepancy in the values for cavity 2a. Since the wavelengths in the centre of the ranges were also measured using the wavemeter and give good agreement with the figures for FSR_{meas}, there is more confidence in these values. This indicates an error in the physical measurement of the cavity. It has to be noted that the physical extent of the gratings preclude the possibility that the penetration depth alone could be the reason. Furthermore, allowing the grating length, Z, to be a variable parameter in the Matlab fits to the transmission spectra give values for the gratings of 2.007 mm, 4.994 mm, 4.056 mm and 5.027 mm, respectively, for cavities, 1a, 2a, 3a, and 4a, so the nominal lengths of the gratings are not suspect. The absolute error in the grating lengths cannot be given due to the confidence

Cavity	λ_{max} (nm)	FSR_{meas} (pm)	L_e (mm)	L_{cav} (mm)	FSR_{calc} (pm)
1a	779.7	3.7±0.1	0.4	57±2	3.6±0.1
2a	779.2	3.4±0.1	1.2	43±5	4.6±0.5
3a	779.5	4.9±0.1	0.6	42±3	4.8±0.3
4a	778.8	4.2±0.1	1.2	-	-

TABLE 5.4: Free spectral range measurements from each set of initial cavities in PS750 fibre. λ_{max}, wavelength of maximum reflectivity; FSR_{meas}, average FSR from wavemeter measurements; L_e, penetration depth of grating at λ_{max}; L_{cav}, length of cavity between gratings; FSR_{calc}, calculated FSR.

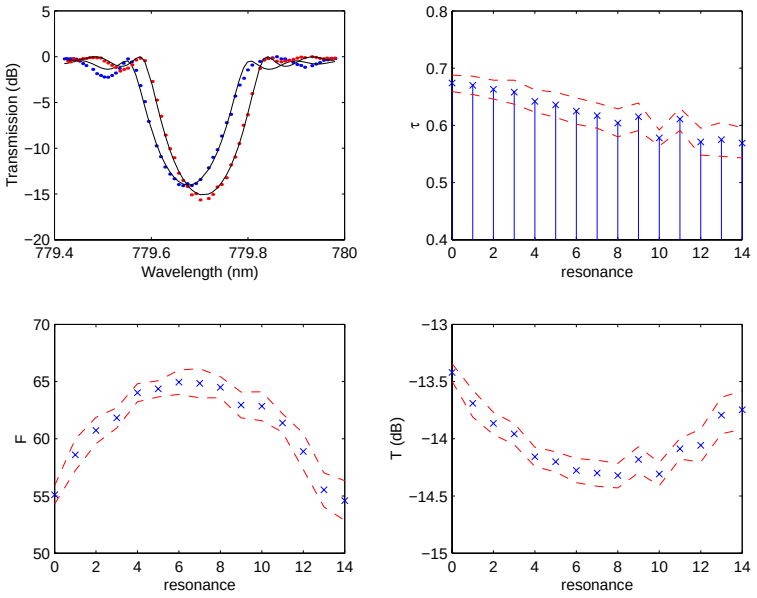

FIGURE 5.8: Grating transmission measurements for Cavity 1b and LabView data for measurements around region of maximum finesse: cavity throughput, τ, finesse, F, and calculated grating transmission, T. Red dashed lines indicate the limits of one standard deviation.

taken in allowing four free parameters in the fit. No measurement of the physical length of cavity 4a was recorded.

5.4.3 Asymmetric cavities

Comparing the results of the two gratings forming a cavity also allows us to identify any grating mismatch in strength and Bragg wavelength. Note that these effects are usually coupled: increasing the index modulation, δn_1, increases the strength of the grating (κ is increased), but also increases the Bragg wavelength, as this is dependent on the average effective refractive index (Eq: 5.1). Figure: 5.8 shows the measurements from a cavity characterisation experiment performed on Cavity 1b. The throughput data indicates a grating mismatch since the minimum throughput

does not coincide with the maximum finesse. With matched gratings, these values are coincident.

Although the fits to the transmission spectra are good at the band edges, there is evidence of interference between the stretched and unstrained gratings. The reason for this is that the wavelengths were separated by only 0.5 nm when the measurements were made (as against 0.6 - 1.0 nm usually). The spectra were recorded with as little time separation as possible to eliminate temperature drift and wavelength drift of the laser, so minimum strain was placed on the cavity at this time. The cavity broke during a repeat of the experiment and the measurement of the second stretched grating. Furthermore, only 64 wavelength steps were used for each scan. Nevertheless, a numerical simulation using the values of κ for the two gratings (1123 m^{-1} and 1213 m^{-1}) reproduced the resonant behaviour extremely well.

For gratings at the same wavelength, but different strengths, the throughput is symmetrical about the maximum finesse, like in the matched case. In this case the maximum reflectivity for each grating occurs at the same wavelength, with the reflectivity decreasing in a symmetrical manner for either positive or negative wavelength detuning. The highest finesse occurs at the centre of the bandgap of both gratings. Since the number of cavity round trips is proportional to the finesse, the cumulative loss is greatest at this point. Furthermore, towards the cavity band edges the transmission of both gratings increases symmetrically, and therefore the throughput increases (see Eq. 3.12). On the other hand, for mismatched gratings of different strengths, the wavelength of highest finesse occurs between the wavelengths of maximum reflectivity of each grating and there is an asymmetry in the throughput between positive or negative detuning due to the combination of different grating transmissions and grating losses.

One of the gratings from the second set of test cavities (2c, not included in Tables: 5.1 and 5.2) was cleaved and fibre was spliced to the remainder of the grating, forming a cavity formed from gratings with similar coupling coefficients, κ, but different lengths. Figure: 5.9 shows that the throughput is near a minimum around the region of maximum finesse. The transmission spectrum of the shorter grating also illustrates how the bandwidth is larger for shorter gratings of the same coupling strength (Eq: 3.37). Fits to the transmission spectrum of a uniform grating show a difference in λ_{max} of 10 pm between the two which is within the measurement limits imposed by temperature fluctuations, OSA resolution, or the accuracy of the fit to the shorter grating. Here a four parameter (κ, Z, λ_{max}, T_0) model

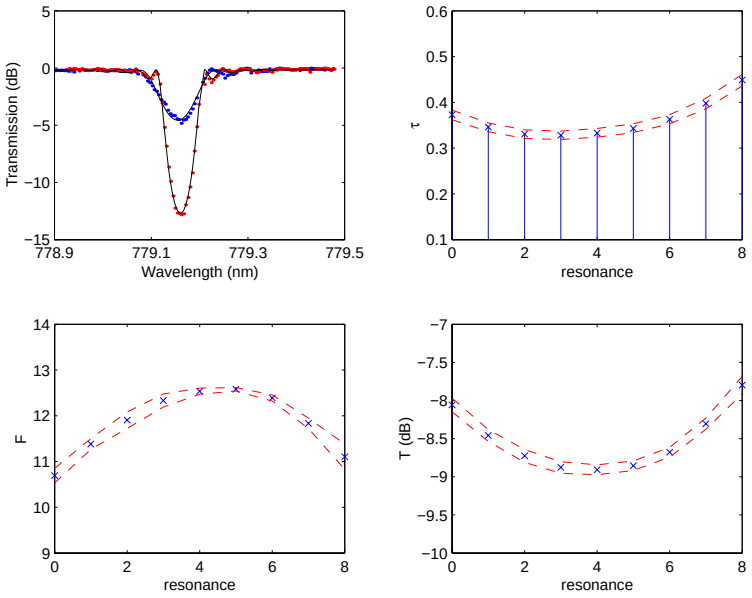

FIGURE 5.9: Grating transmission measurements for Cavity 2c and LabView data for measurements around region of maximum finesse: cavity throughput, τ, finesse, F, and calculated grating transmission, T. Red dashed lines indicate the limits of one SD.

was used for the shorter cleaved grating, which resulted in a grating length of 2.8 mm and a value for κ of 396 m^{-1}. The κ value for the uncleaved grating was 425 m^{-1}, in line with the other gratings from the set 2 cavities. In the case of the smaller grating it is possible that fusion splicing may alter the grating slightly from uniform.

If a scheme using reflectors of different reflectivity is to be implemented using Bragg gratings, to increase the number of photons arriving at the detector, say [92], then consideration of this issue will be necessary.

5.5 Grating loss

The grating loss is of the order of 1-2 % for all the test cavities, with the grating loss coefficients, α, calculated to be in the range of 4 to 7 m^{-1}. Since α is almost constant for all the gratings then the highest losses occur for the gratings with the lowest values of κ, and vice versa, which can be seen by comparing Tables 5.1 and 5.2. The reason for this is that, for weaker gratings, the light penetrates further into the grating, and therefore the loss per reflection is higher, whilst for high values of κ the penetration is small. The loss per reflection is equal to the product of twice the penetration depth and the intensity loss per unit length, so,

on resonance, using Eq: 3.35 we have

$$L|_{\lambda=\lambda_{\max}} \approx \frac{2\alpha}{\kappa} \ . \tag{5.4}$$

So, although there is a correlation between the writing fluence and the coupling coefficient, κ, (See Tables 5.1 and 5.2) as expected, there is no direct relation with the loss per unit length α. For comparison it is worth noting that a measurement on a closed "proof of principle" cavity at 1550 nm (see Subsection: 4.4), with gratings written into standard telecommunication fibre, resulted in a grating transmission of T = -19.2 dB and a single pass loss of $L = 0.0027$. These figures relate to a coupling coefficient, $\kappa = 580$ m^{-1}, and loss per unit length of $\alpha = 0.8$ m^{-1}.

5.5.1 Discussion of losses

It is interesting to consider the origin of these losses in UV written gratings[112]. The losses cannot be assumed to arise solely from scattering. Scattering losses for boron/germanium codoped fibre in strong gratings ($R > 0.97$) at 1535 nm wavelength have been measured by Janos et al.[113] to be $(5 - 30) \times 10^{-5}$ dB cm^{-1}. The usual wavelength scaling of Rayleigh scattering is $1/\lambda^4$, which equates to α = 0.02-0.1 m^{-1} at 780 nm and is therefore about two orders of magnitude too small to account for the observed losses. Absorption losses, on the other hand, are known to increase strongly for shorter wavelengths in germano-silicate fibres because of absorption bands in the UV at about 240 nm. Losses comparable to $\alpha = 4$ m^{-1} measured here have been reported previously[114, 115].

Anoikin et al.[115] have also reported thermal annealing to reduce grating losses at temperatures larger than 200 ^{o}C. These losses have been attributed to the creation of paramagnetic Ge(1) centres in the fibre. In contrast to these previous studies where gratings were fabricated using pulsed excimer lasers, the gratings considered here are written by a cw UV source. Because of the much lower peak powers in this case, one might have expected to induce fewer colour centres in the germano-silicate matrix, however this appears not to be the case. Furthermore, the results show that the absorption rate is hardly affected by increasing the writing fluence from 150 to 800 J cm^{-2}. This suggests that the majority of colour centres are created at very low UV intensities, and that this photo-darkening effect quickly saturates at higher UV exposures.

5.6 Conclusion

The use of a cavity measurement method offers a more sensitive vehicle for measuring the losses in cavity reflectors when compared to single pass measurements. However, the spectra from single gratings can offer not only correlation with cavity calculations of the calculated grating transmission via the measured insertion loss, but also through the measurement of the grating bandwidth. In this way, the agreement between the two methods gives more confidence in the grating transmission figures.

Due to the magnitude of the photosensitivity of standard germanium doped single mode fibre it was not possible to consistently and reliably write gratings of the required strength, due to either the high power stability of the writing laser, or the index change mechanism within the core of the fibre. The switch to a boron/germanium doped fibre allowed consistent grating writing with a lower laser power, however the grating loss per unit length, α, was found to be almost five to ten times that calculated for the "proof of principle" gratings written at 1550 nm in standard telecom fibre. Experimental results also suggested that α did not scale with writing fluence. Similar losses have been reported in the literature and one such paper showed that it was possible to reduce the losses via thermal annealing.

Chapter 6

Annealing Experiments

There are two main contributing loss factors which affect the capability of a cavity detection device: the grating loss, as discussed at the end of the last chapter, and the gap loss, a loss mechanism which is intrinsic to a planar fibre gap cavity due to diffraction. In order to judge how the grating loss will affect atom detection, a figure of merit, ϵ, is defined which relates the projected cavity SNR with a theoretical ideal cavity. Following this, the chapter continues with the description of thermal annealing experiments, prompted by results published in the literature. These annealing experiments are shown to reduce grating losses, with the resultant figure of merit, ϵ, becoming comparable with that calculated for the 1550 nm gratings.

6.1 Grating loss and atom detection

A measure of how the grating loss will affect the final device can be acquired by comparing the signal to noise ratio, SNR, of a measurement made with the cavity in question with the signal to noise ratio, $\mathrm{SNR}_{\mathrm{ideal}}$, of a measurement made using an "ideal" cavity - one for which there is no grating loss and for which $T = L_{\mathrm{gap}}$, maximizing $\mathrm{SNR}_{\mathrm{ideal}}$. Using the theory developed in the paper by Horak et al.[92] we consider a homodyne detection scheme and low atomic saturation for which we obtain a ratio

$$\epsilon(T, L) = \frac{\mathrm{SNR}}{\mathrm{SNR}_{\mathrm{ideal}}} = 4\frac{TL_{\mathrm{gap}}}{(T + L_{\mathrm{gap}} + L)^2} \ . \tag{6.1}$$

To a good approximation, a small number of atoms can be considered to influence the light field in the cavity independently (i.e. ignoring photon transfer between

atoms) so the inverse, $1/\epsilon$, gives the number of atoms needed in order to obtain the same signal to noise ratio as that obtained for the measurement of a single atom in the ideal case.

6.2 Annealing experiments

The thermal decay of fibre Bragg gratings has been reported upon extensively [111, 116–118], and the use of temperature accelerated ageing for grating stabilisation is now commonplace. By pre-annealing the gratings at a higher temperature than the operating temperature, grating devices can be made to operate for decades, with very little loss in the UV induced index change taking place. Erdogan et al.[111] showed that a "power law" could describe the decay of the "normalised integrated coupling constant (NICC)" with time, for germanium/erbium doped fibre, with the decay fitting the form

$$\mathrm{NICC} = \frac{1}{1 + \mathrm{A}(\mathrm{t}/\mathrm{t}_1)^{\vartheta}} \ . \tag{6.2}$$

Here A and ϑ are temperature dependent parameters and the NICC is the integrated coupling constant, ICC, normalised to its initial value at $t = 0$, with $t_1 \equiv 1$ min. For lossless gratings

$$\mathrm{ICC} = \tanh^{-1}(\sqrt{\mathrm{R}_{\max}}) = \kappa \mathrm{Z} \ , \tag{6.3}$$

from Eq: 3.26, where $R_{\max}$, κ, and Z, hold their previous definitions. Equation: 6.2 shows that, for small ϑ, the rate of decay decreases very rapidly. This means that, after an initial rapid decay in the index change at a certain temperature, the reduction of κ with time becomes negligible on the scale of years ($\kappa \propto \delta n_1$), hence the use of thermal pre-annealing. Baker et al.[118] found that the same power law applied to boron and germanium co-doped fibre, although with different parameters A and ϑ as expected, however they also found that hydrogenated B/Ge doped fibre did not follow the Erdogan power law model, and instead proposed a logarithmic time base model for this type of fibre.

The reduction of losses in fibre Bragg gratings near to 780 nm wavelength has been reported previously: Around 800 nm Askins and Putnam[114] showed that the losses could be reduced by photobleaching, with only a minor reduction in grating reflectivity, whilst Anoikin et al.[115] reported on the use of thermal annealing to reduce grating losses by using temperatures above 200 °C. As discussed

in the previous chapter, the throughput of a fibre cavity is dependent on both the transmission of the mirrors (gratings) and any intrinsic losses in the gratings themselves. By thermally annealing strong gratings, the grating strength can be reduced in order to produce better impedance matching, which will increase the cavity throughput and the signal to noise ratio of an atom detection measurement made with a final device. Without changing the fibre geometry the gap loss cannot be changed if the gap size is kept constant, however any reductions in the grating loss will improve the detector efficiency, i.e. increase ϵ. With this in mind, experiments were carried out to find the required combination of temperature and time needed to reduce the strength of the gratings by a specified amount.

6.2.1 Single grating

A grating from the first test set of gratings in PS750 (see Sec: 5.2) fibre was chosen (Grating 3 written at 600 J cm^{-2}) and, for this first experiment, it was placed on a hot plate at 300 °C for a set amount of time, then removed, and the transmission spectra measured using the method described in Subsection: 5.1.3. The fibre grating was then returned to the hot plate for another prescribed time period and the procedure was repeated. Once it was noted that the effect due to the annealing was diminishing the temperature was raised to 400 °C and the process repeated. The final annealing temperature used was 490 °C. To ensure contact with the hotplate the fibre was secured beneath a ceramic plate whilst annealing but, since a stable transmission measurement was not possible by simply lifting the grating off the hotplate, the removed grating was stuck onto card and placed onto the optical table for each measurement. It must be noted that the gratings were pre-annealed for 19 hours at 100 °C as an initial stabilisation process during manufacture, and that this is the "starting point" used in any following discussion.

The Matlab transmission fits for the first two measurements were obtained by removing the lowest points as discussed in Sec. 5.2. Figure 6.1 shows the transmission results for the annealing experiment, normalised to 1 mW, carried out with grating 3. There was no discernible change when annealing at 150 °C for 5 minutes or at 200 °C for 15 minutes. The error figures here are taken from the difference between the actual data point minima and the fit minima. It should be noted that the error for the first measurement is large due to the noise level. From seven different measurements of this grating, taken at different times, the minimum transmission for the fit was T = -50 ±1 dB with the resulting coupling coefficient κ = 1287±16 m^{-1}. The dashed lines are a clamped cubic spline, used

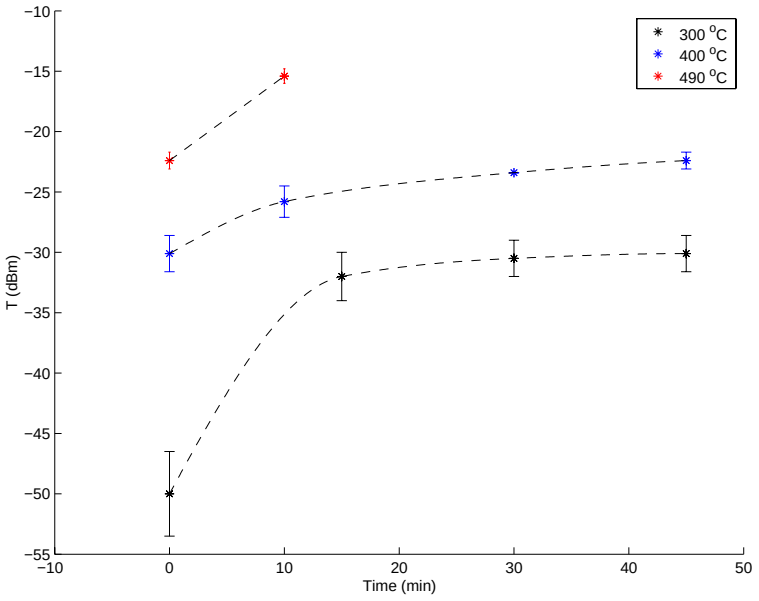

FIGURE 6.1: Measured minimum transmission,T, for grating 3 annealing experiment. Dashed line is guide for eye only.

for a guide to the eye only.

For a set temperature and time, a grating's ICC will decay to a percentage of its initial value, regardless of whether the annealing starts from this initial value or if the ICC has been reduced by previous annealing at a lower temperature. So, when annealing at several different temperatures, it is necessary to consider the decay history prior to the change in temperature. Erdogan et al. commented that this is quite different from a single-activation-energy decay process and is consistent with the idea that all electrons up to a given trap depth are wiped out by a decay process.

The initial pre-anneal at 100 °C for 19 hours was expected to remove all of the hydrogen from the fibre so it was interesting to see if the Erdogan power law could be used to model the time and temperature needed for annealing to a specific grating strength. Fig. 6.2 illustrates the attempted fit using this model. The initial pre-annealing was assumed to have reduced the ICC by less than 10 %, so the initial NICC bounds here have been chosen to be 0.9 and 1. The circles represent an initial median value of NICC=0.95 at the start of the 300 °C anneal with the error bars displaying the bounds. The red curve denotes a fit of Eq: 6.2 to the 300 °C data and the blue curve to the 400 °C data. The calculated values for A and ϑ are also displayed on the plot. By comparing these two curves it can be seen that the 300 °C annealing process can be considered as a period of decelerated aging: 45 minutes at 300 °C being equivalent to approximately 2

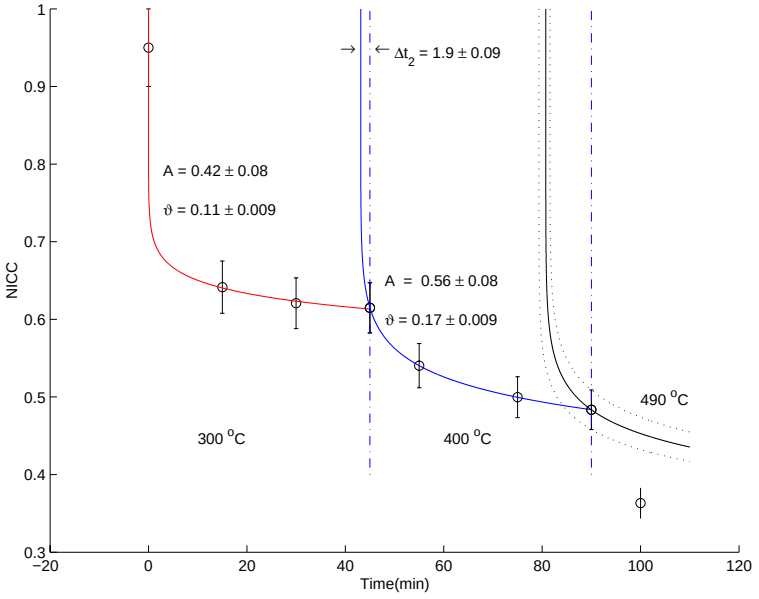

FIGURE 6.2: Power law investigation for annealed grating 3. Red trace: power law fit to 300 °C annealing data; blue trace: power law fit to 400 °C annealing data. Error bars denote upper and lower bounds for an NICC value between 90 % and 100 % after manufacture pre-anneal at 100 °C. Black trace is extrapolation for 490 °C annealing (bounds dotted).

minutes at 400 °C, shown here by the value Δt_2.

The Erdogan model (Eq: 6.2) considers a linear relationship between ln(A) and the temperature, T, measured in kelvin: $A = A_0 \exp(aT)$ where a is a constant coefficient, and also linearity in the relationship between ϑ and temperature, $\vartheta = T/T_0$. Using these relationships, and the calculated values for A and ϑ, the curve for the 490 °C annealing could be computed. This curve and the bounds are displayed on the plot. As can be clearly seen, the predicted decay is much less than that measured, so it appears that this model is not particularly useful in predicting the short term annealing behaviour of these gratings.

Another interesting result of this experiment concerns the wavelength of maximum reflectivity. The final value was found to be the same as the initial value. Initially the wavelength shortened due to a reduction in the magnitude of the refractive index modulation, but after 45 minutes at 300 °C the wavelength returned to its initial value. This seems to be in agreement with Chisholm et al.[116], who reported on this behaviour and attributed it to the positive index change in the core due to the annealing of the boron. However the maximum change in wavelength measured here was only of the order of 40 pm, a figure which could be attributed to the resolution of the OSA or temperature change in the lab. So, although the trend cannot be verified, the final resultant wavelength does give agreement to

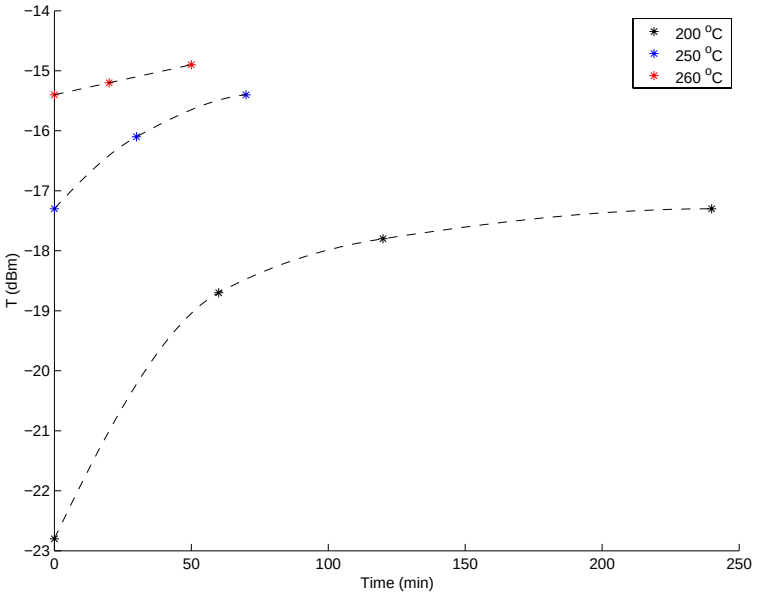

FIGURE 6.3: Calculated minimum transmission,T, for cavity 3a annealing experiment. Dashed line is guide for eye only.

this argument. The reverse process (grating inscription), shown in figure Fig. 5.3, gives an idea of the magnitude of wavelength shift which was expected.

6.2.2 Cavity annealing

The next experiment was carried out to anneal a cavity in a controlled manner in order to reach a specified grating transmission. Cavity 3a was chosen with a target grating transmission of -14.9 dB, the same as measured for Cavity 1a. Since the gratings used in each cavity were 4 mm and 2 mm long, respectively, this was designed to give an indication of loss per grating length. A similar method to the single grating experiment was used but the grating transmission was calculated from the finesse and throughput measurements made on the cavity. The temperatures were kept lower in order that the fibre did not become weakened and also so that the grating strength did not drop too quickly and pass the target strength.

Although no change had been noted at 200 °C in the previous experiment, for a short time period, this was the first temperature used here with a one hour initial time period. After one hour, the grating transmission was increased from -22.8 dB to -18.7 dB and after another three hours to -17.3 dB. At this point, the annealing became slow and the temperature was increased to 250 °C to accelerate the process. The transmission of the grating was thus increased to -16.1 dB and finally to -14.9 dB at temperatures of 260 °C.

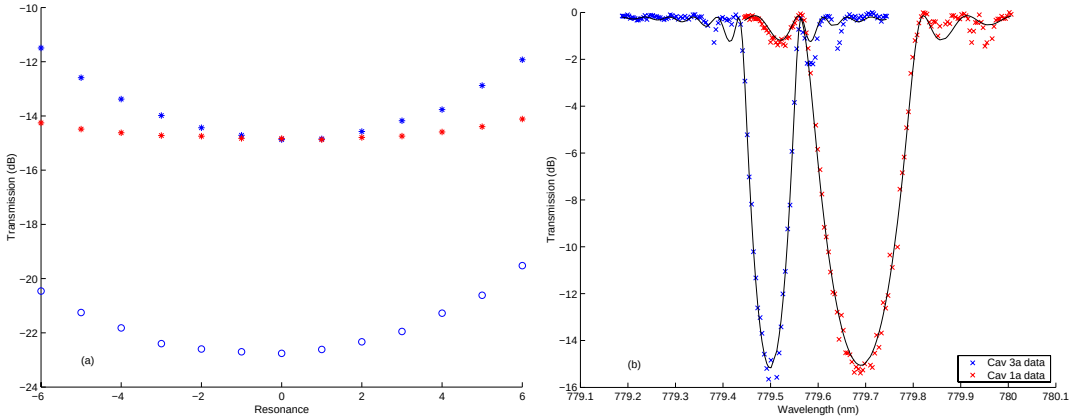

FIGURE 6.4: Transmission comparison of annealed cavity 3a and cavity 1a. (a), Calculated grating transmission: 1a red stars, 3a blue stars, original transmission, circles. (b) Single grating transmission measurements.

At the end of the experiment a transmission measurement of a single grating from the cavity was also carried out using the OSA scan method after stretching one of the gratings. The transmission data calculated from the finesse and throughput measurements of cavity 3a is illustrated in Figure: 6.3, whilst comparison with cavity 1a is shown in Fig. 6.4. The minimum grating transmission, calculated from finesse and throughput measurements, and the measured values are in good agreement. Also, by comparing Fig. 6.4 (b) with Fig. 5.7, it can be seen that very little shift in wavelength has occurred for cavity 3a after annealing.

6.2.3 Discussion of annealing results

As expected, the maximum cavity finesse was reduced due to the increased grating transmission, from $F \approx 150$ to $F \approx 80$ over the extent of the experiment. However, more importantly, a reduction of grating loss from 1.6 % per pass to 0.5 % was observed, as seen in Fig. 6.5, which can also be compared with the 0.9 % loss per pass for cavity 1a. Using Eqs. 3.30 and 3.31 we find that the loss per unit length was reduced from $\alpha = 6.4$ m^{-1} to $\alpha = 1.6$ m^{-1} after the full annealing. Note that the magnitude of the final value is now much closer to the value calculated for the 1550 nm cavity ($\alpha = 0.8$ m^{-1} with $\kappa = 580$ m^{-1}). At the same time, annealing only reduced the coupling strength of the grating from $\kappa = 826$ m^{-1} to 599 m^{-1}, i.e. by about 27 %.

For the targeted application of fibre cavities for single-atom detection on an atom chip, this significant improvement in grating performance means that losses are now smaller than the intrinsic diffraction loss in the cavity gap (~ 1 %) required to

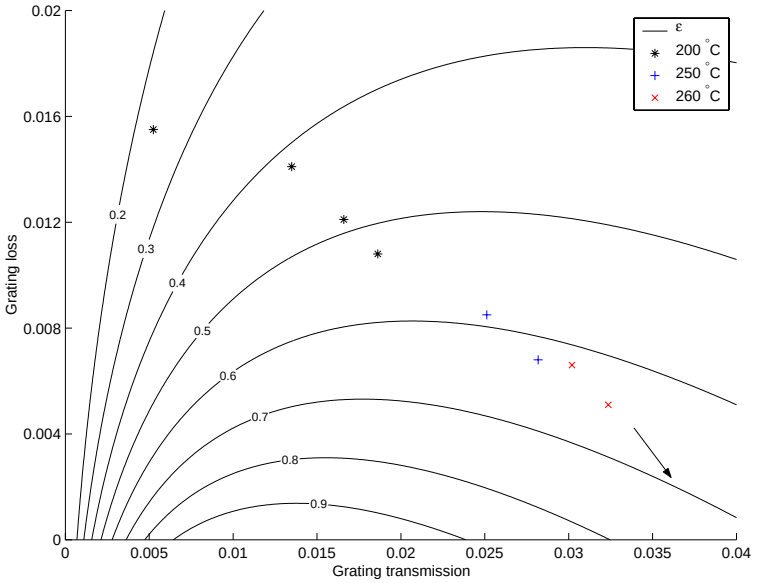

FIGURE 6.5: Results of thermal annealing of cavity 3a. Grating loss, L, and transmission, T (data points), calculated from cavity finesse and throughput measurements, against cavity figure of merit, ϵ (contours). Arrow indicates annealing trend.

accommodate the atom. Therefore the device sensitivity will no longer be limited by the quality of the Bragg gratings. Fig. 6.5, constructed using Eq. 6.1, shows the trend in ϵ as the experiment progressed, with ϵ increasing from 0.24 to 0.64. Here a single pass loss of 1.2 % is included for the 5 µm gap. Section: 8.1 details this calculation and contains details of the fibre parameters which affect this loss.

6.2.4 Reduction of annealing temperature

Since the pre-annealing during manufacture was carried out at 100 °C, a further experiment was carried out at even lower temperatures. A similar cavity was chosen, cavity 3c and, since it was apparent that much longer anneal times would be necessary, the oven used for the manufacturing pre-annealing was employed. Temperatures of 125 °C, 175 °C, and 225 °C, were used with respective time periods of 20 hours, 4 hours, and 4 hours. Transmission measurements were carried out using the previous method.

Figure: 6.6 shows the results of this experiment. Fig. 6.6(a) compares the lower temperature annealing (top) of cavity 3c with the faster higher temperature annealing of cavity 3a. Although the strength of 3c has not been reduced quite as much as for the higher temperature annealing, it can be seen that the trends are the same, and the reduction would be the same over a longer time period. This is

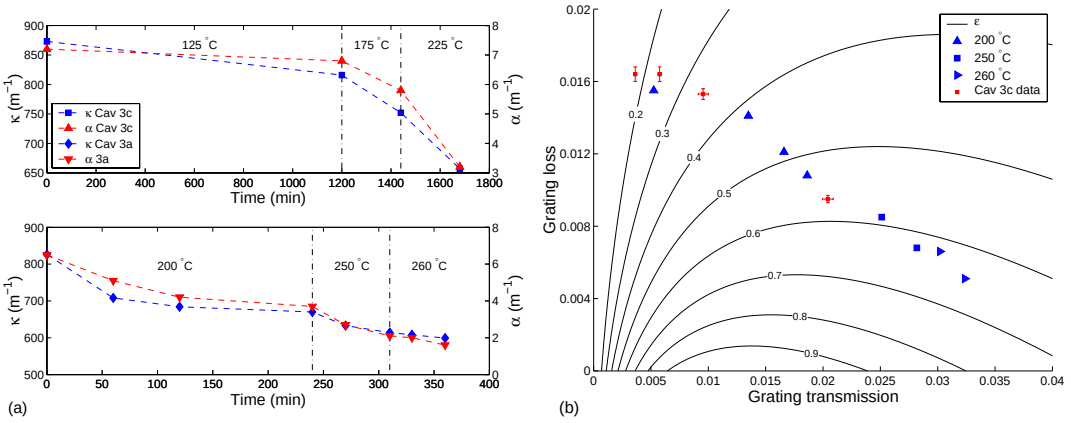

FIGURE 6.6: Comparison of low and high temperature annealing, (a): The trends in grating loss per unit length and coupling constant against time are compared for low temperature annealing of cavity 3c, top, and high temperature annealing of cavity 3a, bottom. (b) plots the grating loss against transmission for the same two cavities with reference to the cavity figure of merit ϵ.

more evident in Fig. 6.6(b) where the calculated grating transmission and loss are plotted for the two cavities, against the figure of merit, ϵ. The red points in the plot represent the cavity 3c annealing with the error bars derived from the spread of results over several measurements.

For inclusion in a final device on an atom chip, an important point arises from these experiments concerning the vacuum bake-out procedure. Temperature ramps from 100 °C to 200 °C over 24 hours are common for this procedure, which implies either that the pre-anneal manufacture temperature needs to be higher, which has consequences for the initial writing process, or that there is further reason for an annealing step to tune the gratings. However, if the bake-out temperature is kept below 125 °C there appears to be a minimal reduction in the grating strength for gratings which have undergone a similar pre-anneal.

After being raised to higher temperatures the fibre appears to be more brittle, although this has not been quantitatively proved - care has to be taken when working with uncoated fibre as it intrinsically brittle anyway. However another observation is that the coating on the fibre becomes discoloured and "crispy" at temperatures around 200 °C. This is not so evident when using a hotplate as only the stripped fibre is in contact with the plate, however in an oven a substantially larger length is heated.

It has been reported that coated fibre does not necessarily cause a large out-gassing problem under high vacuum, but it is possible that chemical changes due to the heating may change this. Of course the affected fibre can be chemically stripped

using dichloromethane or something similar, but then there is a much larger length of uncoated fibre to work with. Since a final device needs to be mounted onto a chip with the input and output fibres fed through vacuum feedthroughs it would appear that a minimum of stripped fibre would aid handling, and also that a reduction in the amount of cleaving and splicing near to the cavity would be advisable.

6.3 Conclusion

Heating of the gratings to 200-260 °C for times of the order of one hour proved to be an efficient method to reduce the intrinsic losses in the gratings, with a similar result for longer time periods at lower temperatures. At the same time, this thermal processing only weakly affected the structural changes of the glass matrix responsible for the refractive index grating[119], as evidenced by the relatively modest reduction in grating strength. This is in agreement with Askins and Putnam[114] who showed that these losses can be reduced by photobleaching with a corresponding minor reduction in grating reflectivity, similar to the results reported here for thermal annealing.

Chapter 7

Cavity Characterisation II and New Cavities

The first part of this chapter describes new experimental set-ups, and changes made to the equipment used, when experimental work recommenced after the fire. Measurements from a new set of cavities written in replacement fibre are given, and the grating characteristics are compared with the previous cavities and annealing experiment results. During initial measurements on the new cavities, the possibility of previous detector bandwidth limitations arose. Since it was not possible to check any of the previous results or equipment, a set of experiments was devised to investigate the extent of any systematic error and a correctional model was developed.

7.1 New equipment set-up

After the fire, certain changes were made to the equipment set-up. A Littrow configured ECDL (Toptica) replaced the Sacher Littman-Metcalf configured laser. This did not tune as smoothly as the previous laser and mode-hopping prevented the measurement of single grating transmission spectra using the OSA scan method. Since previous experiments showed good correlation between the cavity measurements and single grating measurements this was not thought to be too much of a problem, although verification of cavity grating transmissions would have been beneficial.

There are various possible causes/solutions for the laser stability but these were

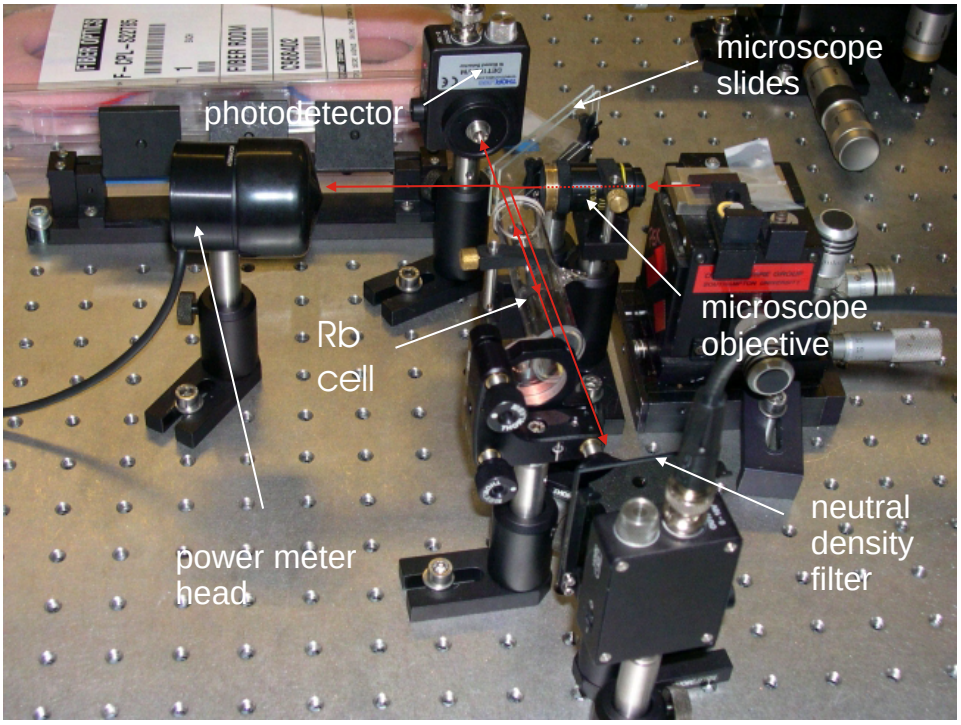

FIGURE 7.1: Rubidium spectroscopy set-up for frequency reference. Red lines show primary beam path.

not fully investigated. The diode was not AR coated which results in more mode competition between the external cavity and the diode itself. The laser also had a "fibre dock", an integral mount for coupling light directly into fibre, and an internal 35 dB optical isolator. This is far less than the two 45 dB isolators which were used previously.

The main benefit of a Littrow configured external cavity over a Littman-Metcalf is that the output power is much larger (for a similarly rated diode) since the zero order mode reflection from the external grating is used in experiments rather than the first order mode. However since this set-up precluded the use of pre-fibre external optics, such as neutral density filters, the excess power was simply discarded by misaligning the fibre dock. The laser includes a beam steering mirror so scanning over small frequency ranges, such as when measuring cavity finesse, did not cause a large problem for fibre launching. For the cavity characterisation, any asymmetry in the launch power is corrected for via the normalisation procedure.

A Newport power meter replaced the wavemeter for normalisation power measurements and an absolute frequency/wavelength reference was obtained from the replacement OSA (50 pm resolution) or via rubidium spectroscopy. Fig. 7.1 shows the absorption and saturated rubidium spectroscopy set-up. Light from the second

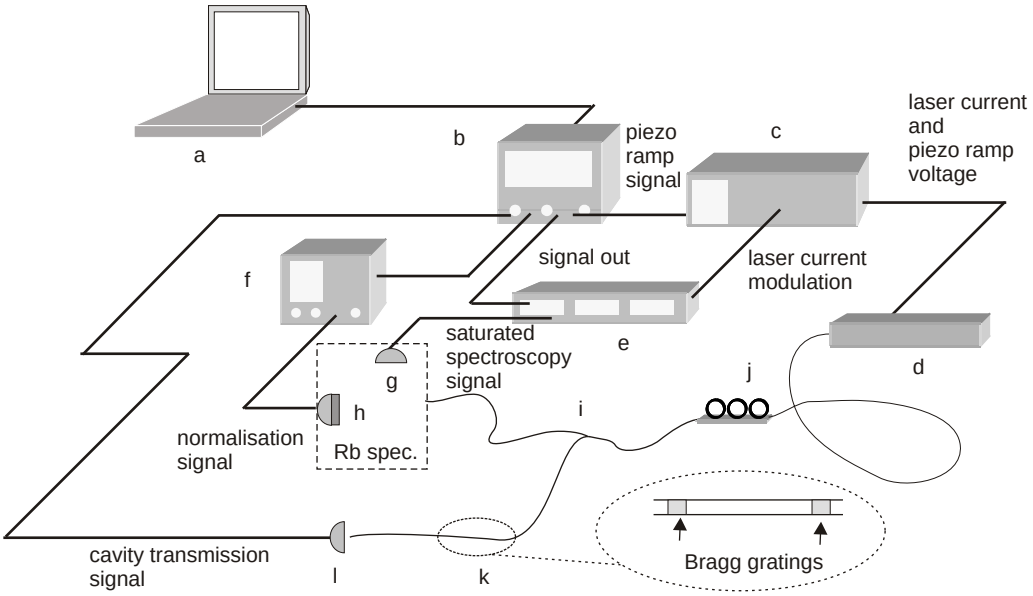

FIGURE 7.2: Experimental set-up for cavity characterisation and Rb spectroscopy: (a) computer; (b) oscilloscope; (c) laser control; (d) external cavity diode laser; (e) lock-in amplifier; (f) power meter; (g) photodiode; (h) power meter head; (i) 50-50 coupler (port 4 not shown); (j) polarisation control; (k) cavity; (l) amplified detector. Dashed box indicates Rb spectroscopy set-up shown in Fig. 7.1 (absorption signal not shown).

output fibre of the 50-50 coupler was collimated with a microscope objective and directed towards the head of the power meter. Light was split off this beam using two microscope slides, mounted in a double filter holder, as an improvisation for an optical flat, with the foremost slide acting as the front reflection and the rear slide acting as the back reflection. The microscope slides are thin enough that the front and back reflections from each slide are not widely separated in space and could effectively be used as single beams. In the figure only the primary beams and reflections are indicated. The beam from the front slide passes through a rubidium cell onto a photodetector giving an absorption spectrum, with a neutral density filter preventing saturation of the detector, whilst the second beam from the other slide is reflected back along the same path through the cell to another photodetector to provide a saturated signal.

Figure 7.2 shows a schematic of the experimental set-up used for cavity characterisation and rubidium spectroscopy. The laptop computer was connected via a network hub to the oscilloscope, communicating via TCIP. This freed up the USB ports, allowing one to be used to communicate with a stepper motor controller during mounting experiments (see Chapter 8), and the other could be used

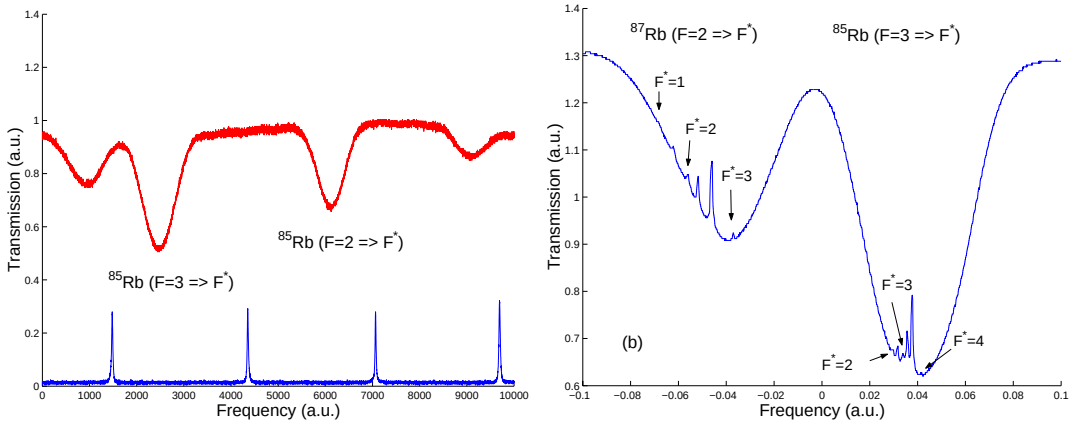

FIGURE 7.3: (a) Cavity 3N1 and rubidium D2 absorption spectrum. (b) Part of the hyperfine structure of ^{87}Rb and ^{85}Rb $5S_{1/2}$ to $5P_{3/2}$ D2 transition.

to control a DC power supply (not shown) for feedback control (see Subsection 7.1.1), via a USB to GPIB converter, or alternatively communicate with a piezo controller connected to the mounting stage piezo actuators.

A frequency reference could be obtained from either the absorption or saturated absorption rubidium spectroscopy signals, however, in order to resolve the hyperfine structure of the Rb D2 line a lock-in amplifier (Stanford Research Systems SR830) could be used. To measure wavelengths away from 780.24 nm (D2 line), the output from the fibre cavity was directed into an OSA. Figure: 7.3(a) shows resonances from one of a new set of cavities (3N1) and the fine structure of the rubidium D2 line (absorption spectrum). Here slight tension is applied to the cavity. Fig. 7.3(b) shows the signal from the saturated beam with the hyperfine transitions indicated.

7.1.1 Feedback control

When characterising cavities, much more drift was noted in the resonances than had been seen previously. This was either down to the lab temperature control and/or laser stability. To get a good comparison between pairs of cavity resonances, or between different cavities, it is necessary to make measurements in a similar manner each time. As mentioned in Subsection 5.3.1, finesse measurements were taken at a central position on the voltage ramp, and for comparison purposes every measurement must be taken around this area.

The new laser had a self contained scan module which supplied a configurable ramp voltage to the laser piezo, so a DC power supply was inserted in series with

this, between the module and the laser, allowing an element of computer control to the scanning. This is illustrated in Figure: 7.4. To avoid having to manually change the DC voltage on the laser cavity piezo, a rudimentary feedback system was written into the LabView program.

The error signal, δ, calculated from the difference between the position of the fit of the first resonance to the position S/4, as indicated in Fig. 7.4(ii), was used in a proportional, integral, derivative (PID), feedback control system. Initially the two resonances were aligned at the quarter (S/4) and three-quarter positions on the oscilloscope, as illustrated in Fig. 7.4(ii) (here S = 2FSR), the DC voltage was used to position the resonances laterally, and the peak to peak voltage of the ramp was used to adjust the width. A small base voltage was initially set on the DC power supply to allow for negative voltage shifts. The feedback system was initiated and the measurement procedure was started once the resonances had aligned to the required position.

During characterisation the feedback calculation and adjustment was carried out after each finesse measurement and did not affect the following measurement. Due to equipment reading and computer speed restrictions the sampling rate was extremely slow, so the feedback system relied mostly on the proportional correction, with only a slight derivative correction, and the integral constant was set to zero. The voltage constants were calculated from the peak to peak voltage needed to scan over two FSR and the feedback system was tuned only coarsely. However, the system was stable long enough to make the required measurements and characterise a cavity, but could not correct for sudden temperature changes, so a cut-off was included to avoid runaway feedback.

7.2 New cavities and detector bandwidth

Replacement PS750 fibre was obtained and a new set of cavities was written. A similar selection of grating lengths was chosen, (3 mm, 4 mm, and 5 mm), and several of the cavities (named 3N1, 3N2,.., 4N1, 4N2,..., 5N1, 5N2,..., respectively) were characterised in a similar manner to Subsection: 5.3.1. The initial observation was that the losses appeared to be slightly lower, with the cavities comprising of 5 mm gratings exhibiting a finesse of around 200 and a 10 % to 20 % throughput on resonance, indicating a single pass loss of around 1 % ($\alpha \sim 3$ m^{-1}). For these measurements a similar reversed biased detector (Thorlabs DET110) was used.

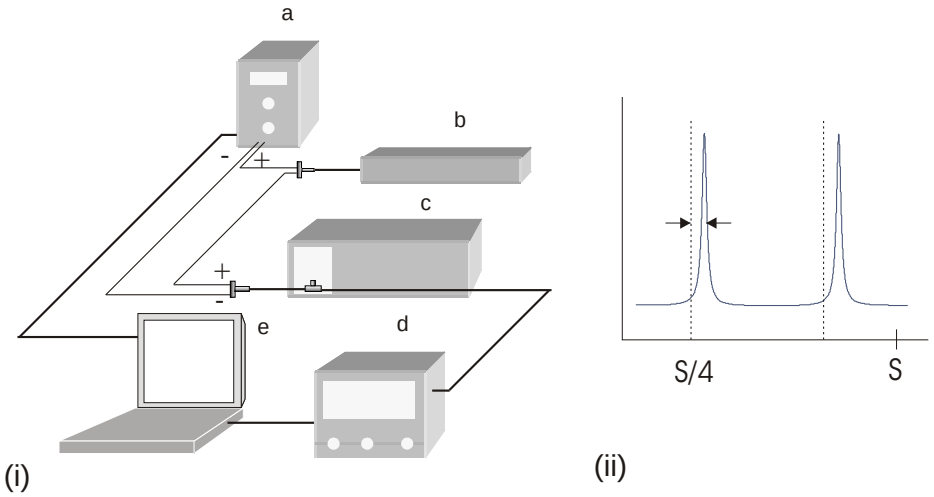

FIGURE 7.4: (i) feedback control equipment set-up: (a) DC power supply; (b) ECDL; (c) laser control box (scan control unit); (d) oscilloscope; (e) computer. (ii) positional error, δ.

Cavity	Z (mm)	F	τ	T (dB)	L
3N1	3	134	0.50	-17.8	0.007
4N1	4	64	0.81	-13.7	0.005
4N2	4	80	0.65	-15.1	0.008
4N3	4	105	0.67	-16.2	0.006
4N5	4	100	0.54	-16.5	0.008
5N1	5	226	0.27	-21.2	0.007
5N2	5	202	0.24	-21.1	0.008
5N5	5	250	0.14	-23.4	0.008

TABLE 7.1: Closed cavity measurements of new cavities (amplified detector).

Previously, measurements had been made with the detector connected to the 50 Ω input of the oscilloscope, using an additional 10 kΩ load, in order to increase the sensitivity. However, the detector was then connected directly to the 1 MΩ input of the oscilloscope for the cavity measurements, described in Chapter: 5, and the annealing experiments. To avoid saturation of the detector, when measuring the cavity throughput outside of the cavity bandgap, the input power was highly attenuated. Therefore a higher sensitivity was required in order to resolve, and fit to, the resulting low amplitude resonance peaks, when measuring relatively high finesse cavities. It was believed that the detector speed, although reduced, was fast enough to measure the resonance widths with the relatively slow scanning speed used (2.5 Hz). As mentioned previously in Sec. 5.1: reducing the scan range to the width of a resonance, and keeping the scan rate the same, had shown no discernible change in the height of the resonance peak on the oscilloscope.

The correlation between the single grating transmission measurements and the calculated grating transmission from cavity finesse and throughput measurements added weight to this. However, a slight discrepancy was noted in the throughput when making measurements on one of the 4 mm grating cavities (4N1) with a new faster photodiode (DET10A) at a faster scan rate. This prompted a set of experiments to investigate if, and by how much, detector response had limited previous measurements.

The response time of a photo-detector is influenced not only by the diode capacitance and resistive load, but also the capacitance and resistance of the circuit involved - coaxial cables and equipment (in this case an oscilloscope). Furthermore, although the response of a detector has to be faster when measuring a higher finesse cavity compared with a lower finesse cavity, the maximum photocurrent is lower due to the throughput, i.e. although the signal has to go up and down faster it does not have to go up as high. Here we consider cavities of similar length and the same optical input power. This means that the nominal rise time (or bandwidth) is not necessarily the limiting factor for relatively fast changing signals since a detector can follow a faster signal if the amplitude is smaller. It was possible to measure the finesse of one the lower finesse cavities (4N1) by going directly into 50 Ω after increasing the input power. The fit to a 2.5 Hz scan gave a similar result for the finesse (F=60 ±5) as a scan with lower input power into 1 MΩ so it appeared that the cavities with weaker gratings had not been greatly affected by equipment response. Here it has to be noted that the signal was noisy and also that the other 4 mm grating cavities had all shown finesses of F=80 to 90.

7.2.1 Simple detector response model

When characterising the cavities, the wavelength sweep is considered to be linear in time as the voltage across the laser piezo is linearly increased. Therefore there is a direct correspondence between the wavelength and time as recorded on an oscilloscope, and the finesse can be written as

$$F = \frac{\mathrm{FSR}}{\Gamma} = \frac{t_{\mathrm{FSR}}}{t_{\Gamma}} \tag{7.1}$$

where Γ is the width (FWHM) of the resonance, t_{FSR} is the time taken to sweep across one free spectral range of the cavity, and t_{Γ} is the time taken to sweep across the width of a resonance. The time signal, or cavity response, is approximately

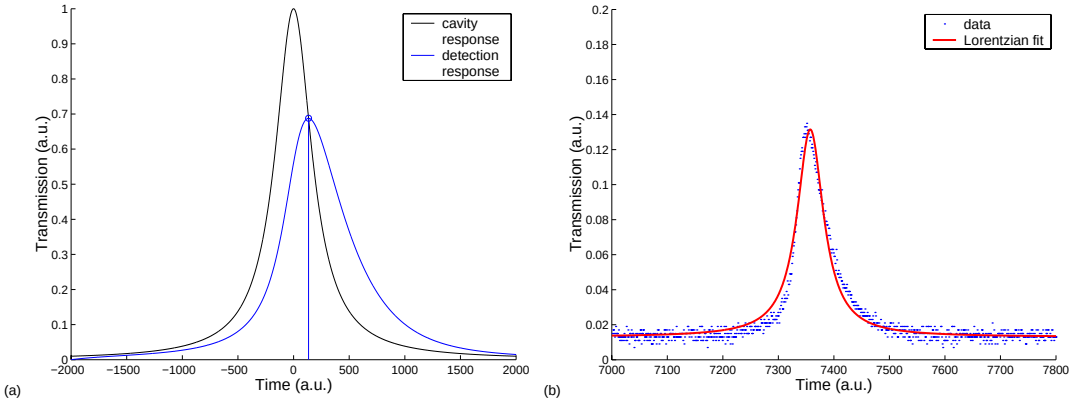

FIGURE 7.5: (a), Cavity response and detector response; (b), Lorentzian fit to 12.5 Hz scan of cavity 5N2

Lorentzian (see Subsection 3.1.3), taking the form

$$L_1(t) = \frac{A}{\pi} \frac{t_\Gamma/2}{t^2 + (t_\Gamma/2)^2} \ . \tag{7.2}$$

For simplicity, the peak of the resonance is taken to occur at t=0 as the time invariance of convolution allows for this.

If a finesse measurement is affected by the time response of the measurement system then the recorded resonance peaks will be broadened, delayed, and "skewed". The result consists of the signal convoluted with a detector system response function of the form

$$f_{det}(t) = \begin{cases} \frac{1}{\tau_c} e^{-\frac{t}{\tau_c}} & (t \geq 0) \\ 0 & (t < 0) \end{cases} \tag{7.3}$$

where τ_c is some time constant related to the detection system. Figure: 7.5(a) illustrates the effect of this theoretically, whilst Fig. 7.5(b) shows the resultant Lorentzian fit to the data resulting from a 12.5 Hz scan of one of the highest finesse cavities. This is a relatively extreme case as the normal scanning speed is 2.5 Hz.

The skewing results in an asymmetry of the resonant peaks however, since the measurements are made by fitting Lorentzian curves to the data and the measurement regime used produces only a slight asymmetry, a "broadening factor", $t_{\rm det}$, can be introduced to account for the detection system. Effectively we can consider a convolution of a Lorentzian resonance with a normalised Lorentzian with an effective width proportional to the time constant of the detection system. The

measured finesse is therefore

$$F_{\text{meas}} = \frac{\text{FSR}}{\Gamma_{\text{meas}}} = \frac{t_{\text{FSR}}}{t_\Gamma + t_{\text{det}}} \tag{7.4}$$

and the measured time signal

$$L_{1,\text{meas}}(t) = \frac{A}{\pi} \frac{(t_\Gamma + t_{\text{det}})/2}{(t - t_{\text{delay}})^2 + ((t_\Gamma + t_{\text{det}})/2)^2} \ . \tag{7.5}$$

since the convolution of two Lorentzians results in a Lorentzian with a linewidth equal to the sum of the original linewidths, i.e.

$$\Gamma_{\text{meas}} = \Gamma + \Gamma_{\text{det}} \tag{7.6}$$

or equivalently

$$t_{\Gamma,\text{meas}} = t_\Gamma + t_{\text{det}} \ . \tag{7.7}$$

The resulting time delay, t_{delay}, will be independent of the time it is measured so that finesse measurements are still consistent, i.e. each resonance will be time-shifted by the same amount and the free spectral range (FSR) will stay the same. A is the area beneath the curve which we assume remains constant provided that the convolution functions are normalised. Energy conservation dictates that this should be the case physically.

The amplitudes of the resonances can be related in a similar way provided that we keep the assumption that A remains constant. The amplitude, a_{res}, of the cavity resonance

$$a_{\text{res}} = \frac{2A}{\pi t_\Gamma} \ , \tag{7.8}$$

is measured as

$$a_{\text{res,meas}} = \frac{2A}{\pi(t_\Gamma + t_{\text{det}})} \ . \tag{7.9}$$

7.2.2 Experiment and the use of the simple Lorentzian model

The transmittance of the cavity is time invariant and, since short reasonably lossy cavities are used, effects due to the finite speed of light are neglected here. If the measurements from the cavity characterisation are equipment limited, then this can be used as an advantage. The time taken to scan across a free spectral range and the time taken to scan across the *measured* cavity linewidth are functions of

the scan frequency, however the effect of the rise time/fall time of the detection equipment is a constant within this frame of reference. In other words, as the scan frequency is varied, the ratio of the widths of $t_{\Gamma,\text{meas}}$ to t_{det} changes. Therefore the finesse measured is a function of the sweep frequency, ν_s, so we can rewrite Equation: 7.4 as

$$F_{\text{meas}}(\nu_s) = \frac{1}{1/F + t_{\text{det}}/t_{\text{FSR}}(\nu_s)} \ , \tag{7.10}$$

using Eq: 7.1. This relationship can be used to deduce the actual finesse from measurements made at different scanning frequencies.

The throughput outside of the bandgap does not change with scan rate so, using Equations: 7.8 and 7.9 and the assumption that the area beneath the curves is preserved, the throughput on resonance, τ, can be written as

$$\tau = \frac{t_\Gamma(\nu_s) + t_{\text{det}}}{t_\Gamma(\nu_s)} \tau_{\text{meas}}(\nu_s) \ . \tag{7.11}$$

Multiplying the top and bottom of the right hand side of Eq: 7.11 by F gives

$$\tau = \frac{t_{\text{FSR}}(\nu_s) + F\ t_{\text{det}}}{t_{\text{FSR}}(\nu_s)} \tau_{\text{meas}}(\nu_s) \ . \tag{7.12}$$

After calculating the values for t_{det} and F it is straightforward to calculate the corrected throughput values for each specific resonance. Corrected values for the grating transmission and loss can then be computed.

7.2.3 Experimental method

The finesse measurements and throughput measurements were obtained in the same way as described in Subsection 5.3.1 with the new set-up. The cavities were scanned at frequencies of 1 Hz, 2.5 Hz and 5 Hz using a LeCroy (Wavesurfer 44X) oscilloscope and both the DET110 and DET10A detectors. The same set of resonance peaks was scanned each time (to the best effort) and the average throughput outside of the bandgap was measured after running all of the scans. Each triplet of finesse measurements was used with Equation: 7.10 to compute values for F and t_{det}.

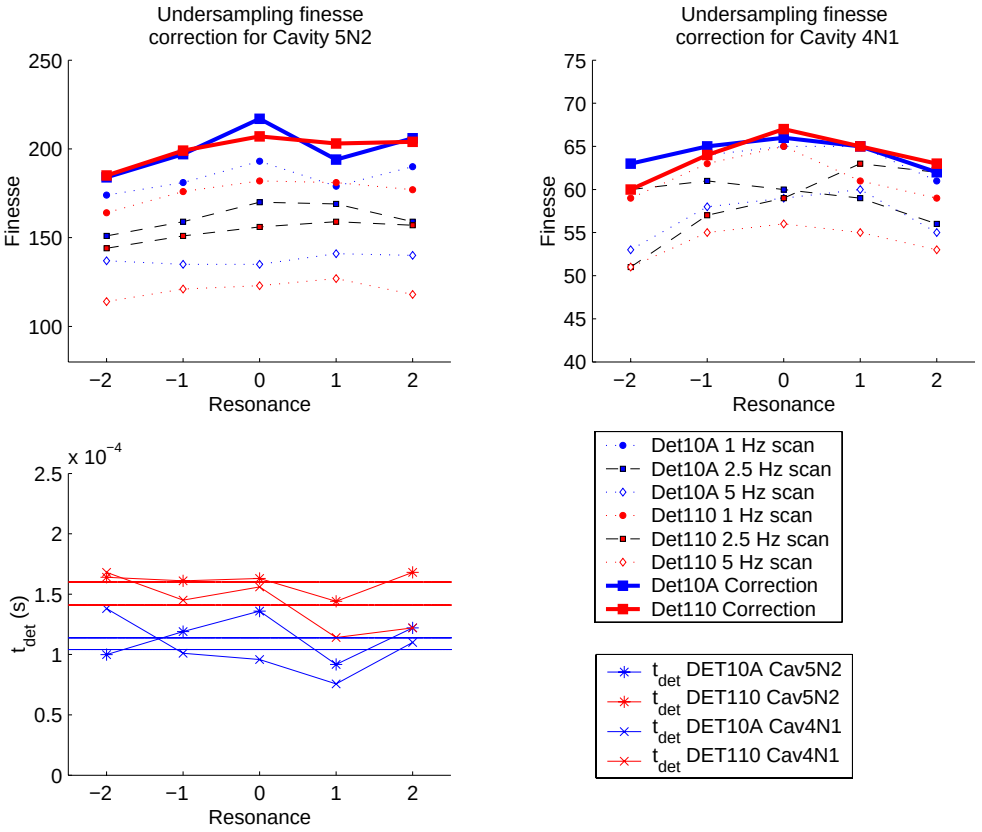

FIGURE 7.6: Result of finesse measurements for Cavity 5N2 and 4N1 made at different scanning rates and corrected values calculated using the simple Lorentzian model, top. Computed values for t_{det}, bottom left. Straight lines are the mean values.

7.2.4 Finesse results

Figure: 7.6 shows the measured finesse and the calculated values for F, labelled as "correction" in the figure. The model predicts a highest finesse for Cavity 4N1 of $F = 67$. As can be seen, there is little difference in the measurements for a cavity with such weak gratings, with the 1 Hz scan being just about resolved with the DET10A/oscilloscope detection system. The 2.5 Hz scans give the impression that perhaps there was a shift within the bandgap between the runs with each detector, but no effort has been made to change the plotting and these are the values used to calculate the correction. The calculated values for F are the same even if the peaks are shifted to look correct. Also, since the differences are relatively small, and the cavities are almost resolved, perhaps this is to be expected. The 5 Hz scans start to show separation in measured values, with the slower DET110 being the most equipment limited, as expected. The set of cavities containing Cavity 5N2 have the strongest gratings of the recent batch. It can be seen that the 2.5 Hz scans under resolve the resonance widths, as shown by the finesse measurements. This is the

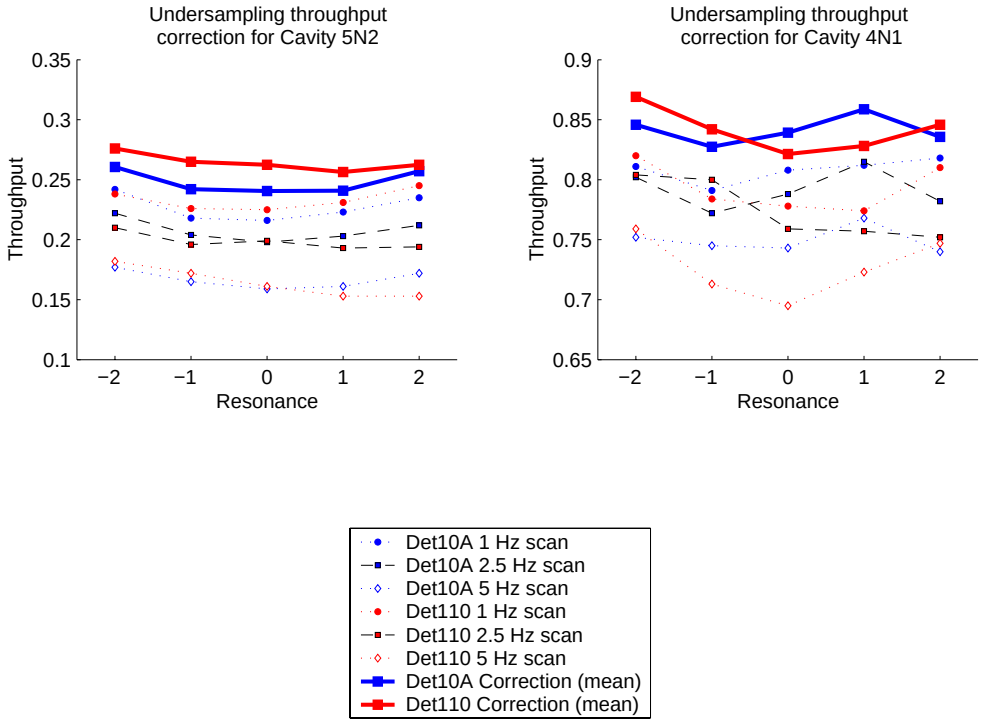

FIGURE 7.7: Throughput measurements for Cavity 5N2 and mean corrected values calculated using the simple Lorentzian model.

scan speed used for many of the previous experiments. The maximum finesse value measured using the DET110 detector is $F_{\text{meas}} = 156$, about the same as the value measured for the strongest gratings (Set 3) in the previous experiments (Table: 5.1). The model gives corrected values between 207 and 217 for the maximum finesse from measurements made using the two different detectors at different scan rates. Again the older (DET110) detector speed is shown to be slower.

The calculated values for t_{det} are also plotted in Figure: 7.6. The mean values calculated for the two detectors measured using the two cavities are plotted with straight lines. The values differ slightly depending on which cavity was measured, but there is separation between the calculated values, with the DET110 detector causing more broadening of the measured resonances compared to the faster DET10A detector. These mean values are used for the following throughput calculations.

7.2.5 Throughput correction

In Figure: 7.7 the throughput corrections for the cavities 4N1 and 5N2 are plotted, along with the original measurements. For each detection set-up the throughput

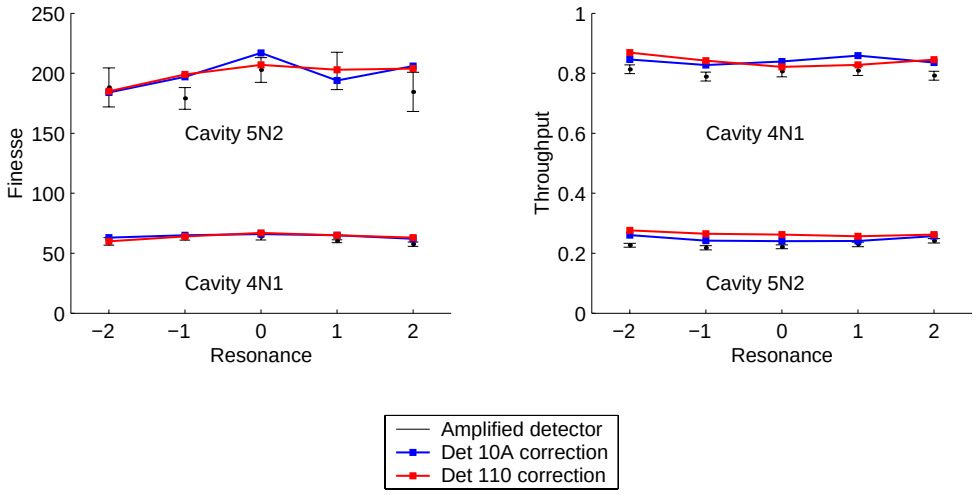

FIGURE 7.8: Finesse and throughput model corrections and amplified detector results (error bars). Error is SD of measurements.

corrections are calculated by averaging over the three scan rates for each resonance. Errors of ± 0.2 for cavity 5N2 and ± 0.3 for 4N1 can be given from the maximum spread about these mean values. There is good agreement in the model predictions from each detector for the throughput of each cavity, giving figures of $\tau \approx 0.25$ for cavity 5N2 and $\tau \approx 0.85$ for cavity 4N1.

7.2.6 Amplified detector agreement

The acquisition of an amplified detector (Thorlabs PDA10A) allowed for an experimental verification of the model predictions. The group's replacement oscilloscope (Tektronix DPO4034) was used for the measurements, as the LeCroy oscilloscope had been returned. However similar results had been obtained from finesse measurements made by both oscilloscopes on a number of cavities. The characterisation method used was the same as that used previously with the new set-up. Figure: 7.8 shows the results of these measurements plotted alongside the correction values displayed in Figs. 7.6 and 7.7. The error bars show the standard deviations in the measurements. Although there is a slight discrepancy in the throughput values, overall the simple model is in very good agreement with measured values. Scanning at different rates, 2.5 Hz, 25 Hz and 125 Hz gave similar finesse results for cavity 5N2 indicating that the amplified detector resolved any bandwidth limiting. Measurements for the new cavities using the amplified detector are given in Table: 7.1.

7.2.7 Results and comparison

In order to correct for the values given in Chapters 5 and 6 certain assumptions need to be made. Firstly, although the oscilloscope used previously had a bandwidth of 300 MHz, compared to bandwidths of 350 MHz and 400 MHz for the oscilloscopes used in the experiments detailed in this section, the amount of equipment broadening is taken to be equivalent. A similar detector (DET110) was used and we assume also similar coaxial lead lengths. The observation of similar equipment limited finesse measurements on cavities using the 350 MHz oscilloscope and the 400 MHz LeCroy oscilloscope would substantiate this. If Fig. 7.6 is inspected it would appear that more confidence can be placed in the highest mean value for t_{det} for the DET110 detector. This figure is calculated using the higher finesse cavity which exhibited clearer separation in the levels of equipment limited finesse and throughput. For these reasons a mean value of t_{det}=1.6×10^{-4} s is used for the correction, and detector bandwidth corrections to previous tables and figures are provided in Appendix A.

An additional consideration to take into account is the linewidth of the laser used. Even without any detection bandwidth limitations, the cavity response is actually a convolution of the cavity linewidth and the laser linewidth. With this in mind we can re-arrange Eq: 7.10 and include laser broadening (again taking this effect to be the result of linewidth addition) such that:

$$F_{\mathrm{real}} = \frac{t_{\mathrm{FSR}} F_{\mathrm{meas}}}{t_{\mathrm{FSR}} - F_{\mathrm{meas}}(t_{\mathrm{laser}} + t_{\mathrm{det}})} \ , \tag{7.13}$$

and similarly from Eq: 7.11

$$\tau_{\mathrm{real}} = \frac{t_{\mathrm{FSR}} + F_{\mathrm{real}}(t_{\mathrm{laser}} + t_{\mathrm{det}})}{t_{\mathrm{FSR}}} \tau_{\mathrm{meas}} \ , \tag{7.14}$$

where

$$t_{\mathrm{laser}} = \frac{\Gamma_{\mathrm{laser}}}{\mathrm{FSR}} t_{\mathrm{FSR}} \ , \tag{7.15}$$

and Γ_{laser} is the linewidth of the laser. Here the manufacturers quote "typical" linewidths of less than 500 kHz for both the Littman-Metcalf laser and the Littrow laser. For a cavity length of 5 cm with an effective index of n_1=1.457 at 780 nm, we find t_{laser} to be of the order of 10^{-5} s when scanning the wavelength at 2.5 Hz. In Figure 7.9 the actual finesse is plotted against measured finesse for values of $t_{\mathrm{det}} = 1.6 \pm 0.1 \times 10^{-4}$ s considering laser linewidths of 0.2 MHz, 0.5 MHz, and 1 MHz. As can be seen from the figure, for low finesse values the linewidth

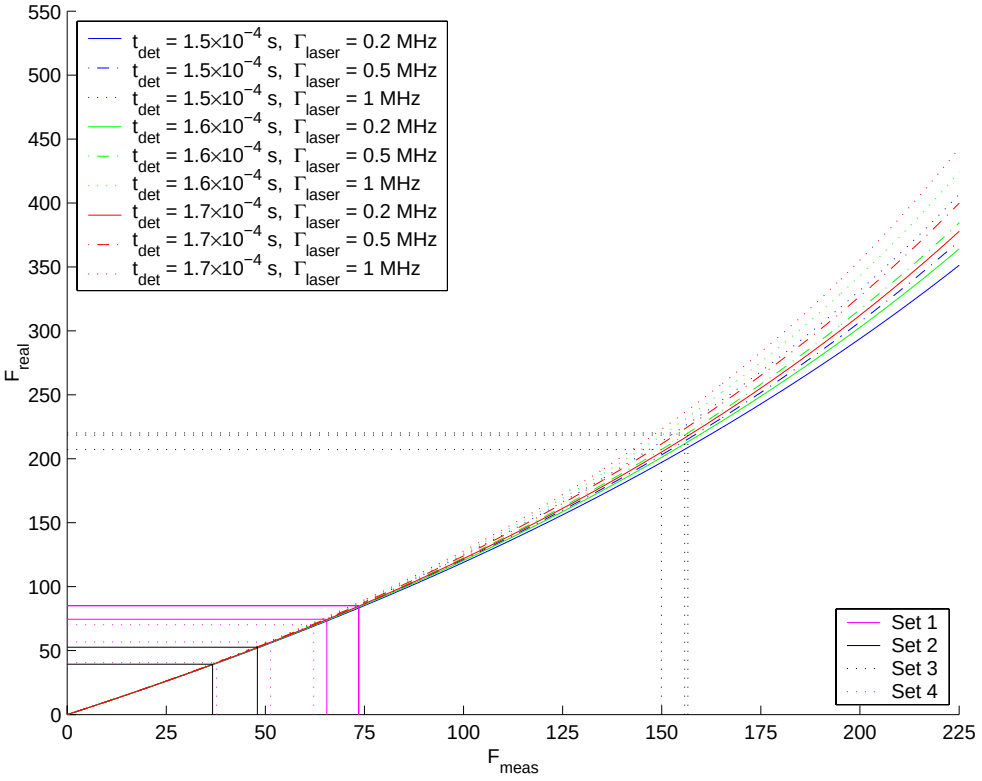

FIGURE 7.9: Finesse correction for different detector time constants and laser linewidths. Corrections to the finesse values for the first test cavities in PS750 fibre (sets 1-4, Table 5.1) are also indicated, taking into account a laser linewidth of 500 kHz.

and detector broadening make little difference, with the cavity response fairly well resolved. It is only at higher finesse values ($F > 80$, say) that we begin to see a difference, and it is here that differences in laser linewidth and detector response time start to become apparent. Included in the figure are the corrections to the finesse values for the first group of test cavities written in PS750 fibre (see Table 5.1), calculated with $t_{\mathrm{det}} = 1.6 \times 10^{-4}$ s and using a laser line width of 500 kHz.

The result of applying the correction procedure to the previous data from Chapter: 5 is such that we find increases in the grating coupling constants κ of 1.5 %, 1 %, 2.4 %, and 1.1 % respectively, for the cavity sets 1 to 4 given in Table: 5.2, meaning that there is still a good agreement with the transmission spectra measurements. However values for the loss per unit length α are reduced by between 20 % to 30 %. The trend in the annealing data (Chapter: 6) still follows the same pattern with the grating loss reduced to an even lower value which subsequently improves the ϵ values. Here we obtain a final value of $\epsilon = 0.75$ for cavity 3a.

Figure 7.10 shows the projected ϵ values (red contours), grating transmission and single pass loss for all the cavities and annealing data and includes data from the

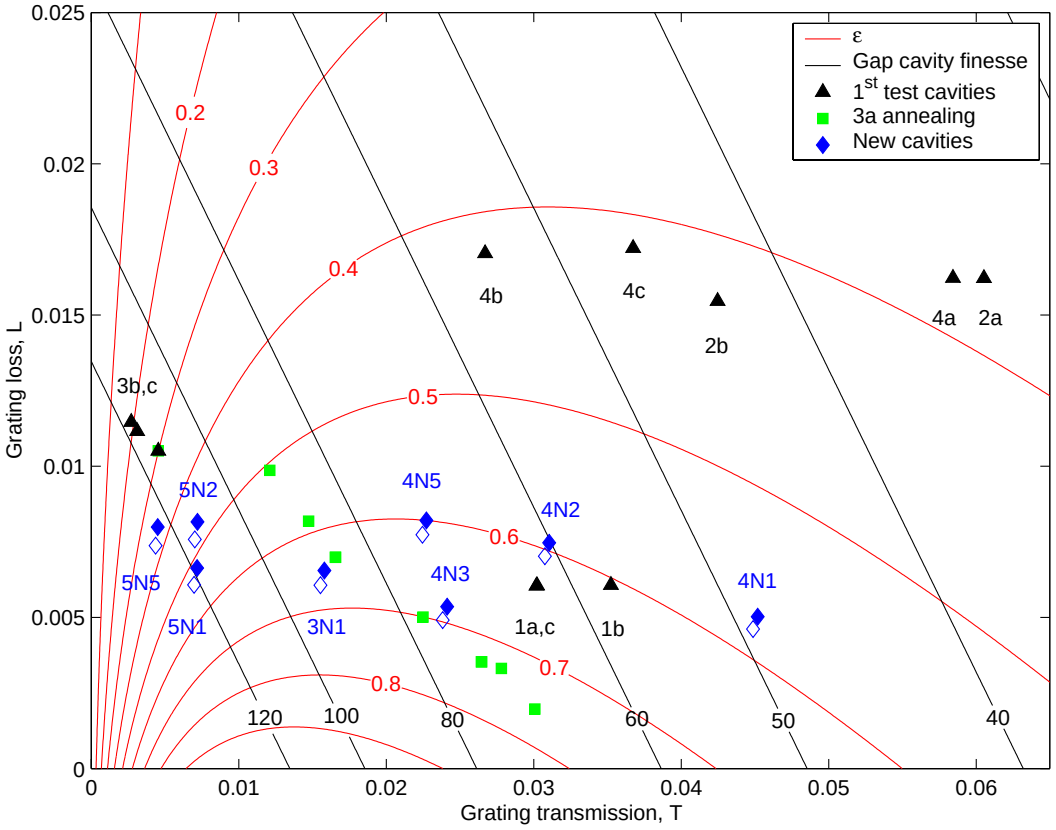

FIGURE 7.10: Cavity figure of merit, ϵ (red contours), and projected finesse for a 5 µm gap (black contours), showing corrected figures for first test cavities and cavity 3a annealing in old PS750 fibre, and measurements from the set of cavities in new PS750 fibre. Corrections for a 500 kHz laser linewidth are shown as open blue diamonds.

new set of cavities for comparison purposes. It can be seen that all of the gratings in the new fibre exhibit similar loss per pass, L. With the exception of cavities 3N1 and 4N1, the coupling constant κ is similar (around 640 m^{-1}) for all the cavities, so this may be expected. The values for the loss per unit length α (1.5 - 3.0 m^{-1}) appear to be lower for the gratings written in this new fibre. In order to illustrate the extent of the effect due to the laser linewidth, projected values for a 500 kHz laser linewidth are shown as open diamonds. Annealing of cavity 3a resulted in a final value of α=0.6 m^{-1} which is lower than the values for the new gratings and the concurrent increase in the figure of merit ϵ, to 0.75, indicates that a final device can be constructed for which the SNR of atom detection measurements will approach that of an ideal device, i.e., it will be sensitive enough for single atom detection. Also included in Fig. 7.10 is the projected finesse (black contours) for an introduced 5 µm gap for the cavities in question. These finesse values represent what would be expected for an absolute minimum coupling loss between the fibre arms after diffraction, light reflected from the fibre faces being reflected back into

the counter-propagating modes. This is included as a reference for gap cavity experiments discussed in the next chapter.

7.3 Conclusion

A new set of gratings written in replacement PS750 fibre exhibited loss per unit length values of $\alpha = 1.5$ m^{-1} to 3 m^{-1} which appear to be lower than the corrected values obtained for gratings written in the the previous fibre (4 - 5 m^{-1}). These corrected values for α have been found to be about 20 % to 30 % lower than originally calculated. However, amended values for the grating transmission are very similar to those measured previously. The resultant α value for the annealed gratings is now found to be almost the same as that calculated for gratings written at 1550 nm, and it would appear that single atom detection would not be hampered by material limitations, although annealing, in addition to that used by the manufacturer for stabilisation, would still be required.

Chapter 8

Micro-Optical Integration and Tuning (780 nm gap cavities)

This chapter is concerned with mounting the cavities and the physical implementation of the gap. The loss due to the gap is influenced by the geometry of the fibre, the preparation of the fibre end faces, and alignment. These issues are discussed here, in addition to phenomena arising from the gap introduction, and the additional complexity of the cavity spectra. Due to the relatively narrow bandwidth of the gratings, and the need for temperature stabilisation, tuning of the gratings will be necessary for a final device. Data from preliminary experiments in this direction is given.

8.1 Fibre parameters and gap loss

8.1.1 Fibre parameters

The photosensitive fibre used, Fibercore PS750, has a Germanium-Boron co-doped core and is single mode at 780 nm. The cladding is fused silica, having a refractive index of $n_{\text{clad}} = 1.4537$ at 780 nm. Using the supplied numerical aperture (NA) of the fibre we attain a core refractive index of n_c =1.459. A calculation of the core radius, a_c, can be made using the specified cut-off frequency, λ_{cutoff}:

$$a_c = \frac{2.405\lambda_{\text{cutoff}}}{2\pi\text{NA}} \tag{8.1}$$

which gives a resultant core diameter of 4.0 µm. Using this value we can calculate the mode field radius [120], w_0:

$$\frac{w_0}{a_c} = 0.65 + 1.619V^{-3/2} + 2.879V^{-6} \tag{8.2}$$

which gives a mode radius $w_0 = 2.6$ µm, or a mode field diameter (MFD) of 5.2 µm. A profile measurement (Photon Kinetics refractive index profiler[1]) of the fibre gave a core diameter of 4.0±0.5 µm, in agreement with the calculated value, and the calculated index difference between the cladding and core of $\Delta n = 4.9 \times 10^{-3}$ is close to the measured profile value of $\Delta n = 4 \times 10^{-3}$. We note here that this is an estimate of the effective index difference for a step index fibre, since the index profile of the core is not flat but has a central depression due to an outward diffusion of the dopants during fibre manufacture. Precision is also restricted by equipment focusing.

From a weighted average of the power confined within the core ($\approx 70\%$), and the power in the cladding, we can estimate an effective index of $n_{\text{eff}} = 1.457$ for 780 nm light propagating in the fibre. Additionally a value of 19.4 dB km^{-1} was quoted for the fibre attenuation coefficientat 780 nm, which equates to a single pass loss of the order of 10^{-4} for a 5 cm cavity, several orders of magnitude below the other loss mechanisms considered, and therefore can be considered to be negligible.

8.1.2 Gap loss

The inclusion of the gap into the cavity immediately introduces new issues regarding alignment, quality of the fibre face, or the angle of the cleave/polish, all of which introduce loss into the system. In free space it is possible to manipulate each side of the gap cavity through six degrees of freedom, allowing correction for any deviation of the fibre faces from the perpendicular, relative to the fibre axis. However once mounted, several of these degrees of freedom become lost.

Unfortunately the measurement of these additional losses is not completely straightforward. Although the loss due to the gratings and the transmission loss can be calculated from closed cavity measurements prior to the introduction of the gap, the actual gap loss is related to the resonance conditions within the coupled cavity system. As has been described previously, the coupling of the cavities results in a non-uniform FSR and, furthermore, this also affects the intensity of the light

[1]Many thanks to Rob Standish for this measurement

field within the gap. The atom-light coupling and the gap loss are related to this intensity. The extremes of these values can be calculated by considering a hypothetical cavity with arms of exactly the same length. If the arms are resonant at the frequency of the input light then there is a node at each fibre face when the cavity is resonant. By matching the electric field and its gradient across the fibre/air boundary it is found that the magnitude of the field in the gap is such that

$$|E_{\text{gap}}| = n_1 \, |E_{\text{fibre}}| \ , \tag{8.3}$$

however if there is an anti-node at the fibre faces then the two amplitudes are equal.

An idea of the "average" loss that can be expected can be gained from the hypothetical case. The cavity intensity loss rate can written as [92]

$$2\kappa_{\text{gap}} = \frac{c}{L_{\text{cav}}} \left(\frac{d}{2z_0}\right)^2 \left|\frac{1+n_1-(1-n_1)e^{jn_1k_0L_{\text{cav}}}}{2n_1}\right|^2 \tag{8.4}$$

$$= 2L_{\text{gap}}\text{FSR}, \tag{8.5}$$

where L_{gap} is the single pass gap loss, since the loss rate encompasses light travelling in both directions. Considering a resonant cavity with equal arms of overall length 5 cm and a 5 µm gap then, using the preceding fibre parameters, we find $L_{\text{gap}} = 1.2\%$. Note here that the fibre geometry influences the loss rate through the term $z_0 = \pi w_0^2/\lambda$ so a larger mode size reduces the loss rate.

8.2 Fibre end face preparation

Although it appears straight forward to go directly from a closed cavity to a gap cavity, this is unfortunately not necessarily the case. Fibre cleavers in general produce cleaves which are quite adequate for fusion splicing, and normal fibre procedures, but not necessarily good enough for a gap cavity. Since the Fresnel reflections from the fibre faces need to match the modes travelling in the opposite direction as closely as possible, then the faces need to be perpendicular to the fibre axis. Originally, the cavities were bisected using York cleavers which seemed to keep the fibre end faces near to perpendicular, but occasionally removed a small chip from the edge of the fibre. The advantage of these cleavers was that they seemed ideal for bisecting long pieces of stripped fibre, leaving two similarly prepared end faces, mainly since the fibre is held on both sides during cleaving.

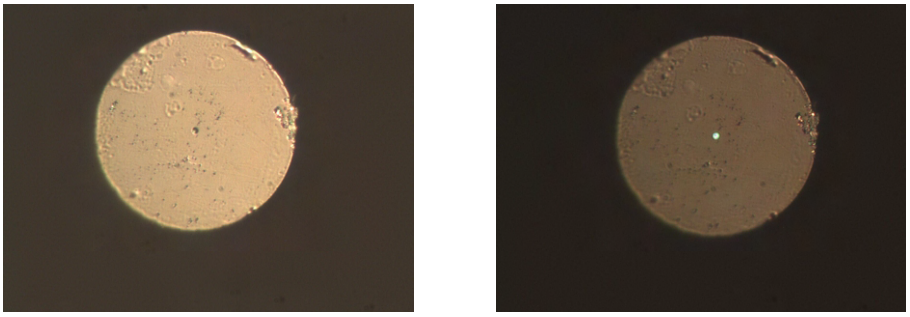

FIGURE 8.1: Result of extended polishing with fluid (prior to cleaning)

The replacement Fujikura cleaver is extremely good for preparing the end of a fibre, but not so good for cutting a long fibre in half. Since the fibre is rigidly held only on one side, this leaves room for error. On the plus side, this cleaver can remove a short length of fibre from each side of the cavity in order to clean up the fibre ends if necessary, provided the original cavity was long enough to do so. However, both of these cleavers are specified to give average cleave angles of about 0.3° which can be problematic.

The only way to correct for bad cleaves then becomes polishing. The hand polishing was carried out using a fibre polishing puck and an adaptor made to hold the fibre. A soluble glue was used to hold the fibre firmly during polishing. Various grades of polishing paper were used, down to a grain size of 0.3 µm. A polishing extender was used in conjunction with the finest paper to provide a flat fibre facet, and between each step the fibre face was cleaned, and inspected with a fibre microscope. The fibre and adaptor were then soaked in acetone to remove the glue and the fibre was washed in alcohol, acetone, and distilled water. The procedure was then repeated for the other side of the cavity.

At the time it was not possible to obtain polishing paper with as fine a grain as had been used previously, but the additional use of a polishing fluid appeared to produce good fibre face surfaces. Prolonged polishing with a polishing extender, however, can produce unwanted dimples in the core, because the germanium-boron doped core is softer than the cladding. Figure: 8.1 shows the result of two minutes of polishing with paper and polishing fluid before cleaning. For this reason the final paper and liquid polishing step was kept to a minimum.

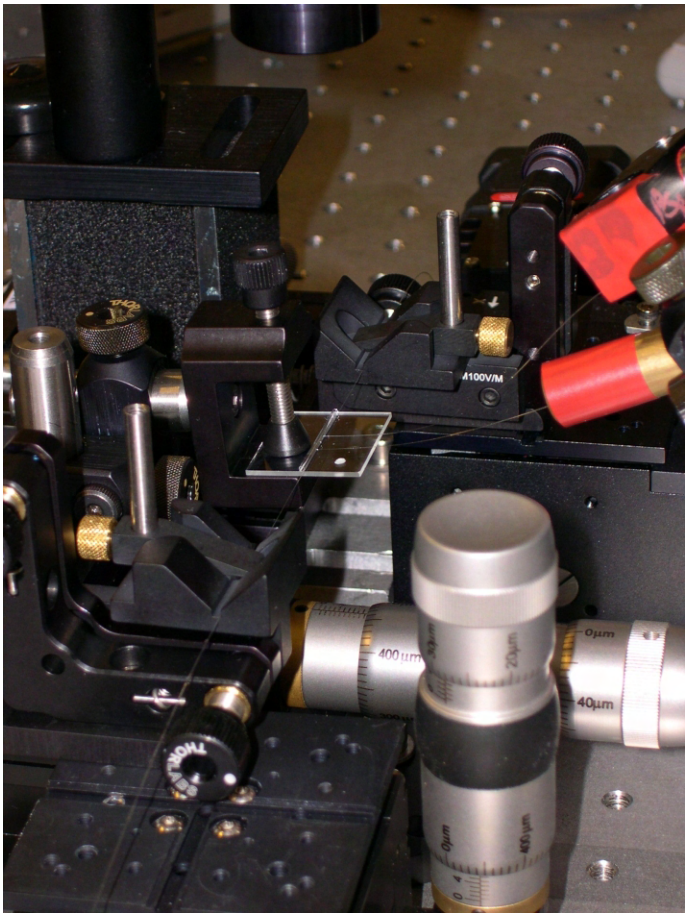

FIGURE 8.2: Fibre transmission experiment

8.3 Fibre to fibre coupling

To get an idea of the losses involved an experiment was conducted to see how the transmission between two fibres changed with fibre separation. A glass capillary tube was glued to a microscope slide, forming a v-groove between the slide and the capillary, shown in Fig. 8.2. Two fibres were cleaved and then mounted on stages at each side of the slide parallel with the capillary, with the fibres kept in the groove by using two other pieces of fibre as tension springs. This allowed the fibres to be kept parallel as the stages were separated. The results of the coupling are shown in Figure: 8.3. The black line shows a theoretical curve for the Fabry-Perot formed between the fibre faces generated using the matrix product found at the end of Subsection: 3.2.1. The maximum coupling (at resonance) is described

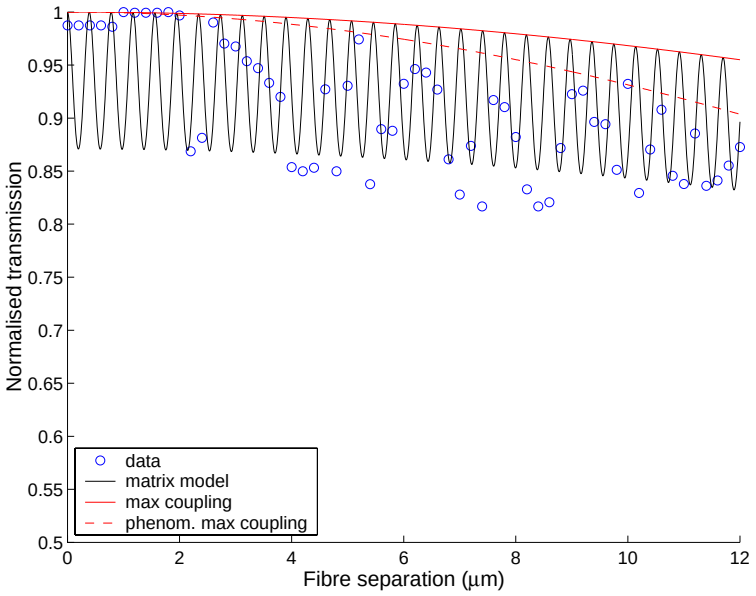

FIGURE 8.3: Direct transmission between two fibres in a groove. The black curve shows the theoretical transmission for the Fabry-Perot formed between perfectly parallel fibre faces. The solid red curve defines the maximum coupling when the gap is on resonance. The dashed red curve shows the comparative experimental maximum coupling, calculated using a phenomenological fit to the data (blue circles).

by the continuous red line

$$T = \left(\frac{w_0}{w(z/2)}\right)^2 = \frac{1}{1+(z/2z_0)^2} \tag{8.6}$$

where z is the fibre separation. As can be seen from the plot, the loss due to longitudinal separation is not large enough to account for the total loss in transmission.

Saruwatari and Nawata [121] modelled the coupling between a semiconductor laser and a single-mode fibre by calculating the mode overlap when lateral and angular offsets are included (in addition to longitudinal separation). For our purposes, we allow the spot size of the laser beam waist to be the same as the fibre mode radius, and consider the laser focus to be the face of the transmitting fibre. We assume a Gaussian transmitted beam, and any ellipticity of the emitted beam due to the cleave angle of the fibre is neglected. The coupling between the fibres can be described by

$$\eta = \left(\frac{w_0}{w(z/2)}\right)^2 \exp\left(-\left(\frac{w_0}{w(z/2)}\right)^2 \left\{\frac{x_0^2}{w_0^2} + \frac{\pi^2\theta^2(w^2(z)+w_0^2)}{2\lambda^2} - \frac{x_0\theta z}{w_0^2}\right\}\right), \tag{8.7}$$

where w_0 is the spot size of the fibre, $w(z) = w_0\sqrt{1+(z/z_0)^2}$ is the emitted beam

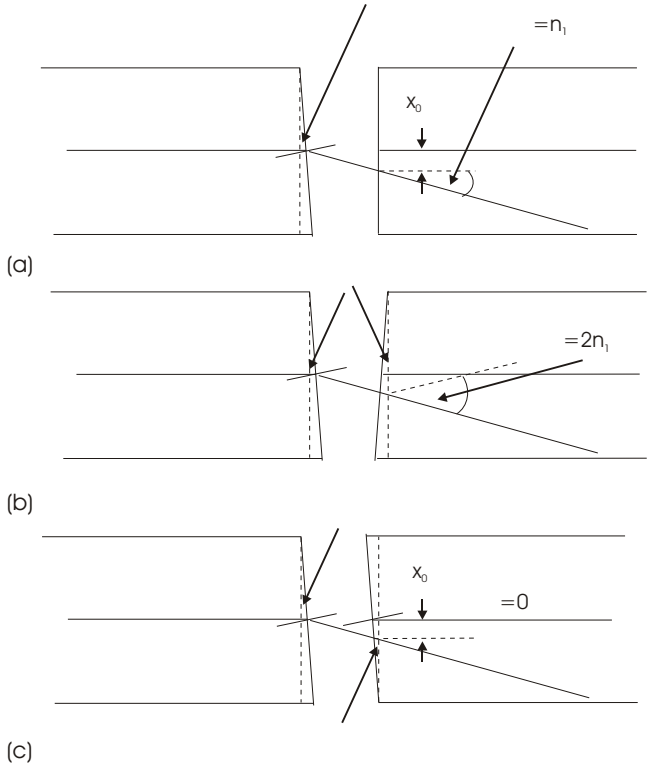

FIGURE 8.4: Possible cleave geometries in the xz-plane. (a) The left-hand fibre is cleaved at an angle β from the perpendicular, with a perpendicular cleave on the right-hand fibre, leading to an angular offset, $\theta = n_1\beta$, and a lateral offset x_0, with n_1 the effective index of the fibre. (b) Both fibres have the same cleave angle, β, but are rotated by 180° relative to each other about the longitudinal z-axis. This is approximately equivalent to the case in (a) with double the offset angle and a similar lateral offset. (c) If the fibre faces have the same cleave angle, but are parallel, then the acceptance axis and the beam axis are parallel, but a lateral offset is still present.

waist, x_0 is the lateral offset between the beam axis and the axis of the accepting fibre, θ the angle between the beam axis and the accepting fibre axis, and z, the longitudinal separation.

Since the fibres are constrained in the groove we can assume any lateral offset between the fibre axes to be negligible, so the majority of the extraneous loss derives from the cleave angles of the faces. This does, however, result in a lateral offset between the axis of the beam entering the second fibre and the axis of the second fibre. Figure: 8.4(a) shows the simplest case. The left hand fibre is cleaved at an angle β from the perpendicular and the right hand fibre has a perpendicular cleave. So, considering this angle to be small, then this is equivalent to having the first fibre rotated at an angle $\theta = n_1\beta$ with respect to the second, where n_1

is the effective index of the fibre. The lateral offset, x_0, is related to θ and the longitudinal separation, z, of the centres of the fibres:

$$x_0 = z \tan\theta \ . \tag{8.8}$$

Physically, the centres of the fibres cannot be brought together if only one fibre has a cleave angle that differs from the perpendicular, and if the fibres are kept parallel, but experimentally, one fibre can bow slightly to butt these faces together. If the fibres are cleaved, and not polished, then we can assume that both fibres have the same cleave angles. The greatest loss will occur if one fibre is rotated about its axis by 180° relative to the other fibre, as illustrated in Figure: 8.4(b). The result is approximately equivalent to the case where one fibre has double the cleave angle, β, and the other has a perpendicular face, with the lateral offset, x_0, being approximately the same. In the third case, shown in Fig. 8.4(c), the fibres are oriented in the same way as before they were cleaved. In this case there is still a lateral offset, dependent on fibre separation, but the acceptance axis of the right hand fibre and the beam axis are parallel ($\theta = 0$). Between the extremes of cases (b) and (c), when the fibres are rotated between 0° and 180° with respect to each other, then for small cleave angles we can expect that the exponential in the coupling equation Eq: 8.7 will contain additive terms concerning angular and lateral deviations in both the x- and y-directions.

So, if we consider the x-axis only, then using Eqs: 8.8 and 8.7 we can write

$$\begin{aligned} \eta &\approx \left(\frac{w_0}{w(z/2)}\right)^2 \exp\left(\frac{-1}{w^2(z/2)}\left\{z^2\tan^2(\theta) + z_0^2\theta^2 + z^2\theta^2/2 - z^2\theta\tan\theta\right\}\right) \\ &\approx \left(\frac{w_0}{w(z/2)}\right)^2 \exp\left(\frac{-1}{w^2(z/2)}\left\{\left(\frac{1}{2}z^2 + z_0^2\right)\theta^2\right\}\right) \ , \end{aligned} \tag{8.9}$$

i.e. the coupling between the fibres is the product of the longitudinally separated fibres, and a decreasing exponential of the form $\exp(-(\alpha z^2 + C)/w^2(z/2))$.

The initial fibre separation will differ depending on the orientation of the fibre faces and, furthermore, there is uncertainty in the initial position since the fibres may be under slight compression. The first points in Fig: 8.3 indicate that the latter may be a possibility here. In order to calculate the additional loss, in light of these uncertainties, the coupling was approximated to

$$\eta = |Q|^2 \exp\left(\frac{-\alpha z^2}{w^2(z/2)}\right) \ , \tag{8.10}$$

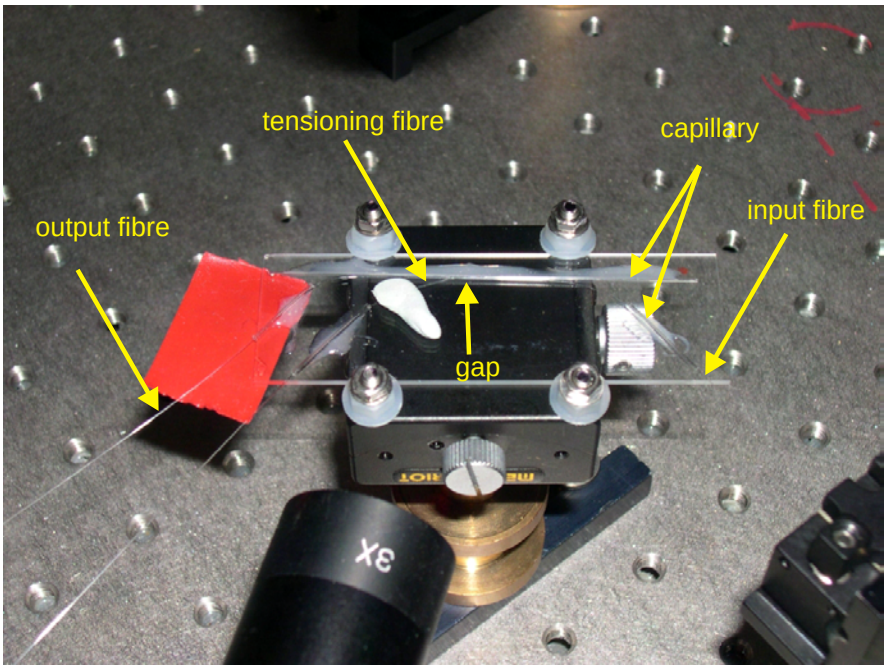

FIGURE 8.5: Initial gap cavity test mount

for some constant, α, and by using the product of η and $(1+R^2)/(1+R)^2$ a least square fit could be made to the data. The resultant phenomenological fit to the maximum coupling is shown in Fig. 8.3 by the dashed red line. The difference between the theoretical maximum transmission, and the maximum transmission from the fit, is about 1 % at 5 µm separation, i.e. there is an additional 1 % loss due to misalignment.

8.4 Mounting schemes

8.4.1 Capillary and slide

As a first attempt for gap cavity alignment a groove was formed between a glass substrate and a glass capillary tube, mirroring the method used by Constable et al. for their light force trap [122]. Initially this was tried using a microscope cover slip as a substrate, but this was found to be too flexible so was replaced with a microscope slide. An image of the set-up is shown in Fig. 8.5. "Araldite" was applied to the slide using another microscope slide in order to form a straight glue line, enabling the capillary to be pushed against this, avoiding contamination of the groove.

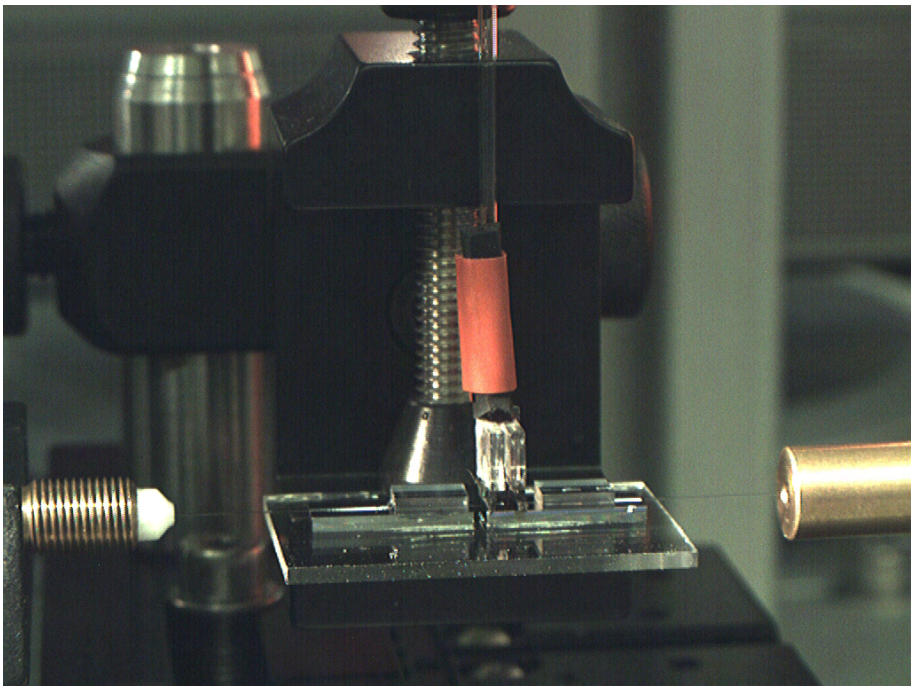

FIGURE 8.6: Mounted gap cavity in silicon v-grooves. A Y-shaped clamp holds each fibre arm down around the gap.

The two sides of the fibre cavity were guided into the groove using a further two capillaries. Tension in the fibre was used to keep the fibres in the groove, but there was a slight misalignment caused by the fibre coating on one side of the cavity. Rather than contaminate the fibre face using a chemical stripper to remove this excess coating, or risk breaking the fibre by physically stripping the coating, an additional fibre was used on one side to force it into the groove.

It was possible to mount a cavity using two of the gratings written into the SM750 fibre (Section: 5.1). With the fibres touching each other a finesse of 100 was recorded. Friction problems made it difficult to adjust the fibre gap. Additionally, although only for testing purposes, the glass capillary would not be an option for use in a device since there is no access to the gap. For these reasons this direction was discontinued.

8.4.2 Silicon v-grooves

Standard single mode fibre silicon v-grooves (Oz Optics) were ordered. These were rectangular shaped silicon, 1 cm by 0.5 cm, and 1 mm deep. The single groove runs the length of the chip, is 138 µm deep for half of the chip length, to accommodate stripped fibre, and then widens to accommodate the fibre coating.

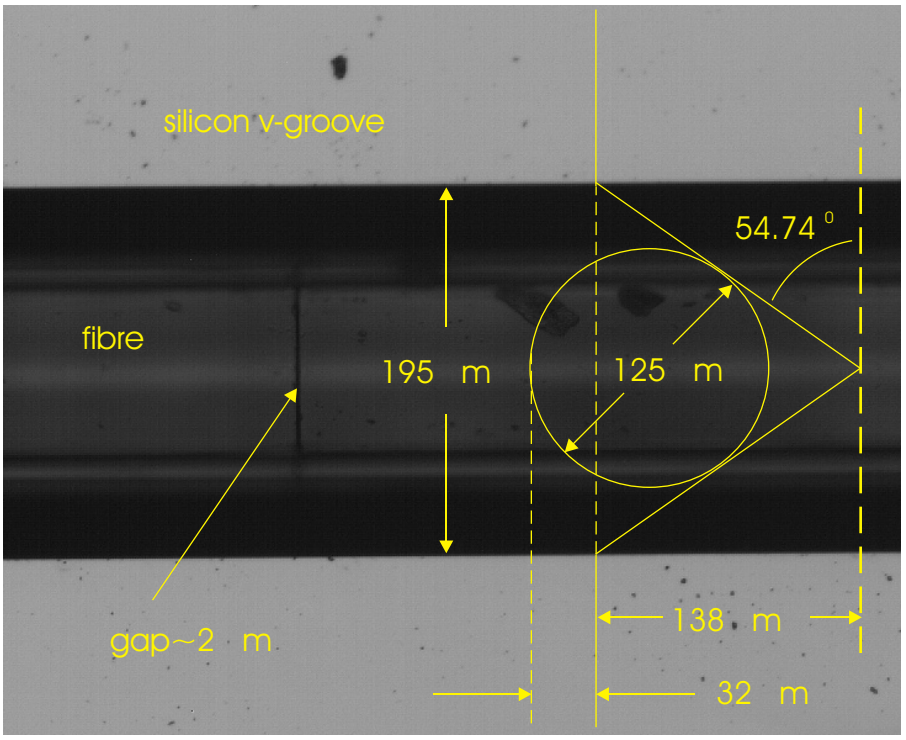

FIGURE 8.7: Image of fibre and gap in silicon v-groove chip (gap, $d \approx 2\mu$m). Overlaid schematic shows rotated side elevation of groove and fibre. The fibre protrudes about 30 µm above the surface of the chip.

This leaves only 5 mm of groove which can be used to align and mount the ends of the fibres and the small gap. At the time it was not possible to obtain longer v-grooves which would have made things simpler.

Since the grooves were short they were used in pairs, end on, and separated by about a millimetre, so that one of the v-grooves could support one fibre, with the end of that fibre just overlapping into the next groove. The second fibre could be positioned alongside in the groove. The grooves were glued onto a microscope slide with UV glue and were aligned by stringing a taut fine wire through the grooves and pushing downwards slightly. The glue was set by irradiating it from below. The placement of the v-grooves with respect to the substrate is shown in Figure: 8.6. Here the gap is beneath the clamp, and small lids are glued in place to hold the fibre.

The substrate containing the v-grooves is clamped to a central stage, and each side of the cavity is held in a fibre chuck which is clamped in a gimbal mount attached to another stage. The left hand stage has step motors and piezo actuators for fine position adjustment. A Y-shaped clamp (see Fig: 8.6), made from glass and rubber, holds each side of the cavity down around the gap. This Y-shaped clamp

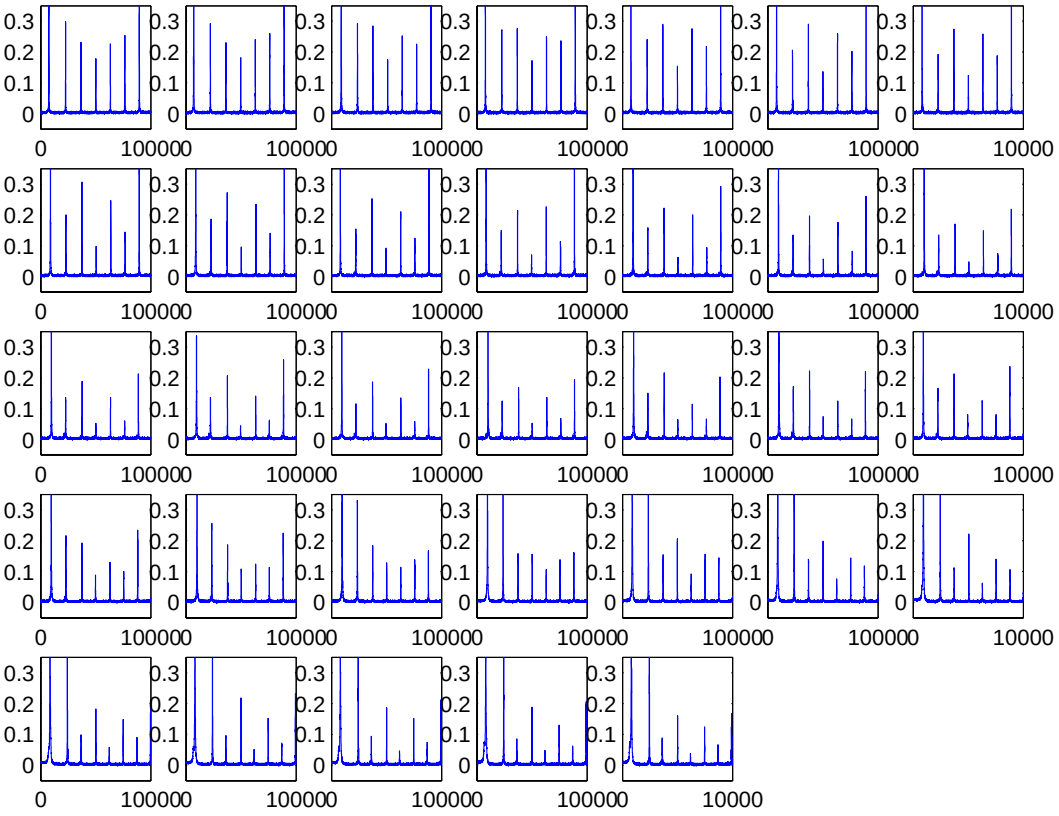

FIGURE 8.8: Central resonances for cavity 5N2 for increasing gap size. From left to right, top to bottom, gap size increases from zero to 8λ (6.2 µm) in steps of $\lambda/4$.

is controlled with a probe station. With the clamp in place, a view of the gap can still be obtained via both a vertical camera and a camera opposite to the substrate. Figure: 8.7 shows an image of the fibre cavity arms mounted in a v-groove and separated by approximately 2 µm. An overlay shows the groove geometry, with the fibre core positioned 30 µm below the surface of the chip.

8.5 Gap cavity experiments

In order to get a qualitative feel for how the resonances changed with gap size, cavity 5N2 was cleaved, prepared, and mounted in a small silicon v-groove. The two sides of the cavity were aligned and butted together. The transmission spectra of the central resonances were recorded at separation intervals of $\lambda/4$, as set on the stage controller. In order to compare the same resonances, the central wavelength of each sweep was also altered by increasing the DC ramp voltage, to keep the original resonances in position on the oscilloscope. The results are shown in Figure: 8.8. It can be seen that there is a lot of change between the relative heights of the

resonances, for instance the heights of the centre and far right hand side resonances drop considerably relative to the others over the full 6.2 µm range.

8.5.1 A mounted gap cavity

Figure: 8.9 shows an example of how the interplay of the three coupled cavities affects the position and size of the gap cavity resonances. Cavity 5N1 was cleaved and the fibre faces polished. The cavity was mounted and glued into the v-groove, but was also still clamped, with a gap of approximately 5 µm. The data for each resonance here is sparse, since the span encompasses several resonances and the number of data points is kept the same. The low number of data points within the FWHM of each resonance means that the Lorentzian fits are not highly accurate and there is some question regarding the relative peak amplitudes. However, finesse measurements of $F > 100$ were recorded when scanning over just two resonances, so the finesse figures above the resonances are a good representation. The finesse values were calculated from the average FSR values each side of the resonance in question. These FSR figures are included beneath the transmission curve. Characterisation of the cavity before the inclusion of a gap showed a finesse of 220, with grating transmission of T=7.6×10^{-3}, and grating loss of L=7.0×10^{-3}, so a measured finesse of around 100 indicates an additional gap loss of 1.5 %.

8.5.2 Other mounted cavities

Besides the example mounted cavity above, several other cavities were mounted in a similar way with differing degrees of success. Several attempts at cleaving and polishing cavity 3N1 only resulted in a finesse measurement of F=55 for a 5 µm gap. This pointed towards a gap loss of about 3.5 %. Indications of a slight dimpling in the core of one fibre may possibly have contributed to the loss, although there were also problems with the type of polishing paper used in this case. Unfortunately the cavity was broken during its removal from the mount. This prompted the use of fibre chucks rather than clamping the fibre directly to the gimbal mounts.

Cleave angles caused a lot of problems when working with the 4 mm grating cavities. A fusion splicing machine was used to estimate the cleave angles. Each end of cavity 4N2 was individually cleaved, and cleave angles of 0.17° and 0.29° were read from the machine. These are only estimates, since slight corrections are

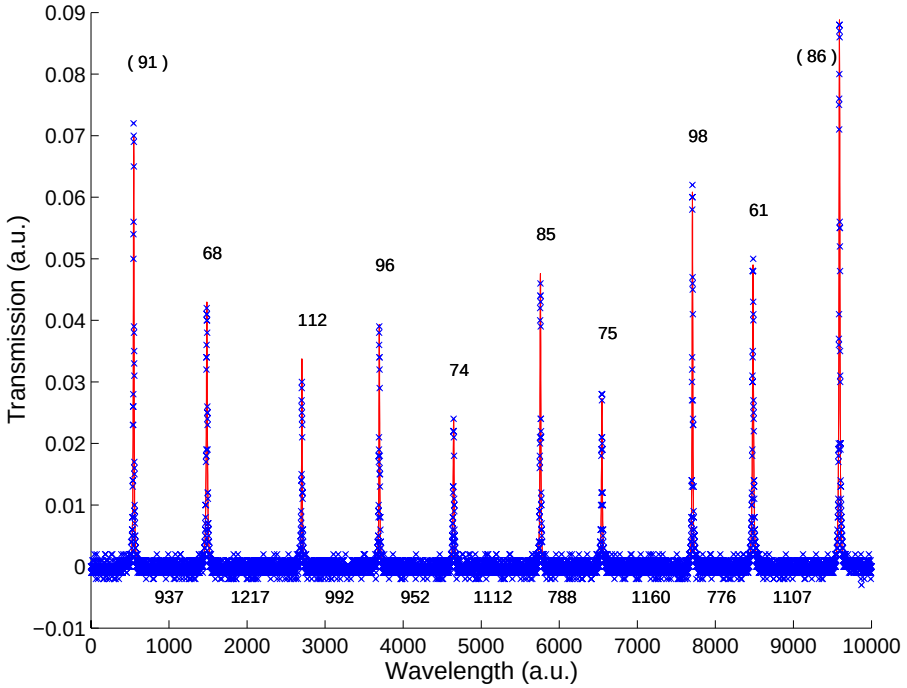

FIGURE 8.9: Spectrum of centre of cavity 5N1 with a 5 µm gap (sparse data). Figures above the resonances are representative of the cavity finesse. Lower figures are FSR values (a.u.).

needed for angular misalignments in the machine grooves. After several rounds of polishing a gap loss calculated at 5 % was the best result recorded.

The gratings for cavity 4N5 were separated by 10 cm which allowed more attempts at getting good fibre facets. The initial cleave angle was over 3°. The end cleaving of the two cavity sides resulted with one good cleave, and one with a face angle of nearly half a degree. Both sides were polished, but measurements with the fusion splicer were not made in order to protect the fibre as much as possible. A face angle measurement of 0.2° had been measured previously for a polished fibre, but it is not known if this is indicative of the angles to be expected, a "one off" case, or whether the alignment angle of the fibre into the splicer was relatively large, and the reading was misleading. Since the fibre cavity arms are uncoated and brittle, and it was necessary to keep the polished fibre faces clean, it was felt that measuring every polished fibre face with the splicer was not a good idea. A minimum of handling and clamping was attempted since breakages were so common. Again the gap loss appeared to be around 5 % for a 5 µm gap.

Cavity 5N5 was another 10 cm cavity so again there was a little more fibre to play with. A borrowed York cleaver was used, and angular measurements of over one degree were made with the splicer. Re-cleaving with the Fujikura cleaver reduced these angles, but angles up to half a degree were still measured. A finesse

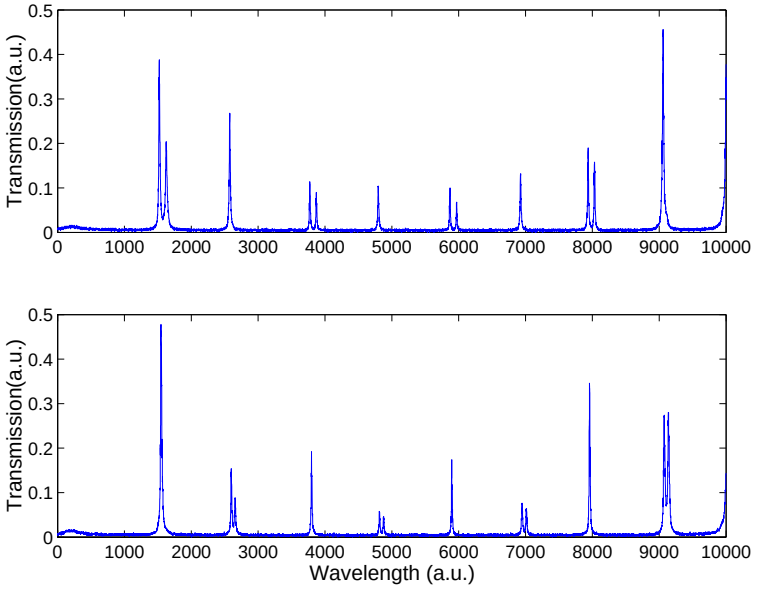

FIGURE 8.10: Gap birefringence in cavity.

measurement of 250 had been made on the closed cavity but there was a lot of noise in the measurement with large uncertainties. However the gratings were expected to be very strong.

Due to the grating strength the throughput for the gap cavity was very low. It was not possible to get a good fit to the cavity resonances to make measurements, so the cavity was annealed to reduce the grating strength. Using the figures from the closed cavity scan, and previous annealing experiments, a temperature of 200°C for a time of two hours was estimated to produce a gap cavity finesse of about 60, when considering a 5 µm gap and allowing for a 3 % gap loss. Finesse figures of greater than 80 were measured with free space alignment and a slight gap between the fibres. The cavities were mounted on v-grooves and glued and clamped. After removing the clamp, and taking the substrate and fibre away from the mounting equipment, it was still possible to record finesse values of 65.

8.6 Polarisation

With closed cavities there is no problem with polarisation issues. With the use of a polarisation controller the state of polarisation of the light entering the cavity is altered, so that only one of the two resonant eigenmodes are excited. The controller itself consists of three fibre coils, which act approximately as 1/4-, 1/2-, and 1/4-wave plates, giving full control of the input state polarisation. By observation of

the scanned cavity signal, the second set of fringes due to the orthogonal resonance can be eliminated, leaving all the power in the one mode of interest. The actual state of polarisation within the cavity is unknown but the resulting transmitted intensity is the same as if the light was linearly polarised.

With the addition of a gap there is an additional mechanism for birefringence. If the faces of the fibres are not parallel then there will be rotation of the polarisation vector on exiting one fibre and on entering the next. Depending on the relative face angles, there will be a combination of diffraction loss, which can also affect the polarisation by reducing one component of the polarisation vector, and also gap birefringence due to different path lengths, as the light traverses the gap. Generally, any unwanted resonance fringes can be suppressed by altering the input polarisation, but if the gap birefringence is extreme, then the resonance spectrum becomes more complicated. Figure 8.10 shows an example of these polarisation effects. A change in the input polarisation can only change the relative intensity of one of the components of each resonance. In the top plot the central resonance($\lambda \sim 5000$) has one component, whilst the two resonances either side are split. The bottom plot shows the opposite effect after the input polarisation has been changed.

The example shown here is believed to be caused by an angle between the fibre axes in addition to the cleave angles of the fibre. It is possible to extend the matrix model given in Section: 3.2 to include the different polarisation components, and by choosing the right parameters it is possible to replicate the above behaviour. However, the model can only give a qualitative representation due to the arbitrary choice of parameters which cannot be directly related to the actual fibre geometry.

8.7 Piezo Tuning

It will be necessary to develop a system to tune the cavity gratings to the laser frequency and to stabilize against temperature fluctuations. For an FBG cavity, a change in temperature leads to both a change in refractive index, and thermal expansion, causing a change in grating period (and change in cavity length). The refractive index change dominates and is the main contributor to wavelength shift [123], which is of the order 0.01 nm $^{\circ}C^{-1}$.

8.7.1 Bragg wavelength change with strain

The change in grating Bragg wavelength with strain can be given as [48]

$$\Delta\lambda_B = (1 - p_e)\lambda_B\epsilon \tag{8.11}$$

where the strain, $\epsilon = \Delta Z/Z$, and the photoelastic term

$$p_e = \frac{n_1^2}{2}\left(P_{12} - \mu\left(P_{11} + P_{12}\right)\right) \ . \tag{8.12}$$

Experimental values for the strain tensor coefficients, P_{12}, P_{11}, and μ, have been given as 0.252, 0.113 and 0.16, respectively, for single-mode fibre at 633 nm [124]. Although the fibre dopants and geometry are different to the fibre used here, using these parameters with a refractive index of 1.457 gives $p_e \approx 0.21$.

8.7.2 Experiment

The use of a piezo stretcher to lengthen a fibre grating, and thereby change its wavelength, has been mentioned previously in Chapter: 5, however here it is considered in terms of tuning the grating rather than just a method to investigate each grating individually. An experiment to quantify the change in wavelength with piezo voltage was carried out using an early weak grating written in the SM750 fibre (not previously detailed in this thesis). The grating was attached to a piezo stretcher with the attachment points 2.4±0.1 cm apart. The stretcher lengthened the grating by expansion of a piezo stack. In order that the stretcher would lengthen the fibre, hence increasing the grating wavelength, it was put under tension which originally increased $\lambda_{\max}$ by around 0.5 nm. The transmission of the grating was recorded, using the method detailed in Subsec. 5.1.3, and Fig. 8.11 shows the result of this experiment. Since only the central wavelength, $\lambda_{\max}$, was required, a simple Gaussian fit was used for the transmission spectra (a), and a linear fit was used for the wavelength voltage plot (b).

The manufacturer's specification for the elongation of the piezo stack is 11.6±2.0 µm at 100 V. If we assume that the piezo extends linearly with voltage, then an extension of 3.7±0.6 µm can be expected at 32 V. Making a further assumption that the strain on the grating is the same as that for the total length of stretched fibre, then

$$\epsilon = \frac{3.7 \pm 0.6 \times 10^{-6}\text{m}}{2.4 \pm 0.1 \times 10^{-2}\text{m}} = 1.6 \pm 0.3 \times 10^{-4} \ ,$$

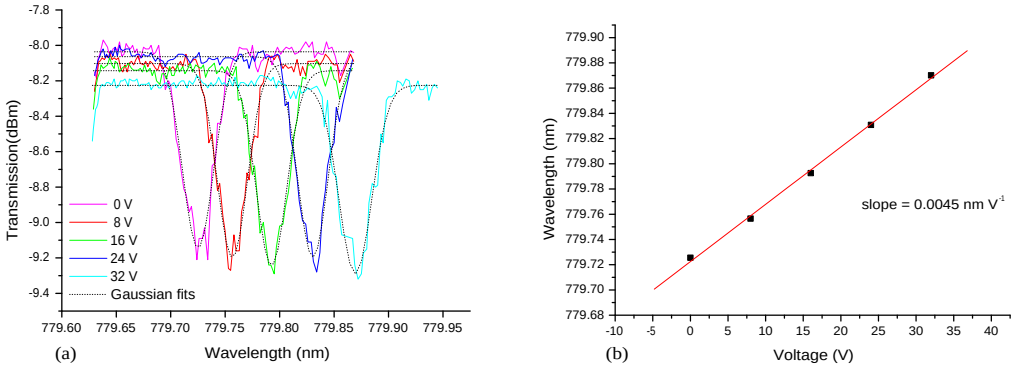

FIGURE 8.11: Grating tuning experiment: (a) transmission for different piezo voltages; (b) central wavelength against voltage.

leading to $\Delta\lambda = 0.10 \pm 0.02$ nm using Eq: 8.11. This is slightly less than the wavelength shift recorded here, with initial and final wavelengths of 779.73 nm and 779.87 nm, respectively.

A closer inspection of Fig: 8.11 raises a couple of issues. Firstly, in (a) the transmission outside of the grating bandgap appears to drop as the strain is increased. A small proportion (about half) of this apparent loss is caused by a slow drift in laser power, over time, which is evident when inspecting the normalisation signals. Since the fibre is attached by small glue points on one side of the fibre only, this may lead to a non-uniform strain along the fibre length. The mechanism that causes the apparent extraneous loss is unknown, but may be a form of micro-bend loss due to this non-uniform strain, and additionally to a slight bending in the stretcher. More recent cavity stretchers have been constructed so that they are constrained to move along one axis only, and the fibre is also clamped rather than glued, in order to prevent any such problems. The second issue concerns the slight non-linearity in the wavelength-voltage graph (b). The probable cause for this is a non-linear piezo response with voltage.

The piezo stack used in this experiment would not be ideal for use in an actual device since the piezoelectric ceramic layers are coated in a plastic, preventing attachment along the stack's length. Although it would be possible to fabricate a small stretcher, it is expected that this type of piezo stack would outgas under high vacuum. However, it is possible to obtain uncoated piezo stacks onto which the grating could be glued.

8.8 Locking

In order to lock the cavity, working with a second frequency, or at a different time-scale, will be necessary to avoid unwanted compensation for dispersion shifts caused by the presence of an atom. Either using a second laser frequency [62], or switching off stabilisation during measurement [63] are both common methods used in cavity QED experiments. Tuning can be accomplished using a piezo electric stretcher on one arm of the cavity. Vibration stability is also of concern, but isolation from the environment should suffice.

8.9 Conclusion

A single pass gap loss of 1.5 %, close to the theoretical minimum value of 1.2 %, has been achieved for a cavity with an approximate 5 µm gap, mounted using two short silicon v-grooves. Fibre end preparation would appear to be the main issue involved with optimising the mounting procedure, although the use of a single longer v-groove is likely to improve coupling between the fibre sections, and additionally simplify the mounting operation. Using piezoelectric stacks it is possible to tune the Bragg wavelength of the cavity gratings, or the cavity length, in order to change the desired wavelength, or stabilise against temperature fluctuations. The introduction of a gap into a closed fibre resonator results in three coupled cavities and a more complex resonant structure. At any particular resonance the interplay of these cavities results in a particular linewidth, and cavity throughput, due to the losses involved. However, the use of piezoelectric tuners will allow for the selection and optimisation of any particular resonance, compensating for the initial mounting arrangement.

Chapter 9

Fluorescence Detection

Originally, work on a fluorescence detector was carried out in parallel with the fibre cavity work, however this was discontinued after the fire. This chapter describes the preliminary investigation along this path, concluding with a short report of results and directions taken by a selection of research groups working in this area. The idea behind the fluorescence detection system is simple in concept: light resonantly scattered from an atom is to be collected by a multimode fibre in the vicinity of the atom. The initial concept for the detector consists of an illuminating tapered lensed fibre (TLF) and a multimode collection fibre, see Fig. 9.1, mounted orthogonally onto a substrate. The atom is to be positioned at the focal point of the fibre lens, and is to be illuminated with resonant light of angular frequency ω_a. After excitation with resonant light an atom will spontaneously emit radiation, and the detection of this emitted radiation gives evidence of the atom's presence.

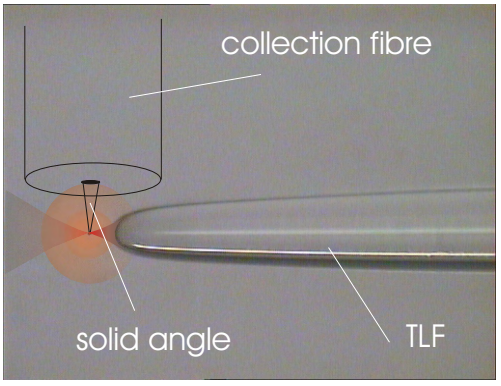

FIGURE 9.1: Fluorescence detection: an atom, positioned at the focus of a tapered lensed fibre (TLF), is to illuminated with resonant light. Light scattered from the atom is to be collected by a multimode fibre.

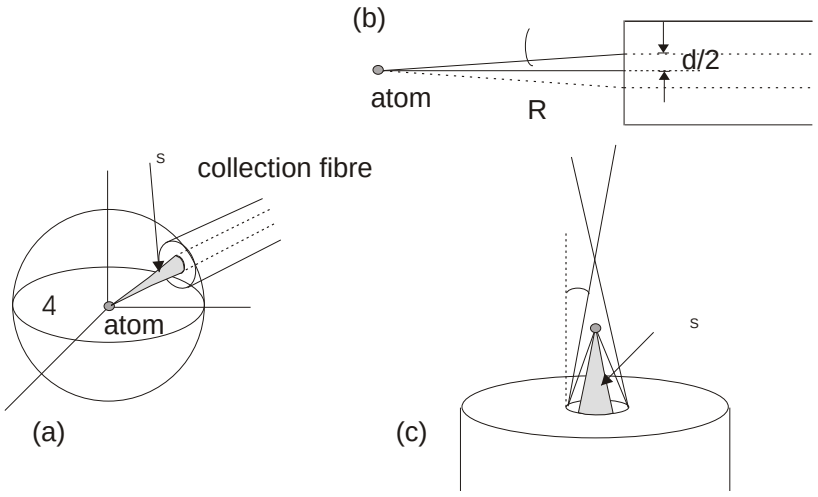

FIGURE 9.2: Fluorescence detection schematic. (a) The light captured by the collection fibre is approximately given by $\Omega_S/4\pi$, where $\Omega_S = 2\pi(1-\cos\alpha)$ is the solid angle subtended by the collection fibre core and, (b), $\alpha = \tan^{-1}(d/2R)$. (c) The maximum solid angle, Ω'_S is governed by the acceptance angle of the fibre, β.

9.1 Model

A basic model considers the free-standing case, where the atom has no constraints from guidance potentials, and the light from the atom is radiated symmetrically. The fraction of light entering the collection fibre is approximately given by $\Omega_S/4\pi$, where $\Omega_S = 2\pi(1-\cos\alpha)$ is the solid angle subtended by the collection fibre core, and $\alpha = \tan^{-1}(d/2R)$, as illustrated in Fig. 9.2 (a) and (b). There is however a maximum solid angle which is governed by the acceptance angle of the fibre, β. If $\alpha > \beta$ the collected light is limited to that of the solid angle Ω'_S, shown as the shaded region in Figure 9.2 (c). This maximum is therefore

$$\Omega'_S = 2\pi(1-\cos\beta)\ ,$$

where β is given by NA $= \sin\beta$, NA being the numerical aperture of the fibre. The typical multimode fibre considered here has an NA of 0.275, which means that the photons scattered into this solid angle represent about 2% of the total number scattered. This fibre has a core diameter of ~ 60 µm, requiring that the fibre is positioned a maximum distance of about 100 µm from the atom for optimal collection ($\alpha \geq \beta$).

If the natural decay rate of the excited atomic state is 2Γ then for high intensities and strong saturation the rate of spontaneous photon emission approaches Γ,

because the atom has equal probability of being in either the ground or excited states. The energy emitted per second is $\hbar\omega_a\Gamma$ and the power, W_f, collected by the fibre is

$$W_f = \frac{\hbar\omega_a\Gamma\Omega_S}{4\pi}.$$

For this simple example, if we consider a standard multimode fibre with an NA of 0.275, $2\Gamma/2\pi = 5.98$ MHz, and the collection of light to be at maximum, then the number of photons collected is $\Gamma\Omega'_S/4\pi = 3.6 \times 10^5 s^{-1}$, resulting in an average power of the order 10^{-13}W. However, if we consider the case where the light emitted from the TLF is linearly polarised, but the polarisation direction is unspecified, then on average the light collected from the driven dipole is also dependent on the angle between the axes of the TLF and the collection fibre (see Appendix C). In this case it can be shown that having the TLF and the collection fibre perpendicular to one another is not optimum.

This estimation concerns an essentially "free" atom, and further corrections will need to be made when dealing with the situation where the detection system is mounted on the atom chip with the atoms within guiding potentials. The main consideration here will be the avoidance of spin-flips which will lead to the ejection of an atom from the potential well of the guide wire. In this case, the polarisation of the pump light must be considered, and controlled, so it is expected that polarisation preserving fibre will have to be used for the tapered fibre lenses. It must also be noted that Fresnel reflection is ignored (we can make the assumption that the collection fibre has an anti-reflection coating). Furthermore, for a full calculation of the detection efficiency, the quantum efficiency of the detector must also be taken into account.

9.2 Characterisation

A selection of Nanonics TLFs were characterized, both to compare their physical dimensions, and to observe the emitted beam (focal length, beam diameter, beam shape). The company supplied four different lens types with specified working distances of 3 ± 1 µm, 5 ± 1 µm, 20 ± 2 µm and 22 ± 2 µm, with respective beam diameters 1.2 ± 0.3 µm, 1.2 ± 0.3 µm, 4.2 ± 0.5 µm and 4.2 ± 0.3 µm. By imaging through an optical microscope, and comparing with graticule images at the same magnification, the diameters of the fibres were measured at certain positions along their lengths (0.4mm, 0.8mm and 1.2mm from the TLF tip respectively) indicated by the diameters A, B and C in Figure 9.3(a).

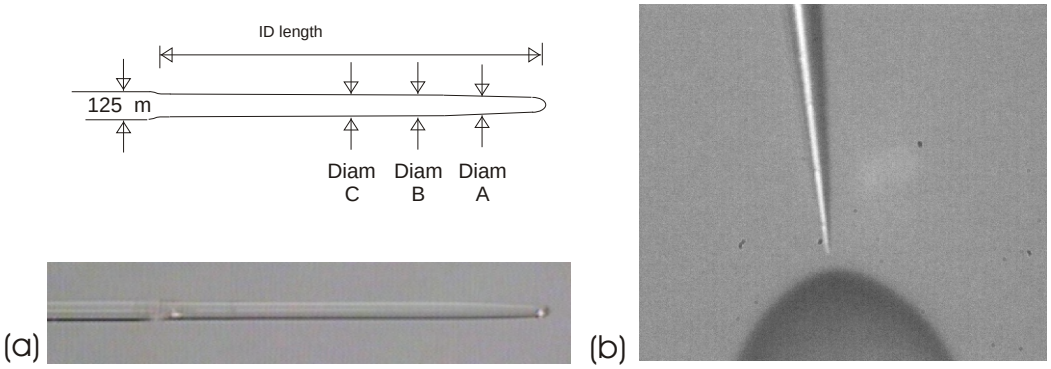

FIGURE 9.3: (a) Physical measurement of tapered lensed fibres, (b) TLF and SNOM tip.

Two different methods were used for analysing the beams emitted from the TLFs. Firstly, using a microscope with a 50X objective, the beams were imaged, with a Watec (WAT-902B) camera connected to a frame grabber on the computer. Images were taken at several planes of focus, separated by 5 µm steps, starting from the end of the fibre. The peak intensity was kept as uniform as possible by monitoring the histogram on the frame grabber software, and attenuating using a pair of polarisers and neutral density filters. This was done in order that the response from the camera for each frame was as similar as possible.

The second method entailed using a SNOM tip (see Figure 9.3(b)) to sample the light field at various positions within the beam, in order to build up a selection of cross-sectional images taken at various points along the longitudinal (z) axis. This technique has been reported by Butler et al.[125] who used it to characterise the intensity distribution of the field emerging from an optical fibre. Three fibre tips were pulled using a tapering machine, then coated with aluminium by evaporation. A LabView program was written to both drive a three-dimensional motorised stage so as to complete a number of raster scans, and also to take the readings. The readings themselves were taken using a femtowatt receiver connected to a multimeter. The stages and meter were controlled via a GPIB port on the computer. Using grabbed images from cameras mounted above and to the side of the experiment, it was possible to simultaneously observe vertical and lateral views of both the TLF and the SNOM tip from within the program to aid initial alignment.

Each data set comprised of multiple raster scans recorded at incremental distances from the TLF, with each cross-section commonly containing 1681 sampled points

Fibre	ID length(μm)	Diameter A(μm)	Diameter B(μm)	Diameter C(μm)
1	2271	101	111	111
2	2915	98	111	111
3	3984	81	98	98
4	3775	86	95	97
5	3574	92	103	105
6	4605	94	112	114
7	3798	90	101	98

TABLE 9.1: TLF physical measurements

from an area of 100 to 225 µm^2. This process took several hours to collect but was fully automated, so did not require constant monitoring. The Labview program itself also displayed the data for each slice as an intensity graph and saved the data to a spreadsheet file. Sub-routines were written, within the LabView program, to fit the various cross-sectional scan data to Gaussian intensity profiles in both the x and y directions (the beam from the TLFs is considered to be approximately Gaussian) for both beam analysis methods.

9.2.1 Physical measurement

The physical measurements for the 22 micron working distance fibres are shown in Table: 9.1. Since the TLFs will need to be mounted onto a substrate, with the beam axis at the same height as the centre of the collection fibre, then it will be necessary to take into account the differences in their physical dimensions. The main concern would appear to be the marked variance in the "ID length", since this effectively indicates the part of the lens where the diameter is less than 125 µm. However the precision needed is not as stringent as that for the fibre cavity.

9.2.2 Beam analysis

Figure: 9.4(a) shows an intensity profile of a longitudinal slice through the beam for one of the tapered fibre lenses (TLF6 from Table: 9.1), derived from sampling the beam with a SNOM tip. By fitting a Gaussian intensity profile to each cross-section it was possible to obtain a beam width (radius), $w(z)$, at each distance from the lens. Fitting these beam widths to the longitudinal profile of a Gaussian beam produced a resulting beam waist, $w_0 = 2.1 \pm 0.1$ µm. Here an M^2[126] value was introduced to allow for the deviation from a TEM00 mode, and this was found to be 1.5. A datum point was calculated by comparing images taken of the SNOM

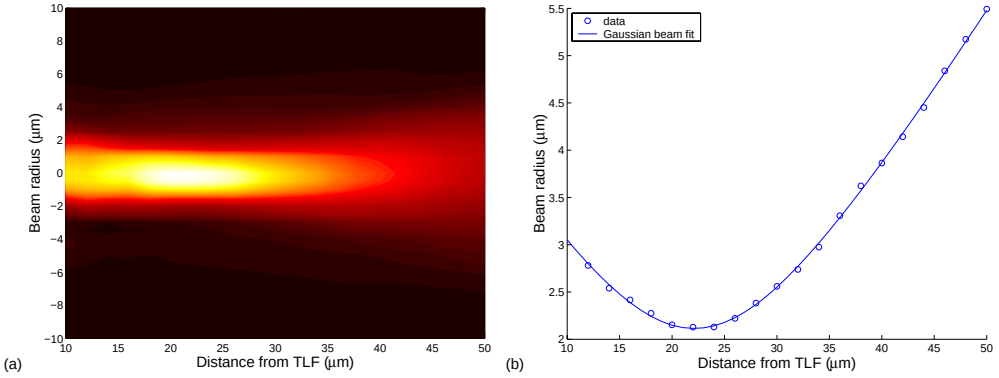

FIGURE 9.4: (a) SNOM scan intensity profile of longitudinal slice through beam from TLF 6; (b) beam radius, w, measurements of TLF 6 with longitudinal fit to Gaussian beam.

tip and the TLF, with images of a microscope graticule taken under the same magnification in the same focal plane. A check on this was possible by deriving a second pixel/µm scale from images of larger TLF-SNOM tip separations. This resulted in a focal distance of 22±1µm, with the main contribution to the error being due to uncertainty in the position of the end of the SNOM tip due to image resolution. The distance axes in Figs: 9.4(a) and 9.4(b), which display the beam radius data, have been offset to reflect this focal distance.

Initially, the data gathered from the imaged beams appeared to show some sort of double waist, which was thought to be caused by interference effects. Furthermore, the short focal length lenses also exhibited diffraction rings, which again may have been caused by the imaging process, although the microscope objectives have good anti-reflection coating. Further inspection, and comparison with the data from the SNOM scans, identifies the former effect to be due solely to the initial focal plane of the microscope.

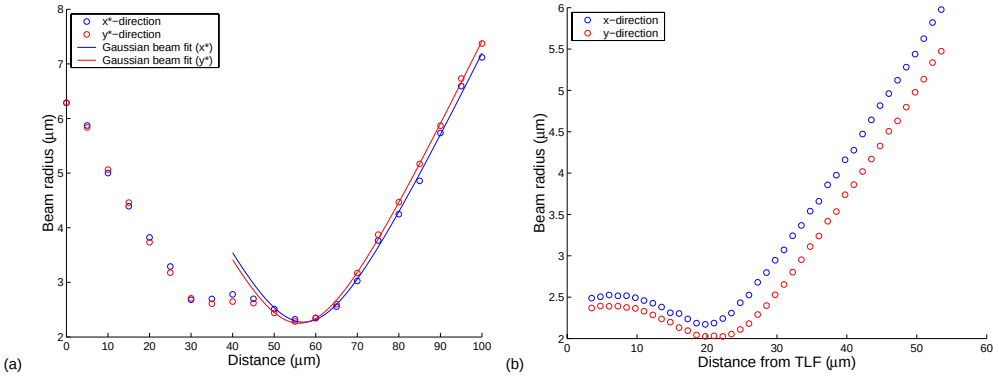

FIGURE 9.5: (a) beam radius calculated from microscope images of the emitted beam from TLF 1; (b) comparative SNOM scan measurements of the same lens for two orthogonal directions.

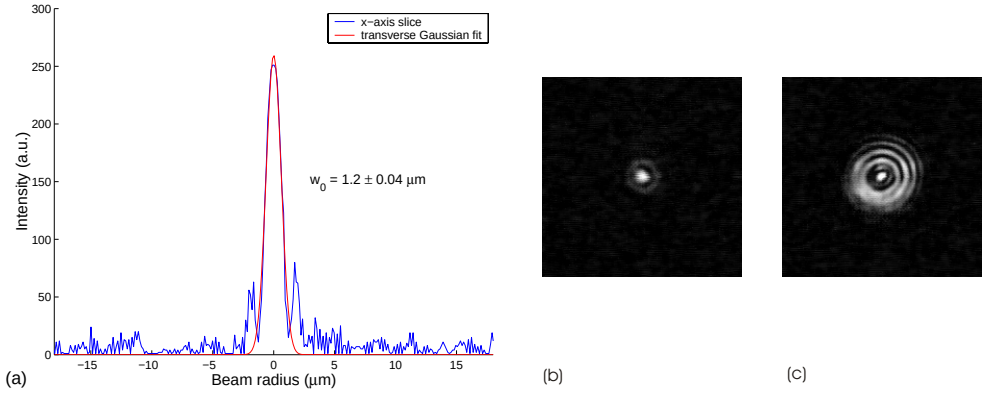

FIGURE 9.6: (a) Gaussian intensity fit to centre of short focal length TLF; (b) beam image at lens focus; (c) beam image 20 µm past lens focal point.

Fig. 9.5(a) shows a plot of beam radius measurements against distance for a nominal 22±2 µm working distance, 4.2±0.3 µm spot diameter fibre (Fibre 1 in Table 9.1), calculated from Gaussian intensity profile fits of cross-sectional images obtained using the microscope and camera. The uncertainty in position of the end of the fibre is clearly illustrated. A longitudinal Gaussian beam approximation is not good in the near-field zone close to the lens, which can be expected, however past the focus, the fit appears quite good for a beam with an M^2 value of 1.46. Plot (b) of the same figure displays scaled data from a SNOM scan of the beam from the same fibre lens. A degree of ellipticity is present, which may well have been masked in the image analysis method, purely due to the rotation of the fibre with respect to the fixed x- and y-axis slices (i.e. there is no direct relation between the x- and x*-directions between the two plots (a) and (b)).

An alternative explanation for this may be that the SNOM scan z-axis and the beam axis were not parallel, and awareness of this will be needed when using this method in the future. A measurement taken from an image of the initial position of the SNOM tip, with respect to the TLF, gives a datum point 3.5±0.3 µm from the end of the fibre, giving a working distance in agreement with the manufacturer's specifications. This offset has been incorporated into the graph.

Fig. 9.6(a) shows a cross-sectional intensity profile of one of the short focus tapered lensed fibres at the focus, taken from a microscope image. A Gaussian fit to the central peak gives a radius of 1.2 µm, again in agreement with the manufacturers specifications. This was recorded at a distance of 4 µm but an absolute datum point is unclear. The image (b) is taken in the focal plane of the TLF, whilst further from the lens the ring system becomes quite pronounced and, for this reason, in addition to the short working distance, it was decided not to use these short focal lenses for the detection system. Fig. 9.6(c) shows an image focused in

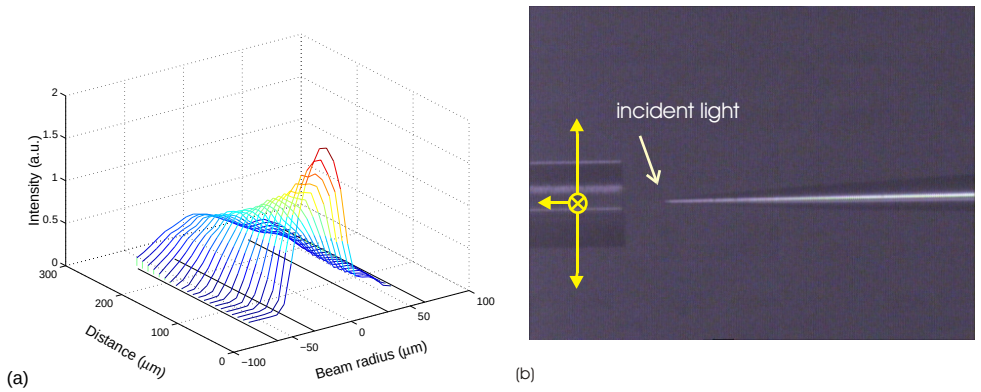

FIGURE 9.7: (a) Collected light intensity with respect to SNOM scatterer position. (b) Multimode collection fibre scan direction and SNOM scatterer.

a plane 20 µm from the TLF focus. Beam width measurements made on the other tapered lensed fibres from Table 9.1 showed good consistency. Since the SNOM scan method appeared to verify the manufacturer's specifications, it was felt that the same set-up could be used for aligning the fibres for a fluorescence detection system.

9.3 Scattering experiments

Since the end of a SNOM tip is generally sub-micron, this was thought to offer a small scattering centre. An experiment was carried out to measure the dependence of the scattered signal due to the position of the scatterer, relative to the collection fibre, and also to see what the apparent effects of the acceptance angle of the fibre would be. In order to try to capture light scattered from the end of the SNOM tip, the multimode fibre was aligned co-axially facing the SNOM tip, and the TLF was introduced at an angle slightly less than 90° from the collection fibre (the direction of the incident light is shown in Fig. 9.7(b)). The light collected from the multimode fibre was measured using a femtowatt receiver connected to a Keithley multimeter.

The collection fibre was scanned in a similar fashion to the TLF characterisation scans, so that the scattered light was sampled in a number of planes at set distances from the fibre. A cross-section of the collected light intensity is illustrated in Fig. 9.7(a). Here the solid black lines are extensions of the fibre diameter and the position of the fibre core. The initial datum was about 50 µm from the collection fibre face, and the scan ranged over an area 120 µm by 120 µm, and 200 µm in the longitudinal direction.

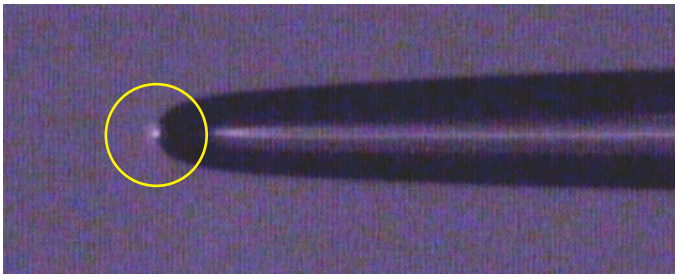

FIGURE 9.8: Scattered light from end of tapered fibre lens, circled.

An initial observation is that the light falls off immediately with distance and does not stay constant within a distance of 100 µm from the collection fibre as might be expected from the simple argument given at the beginning of this chapter. An explanation for this could be due to the fact that the light scattered from the SNOM tip is not scattered isometrically. Since the light is scattered from points on a truncated aluminium coated cone this could certainly be expected. Furthermore, to accurately calculate the collection efficiency of the multimode fibre, the overlap of all supported modes would have to be calculated. A second observation concerns the acceptance angle of the fibre. The intensity at 5 % of the maximum was calculated for each slice in the longitudinal direction, and this was found to describe an acceptance angle of only 8°, as against the 16 ° which might be expected for the NA of 0.275. Again this may be explained by the directional nature of the scattered light.

Of more concern is the asymmetry of the signal. A double peak had been observed previously and found to be due to a broken SNOM tip but this is not the case here. The slice depicted in the Figure: 9.7 is in the vertical direction, and the "bump" evident to the right of the graphs is due to the TLF. Initially this was thought to be due to light reflected back to the tapered lens from the scatterer and then into the collection fibre, and it is possible that a component of this signal is due to this. However, a closer inspection found that there is light scattered directly from the TLF itself. When the power of the incident light was increased light scattered from the end of the TLF was clearly seen on the monitoring cameras. Figure: 9.8 shows this for a laser power of 2.5 mW.

9.3.1 TLF scattering

To see if the light directly scattered from the TLF was coupled into cladding modes of the multimode collection fibre, these cladding modes were stripped using

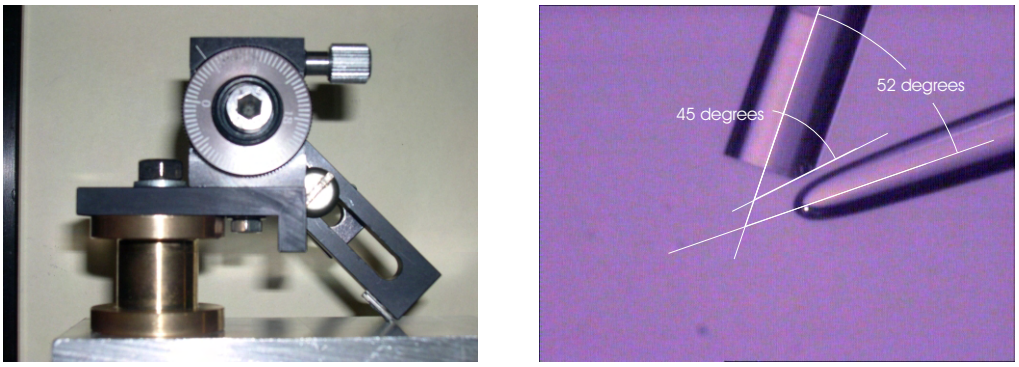

FIGURE 9.9: (a) angle polishing rig. (b) fibre geometry.

index matching fluid. This had a minimal effect on the collection signal. A second attempt at reducing this "self-scattered" light was tried by reducing the angle between the tapered lens and the collection fibre. Furthermore, a more acute angle between the fibres should give, on average, a better collection efficiency (see Appendix C). A more detailed picture of the shape and size of one of the lenses was drawn up and the possible mounting geometry was investigated, with consideration given to both the physical shape and focal length of the lenses.

Polishing the edge of the collection fibre down towards the core allowed a tighter angle between the fibres. This polishing was achieved by glueing the multimode fibre into a glass ferrule which was hand polished at a 45 ° angle (see Fig. 9.9(b)). The end of the TLF was aligned with the central axis of the collection fibre, and the collected light signal was measured as the TLF was withdrawn towards the edge of the fibre. The signal had fallen to 9/10 of its maximum value when positioned such that the focus point of the lens lay on the axis of the collection fibre, and dropped to zero as the end of the lens was aligned near to the edge of the fibre core. Although the change in the geometry precluded a direct comparison with the scattering, measured with the fibres at a greater angular separation, it was evident that this did not solve the problem.

9.3.2 Magnitude of "self-scattering" from TLF

To assess what problems this "self-scattering" may actually cause, it was necessary to gain an estimate of the magnitude of this unwanted signal. A power meter head was positioned a short distance away from the side of the TLF to measure the scattered component of the light, which was assumed to scatter in a spherically

symmetrical pattern. Taking into consideration the area of the detector, and its distance from the tip of the lensed fibre, the ratio of scattered power to power in the beam was found to range from $3{\times}10^{-4}$ to $1{\times}10^{-3}$ over several experiments.

In order to consider how this may affect a detection measurement we can consider a resonant beam with power of about 10^{-10} W, giving an intensity at the centre of the beam, at focus, equal to the saturation intensity of rubidium, $I_S = 1.6$ mW cm^{-2}. In this case, the probability of the atom being in an excited state is 1/4, leading to an average spontaneous emission rate of $\Gamma/2$. If 2% of these photons are collected by the detector, this leads to an atomic signal power of $\sim 2 \times 10^{-14}$ W. The total power scattered from the end of the lens will be 3×10^{-14} W to 1×10^{-13} W, of which about 9/10 $\times$2% will be collected. This indicates that the power collected directly from the lens is between 3% and 9% of the atomic signal, and may constitute a problem.

However, this simplistic model does not take into account atomic heating which will soon evict the atom from the collection region. In this case, a more realistic single frequency detection system could be used with a red detuning of several hundred linewidths, in order to produce a potential well for the atom. A compromise between atomic excitation and trapping could then produce a reasonable time window for a detection event. If this type of scheme is considered, then higher powers would be needed for a similar atomic signal, and the "self-scattering" could certainly prove to be a problem.

Through correspondence, the manufacturers suggested that this scattering could originate from dirt on the end of the TLF, and suggested thorough cleaning. This was carried out using acetone, ethanol, and distilled water, but no change was noted when viewing the scattering via camera and, furthermore, the same effect was seen from all of the tapered lenses with this specification. Quantification of this was not carried out, so it is unknown whether the range of "self-scattering" results could be partly due to additional scattering due to dirt or dust. Additionally, the company stated that their manufacturing process was constantly improving and that newer lenses would have better optical properties. Following this, a number of new TLFs were ordered but with a 50 µm working distance. This would allow for a greater range of mounting geometries, which would be beneficial when considering the placement of the fibres with respect to the guiding wires on the atom chip. Unfortunately these new lenses could not be tested as they were destroyed by the fire before they could be characterised.

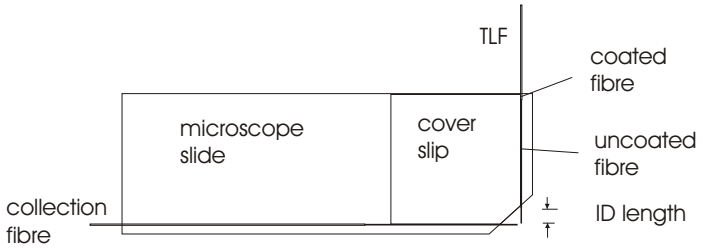

FIGURE 9.10: Initial trial mount

9.4 Tapered lensed fibres - fluorescent detection scheme mounting experiments

For a first attempt, the TLF and collection fibre were to be mounted orthogonally onto a microscope slide, using the edges of a microscope cover slip to guide the fibres (see Fig. 9.10). The removal of a corner of both the slide, and cover slip, produced an accessible free space gap for the atoms. Since the collection fibre and the TLF (not including the ID length discussed in Subsection 9.2.1) have similar diameters, this method should ensure that the central axes of both of the fibres lie in the same horizontal plane. The mounting was carried out using two three axis stages; one supporting the substrate, and the other used to position the fibre. A basic preliminary experiment was carried out using two pieces of plain 125 µm fibre and, although certain problems presented themselves, it was possible to manoeuvre a fibre into the correct position adjacent to the cover slip and flat to the slide, and then move it to a position 20 microns away from the central axis of the second fibre, approximately the working distance of the TLF, using piezo stage actuators. The second fibre (collection) could be positioned by monitoring through a microscope, and CCD camera, as the positional tolerance was not as strict: this needed to be within 100 µm to allow for maximum photon collection according to the simple model described at the beginning of the chapter.

The fine tuning of the fibre alignment was to be carried out actively, and a UV epoxy used to allow for this. It had been found that, since it had been possible to accurately find the focus of the TLF with a SNOM tip then, in free-space at least, the collection fibre could be positioned to collect as much of the light scattered from the tip as possible, which would place the central axis of the collection fibre within about a micron of the TLF focus in the horizontal or vertical direction. Although the alignment appeared possible, friction between the fibre along the length of the microscope slide caused some problems for fine tuning, and manipulating the fibres whilst keeping them against the length of the cover slip was a problem.

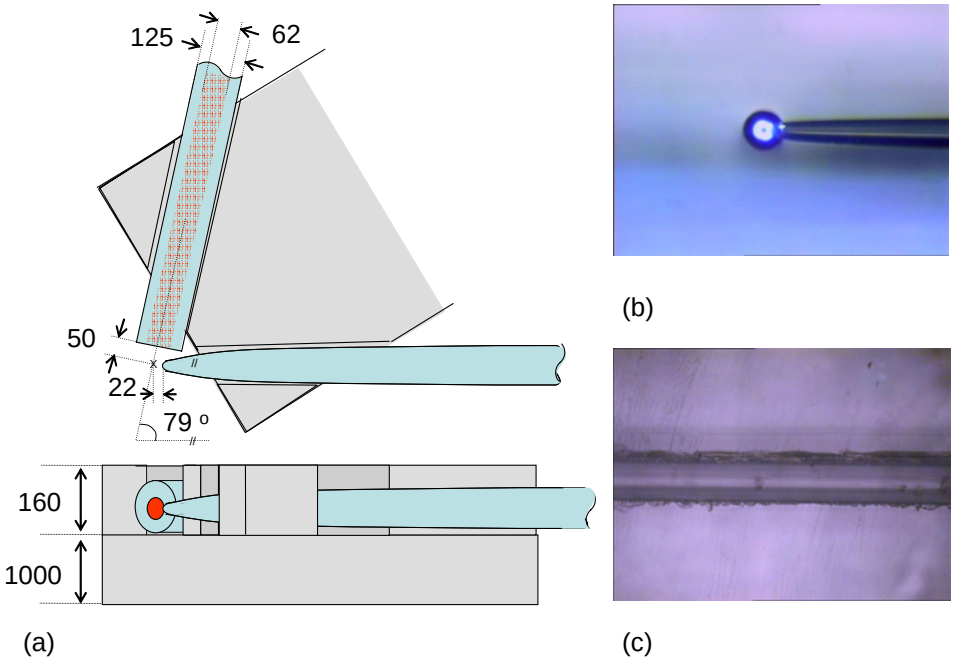

FIGURE 9.11: Schematic of prototype mount, dimensions in µm, (a); Collection fibre and tapered lens (light introduced into multimode fibre to enable core visualisation); Fibre channel, (c).

For these reasons the design of the test mount was changed. The cover slip was cut into three pieces and the edges were wet and dry polished in order to remove material, and to produce flat surfaces. After cleaning, these pieces were glued (Norland 800 UV) and aligned onto half a microscope slide as illustrated in Figure: 9.11(a). Note here that this schematic is not drawn to scale with the diameters of the fibres being largely exaggerated.

By pushing the pieces together against lengths of stripped standard 125 µm diameter fibre it was possible to produce channels approximately 125 µm wide to accommodate the lensed and collection fibres (Fig: 9.11(c)). With the fibres mounted on the substrate in this way there was less friction, so the fibres could be moved freely along the channels. The fibres were mounted in fibre chucks connected to stages allowing 6 degrees of freedom. The experimental set-up is shown in Figure 9.12. By optimising the collected signal scattered from a SNOM tip, introduced at the focus of the lensed fibre, and also by inspection of the monitoring camera images, the TLF and multimode fibres were positioned. The focus of the lens had been found by moving the SNOM tip and sampling an area 20 µm by 20 µm. This scan was repeated but this time the scattering signal into the collection fibre was recorded. By comparing the two images, the difference in SNOM position was

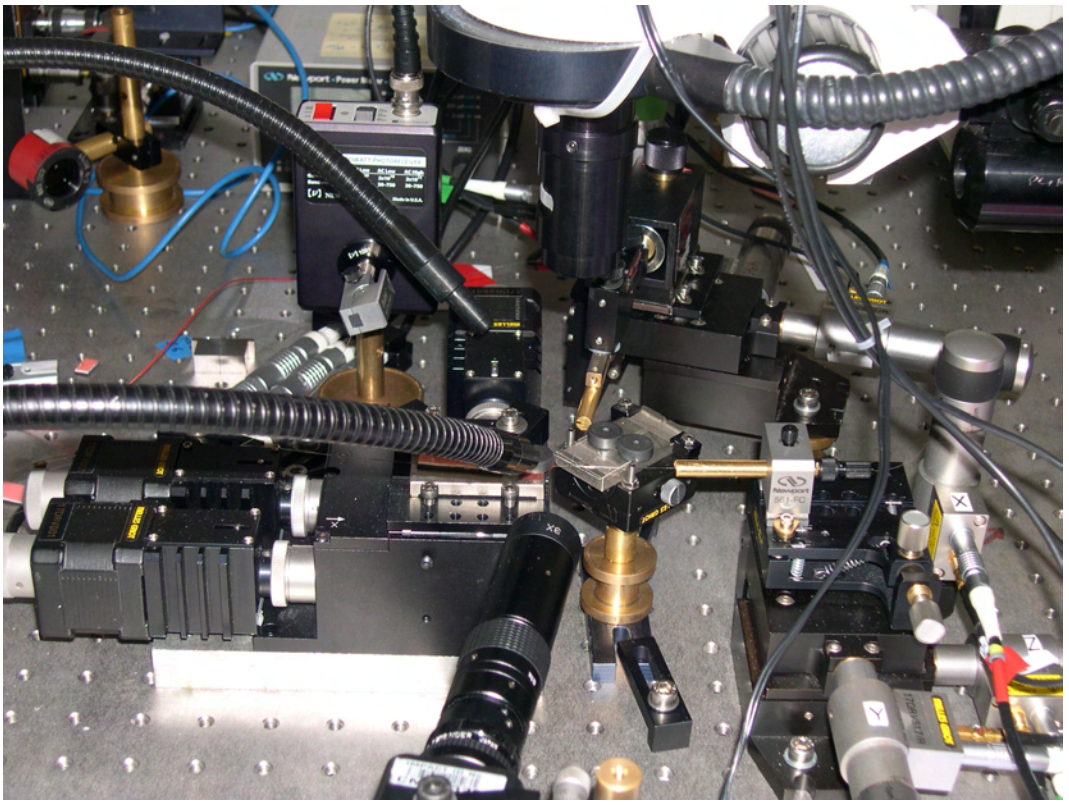

FIGURE 9.12: Equipment set-up for fluorescence detection scheme test mounting.

calculated for the maximum signal in each case. This displacement was found to be $\Delta x = 0.7 \pm 0.5$ µm and $\Delta y = 1.2 \pm 0.5$ µm, where the uncertainty has been taken from the resolution of the scan. Next the TLF was glued into position with UV glue. On application, the glue spread appreciably along the channel towards the protruding end of the lens, but did not appear to alter the emitted beam. The displacement of the focus from its original position, after glueing, was found to $\Delta x = 1.5 \pm 0.5$ µm and $\Delta y = 0.5 \pm 0.5$ µm. The SNOM tip was centred with respect to the new TLF axis and then the collection fibre was glued into place. Scanning the SNOM tip again and recording the collected signal resulted in a difference in maximum signal positions for the SNOM tip being reduced to $\Delta x = 0.3 \pm 0.5$ µm and $\Delta y = 0.8 \pm 0.5$ µm. The focal point of the TLF was estimated to be 55 µm away from the collection fibre, in a line along the collection fibre axis, and each fibre protruded 2 mm from the edge of the substrate. An image of the two fibres is displayed in Fig. 9.11(b). For visualization purposes white light is introduced into the collection fibre to show the position of the fibre core.

9.5 Conclusion

After moving to the new laboratory my work focused on the fibre cavities, as time constraints ruled out setting up experiments for both the cavities and for investigating the fluorescence scheme, so unfortunately no more experimental work was carried out in this direction. It is interesting to note though that there is still an interest in a miniaturised fluorescence detection scheme within the cold atom community.

Marco Wilzbach et al. worked on a similar scheme in Heidelberg, and have had success detecting atoms with a 40 µm focus TLF and multimode fibre (NA =0.275) mounted at 90° from each other. Recently they have published results showing a detector efficiency of 56 % with an SNR of 275 [127]. By improving their photon counter, and using two high NA collection fibres, they expect to distinguish between one or two atoms with a detection probability greater than 99.9 %. They have also published theory concerning the use of off-resonant light to trap the atom [105]. Furthermore, the group's work on alignment structures using a hard epoxy based photoresist (SU-8)[29] has shown that these structures can be used to mount such a detection scheme, since it requires no active alignment.

As an alternative method for the mounting of tapered lensed fibres, the atom chip group at Imperial College have shown that it is possible to etch tapered grooves in silicon[28]. In the same paper the group suggest a single TLF fluorescence detector using both red detuned light to trap the atom, in addition to resonant light. The atomic fluorescence is to be collected by the same lens. They expect the scheme to be capable of detecting several tens of atoms.

The atom chip group at the Max-Planck Institute for Quantum Optics recently published a paper following their investigation of a dual frequency fibre based detector [73]. Their scheme involved the use of an aspheric lens and a single mode fibre, used to both transport a detuned 830 nm dipole trapping beam, as well as carry the resonant fluorescence from the atom. However, the atomic excitation in this case is provided by two slightly detuned counter-propagating beams originating away from the chip.

Chapter 10

Future Work and Conclusions

This chapter provides a summary of the work presented in this thesis along with the conclusions reached. Various methods for improvement of the fibre devices are then offered, in addition to a selection of possible research directions which would aid the development of single atom detection on an atom chip.

10.1 Summary and thesis conclusion

The massive progress in the field of cold atom research and quantum control has been accelerated by the development of the atom chip. By reducing the size of the elements needed to manipulate atomic states, and atomic position, high levels of control have been reached, and the possibility of scalable quantum information processing is a step closer. Furthermore, this miniaturisation of quantum and atom optic experimentation has allowed for a deeper understanding of fundamental physics, such as atom surface interactions, and offers technological advancement in the fields of frequency standards and sensing. However, the inclusion of micro-optical devices is still a necessity for a fully integrated chip based atomic laboratory.

This thesis has detailed our progress towards the integration of micro-optical fibre components onto the atom chip. The investigation and construction of fibre devices aimed at single atom detection has been described, starting from initial trials with cavities formed with evaporated gold coated mirrors, or dielectric films, and resulting in the successful mounting of fibre gap cavities onto silicon v-grooves. In another direction, the idea of using a tapered fibre lens and a multimode collection

fibre for a fluorescence detection device was examined.

After showing that Bragg grating technology is a viable technology for fibre cavities by working at the wavelength of 1550 nm, where the the fibre optic field is more mature, the work advanced to devices designed for 780 nm light, the wavelength required to interrogate the D2 line in rubidium. Here the issue of grating loss was uncovered and the effect this would have on a detection device analysed. Characterisation procedures were developed to measure these losses and a full theoretical understanding of fibre cavities was researched.

Similar losses had been reported in the literature and a solution related to these results was found. Thermal annealing experiments on both single gratings and fibre cavities showed that not only could these losses be reduced, but also the strength of the cavity gratings could be tuned, in order to optimise device characteristics, without altering the wavelength. Consideration to the manufacturer's original stabilisation annealing procedure and the requirements for ultra-high vacuum experimentation was given.

The practical reality of introducing a gap into the fibre cavities was detailed, with comparison made to the theoretical maximum coupling between the fibre arms. Furthermore, the mounting methods and schemes were described, and the complex phenomena arising from coupled cavities was illustrated. Due to the limited size of the bandgaps of the Bragg gratings, tuning of the gratings to the required wavelength is required, and preliminary work on this aspect was also described.

The conclusion gained from the work described in this thesis is that the use of fibre optics offers a good solution to the integration of optics on an atom chip. Considering the figures quoted for the mounted gap cavity in Section: 8.5.1, and using the theory of Horak et al.[92] introduced in Chapter: 2, we find that this cavity would offer a possible SNR of 10, working on resonance, or $\mathrm{SNR}_{\mathrm{hom}} = 7$ with a detuning of 50 Γ, with the spontaneous scattering $M \approx 90$ photons in a 10 µs time window, for both cases. This is comparable with the example given in the detection theory section, but includes a measured grating loss of 0.7 %. Since it was shown in Chapter: 6 that these grating losses can be reduced, then further improvement can be expected and fibre optics can surely be used for single atom detection.

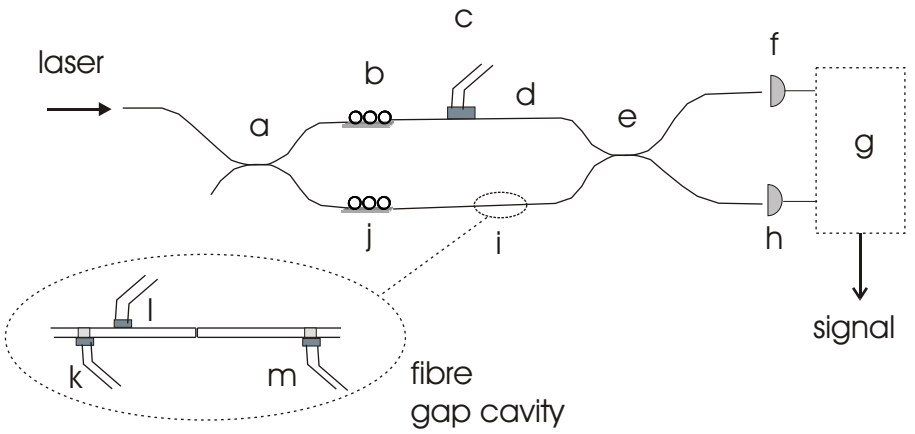

FIGURE 10.1: Conceptual schematic for homodyne fibre cavity atom detection. Laser light is directed into a reference arm (d) of the interferometer with a portion of this light split via a fibre coupler (a) and directed towards the atom chip mounted fibre cavity (i). A piezoelectric stretcher (c) is used to maintain the interferometer at a fixed operating point. A single cavity polarisation eigenmmode is obtained by altering the input polarisation via the polarisation controller (j), whilst the output polarisations of the two interferometer arms are matched using a polarisation controller (b) in the reference arm. The light is mixed at a 50-50 coupler (e), and the light from each exit port is measured using the photodetectors (f) and (h). Signal processing (g) provides the detection signal and/or feedback for an active interferometer. Three piezoelectric stretching elements are attached to the mounted cavity, two for tuning the gratings (k),(m), and one to tune the length of the cavity (l).

10.2 Future work

This section offers possible future research directions for continuing the implementation and improvement of fibre devices for the atom chip. There is scope for a large amount of experiment and investigation, not only for atom detection devices, but also if one wanted to use the cavities for other purposes such as cooling or quantum logic operations. In this case, ways around the intrinsic gap loss need to be found.

10.2.1 Atom detection prospects - device implementation

Once mounted on an atom chip, the cavity is to form one arm of an interferometer in a homodyne scheme which is illustrated diagrammatically in Figure: 10.1. Laser light is to be divided between the cavity and a reference arm and the light then recombined with a 50-50 fibre coupler. The laser is to be locked to a wavelength,

detuned from the rubidium D2 line, and the cavity is to be locked to the laser by mediating the cavity length with a piezoelectric device. The details of this locking, and the methods decided upon, are subject to investigation which is described further in the following subsection.

The input polarisation to the cavity is controlled using a polarisation controller to ensure that only one cavity eigenstate is matched. A further polarisation controller on the reference arm is to be used to match the output polarisations of the fibre arms to ensure maximum interference. In order to maintain the interferometer at a fixed operating point, the length of the reference arm is to be controlled using a further piezoelectric stretcher. If possible this will be actively controlled via feedback but, similar to the cavity length stabilisation issue mentioned in the next subsection, this will need to be isolated from any atom detection event.

The atom detection signal is to be processed from the photocurrents generated in the photodetectors connected to the exit ports of the second 50-50 coupler. These same photocurrents would be used if the interferometer was to be actively maintained at the quadrature point (provided that this is isolated from phase shifts caused by the presence of an atom in the cavity). In order to maximise the cavity finesse, if necessary, the Bragg grating reflectors are to be tuned to the working wavelength using two additional piezoelectric stretchers, however active control should not be necessary in this case.

There is good reason to believe that single atom detection on an atom chip will be possible, provided that the complete device is limited mainly by the photon noise inherent in the cavity detection, rather than additional noise introduced by the signal detection system. With careful design, and choice of optoelectronic components, this should be the case. Furthermore, it has been shown in this thesis that there is no material limitation due to the fibre Bragg cavities themselves.

10.2.2 Experimental requirements

The mounting experiments discussed in Chapter: 8 need to be extended. With the use of longer v-grooves the methods developed in my PhD work should provide for more accurate aligment. The opportunity to mount on an actual atom chip with mounted grooves, or grooves etched into the surface of the chip, would be desirable. Unfortunately silicon etching work by one of our group, Dr. Corbari, was curtailed by the fire soon after it had begun. This was unfortunate as mounting with larger grooves would have been beneficial. However, although I have no first

hand experience with the structures, the SU-8 photo-resist structures [29] used by the Heidelberg atom chip group (now University of Vienna) would appear to offer a good solution.

The tuning experiments referred to in Section: 8.7 need to be extended, and a completely tunable and lockable system needs to be devised. As discussed, piezo tuning of the gratings is a viable method and this could also be used on one of the cavity arms to tune the cavity as a whole. Since the extension necessary to keep the cavity in resonance will probably be much smaller than the extension needed to tune the gratings to the laser frequency (1 FSR compared to at least several FSR), then it may be possible to use only two tuning elements, allowing each grating piezo to extend past the grating and stretch the cavity also. The cavity tuning will then only alter the grating reflectivity slightly. This would need to be calculated theoretically and experimentally confirmed. Another alternative method for grating tuning is heat, via thin film heating or something similar, however whether the wavelength change would be fast enough would need to be confirmed.

The cavity locking needs investigating also. For the dual wavelength locking commonly used in conventional QED experiments with macroscopic mirrors (eg. [62]), the cavity is stabilised using an auxiliary laser, which is itself locked to a reference cavity. This wavelength used is several longitudinal-mode orders away from the cavity QED mode, producing a small effect on the atom. Investigation into implementing this in fibre is desirable. There is no problem for propagating two single modes with a relatively large wavelength separation in fibre, with consideration only needing to be given to the geometry and cut-off wavelength of the chosen fibre. Fibre Bragg gratings have been shown to be desirable for fibre cavities so the question is whether a second set of Bragg gratings at the required wavelength could be implemented without introducing further losses. Research, both theoretical and experimental, would confirm whether this would be viable, considering both the effect on the atom (dipole forces, Stark shift, etc.), and the optical implementation needed with its additional complexity and tuning issues. Alternatively, the cavity locking can be carried out using the detection laser between detection events, and this would require consideration of the necessary timing.

Work is also needed on the signal detection side. In the case of the actual detection of photons, avalanche photon detectors with extremely high quantum efficiency are commercially available, but in order to use a homodyne detection scheme in fibre, several problems need to be overcome, and a viable system needs to

be developed. Two beam interferometric devices in fibre (e.g. Mach-Zehnder or Michelson) tend to suffer from polarisation-induced fading due to the differing evolution between the states of polarisation in the two fibre arms. Investigating the extent of this problem with respect to an integrated atom chip device is necessary from both a theoretical and an experimental point of view. Several solutions to this problem in sensors have been put forward, such as feedback controlled input polarisation offered by Kersey et al.[128]. However, since we already have a single arm interferometer (FFP), the input polarisation needs to be set in order that only a single resonant mode is present in the cavity, and an alternative solution is required.

10.2.3 Device improvement

In order to improve the efficiency of a fibre cavity atom detection device for the atom chip there are several directions that may be investigated and problems to be solved. Consideration must be given to the question of whether the device is to be used plainly as an atom counter, or whether it is possible to produce a device for reversible quantum logic operations or "interaction free" measurement.

The polarisation of the light in the gap needs to be investigated and possibly controlled. The theory reported in this thesis considers a two state atom only and does not take into account the magnetic sub-levels of the atom. Atoms are now commonly guided within potential minima of magnetic fields, for example from two wire guides. These weak-field seeking atoms have a magnetic moment that is anti-parallel with the field. A bias field is added in order to remove a zero potential which would allow uncontrolled atomic spin flips. However, if the atom is pumped into a strong-field seeking state it will be immediately ejected from the guide. If atoms are to be detected whilst being magnetically guided, rather than with the guiding fields off, then the state of polarisation may need to be controlled. It is possible that selecting the opposite orthogonal resonant polarisation in the cavity may be all that is needed, but this needs to be explored. The use of highly birefringent polarisation preserving fibre may be necessary.

Optimisation of the fibre geometry is another consideration for the gap cavity detection scheme. The fibre used for the work described in this thesis is "off-the-shelf", and chosen only for the fact that it is single mode at the required wavelength of 780 nm, and for its photosensitive properties, to allow the writing of Bragg gratings. The atom-cavity coupling is inversely proportional to the cross-

section of the cavity mode at the position of the atom, so it would seem to be beneficial to reduce this as much as possible. However, the mode size is governed by the choice of fibre (which needs to be single mode at 780nm) and, perhaps more importantly, the smaller the mode size the greater the divergence of the beams within the cavity and hence diffraction losses. If the gap size is small compared to the Rayleigh range of the beam within the gap ($d \ll z_0$) then, intuitively, the diffraction can be said to be small. By analysing the effect that changing the core size and NA of the fibre, and the gap size, have on the detector efficiency, whilst taking into account the parameters necessary for single mode guiding, and also taking into consideration any increased susceptibility to bend loss, it should be possible to design a fibre which would be more suitable than the present fibre.

Associated with the above research into fibre geometry would be the concept of using an anti-reflection coating on the fibre faces. The Fresnel reflections from the fibre faces are generally unwanted, because the field amplitude in the gap and the subsequent gap loss are both dependent on the destructive or constructive interference between these reflections. At first glance the idea of anti-reflection coatings seems a good one, as the cavity dynamics would simplify considerably from three coupled cavities to a single lossy Fabry-Perot. However, although multilayer films on both faces are thin, summing to only a few quarter-wavelengths in total, the additional loss of a micron or so from the gap may not be acceptable, since the light is not guided within these layers. However, when taken into consideration along with the fibre geometry, and any possible gap expansion, they may form part of a more optimal solution. Perhaps a single layer, reducing the reflection down to 1 % or so, would offer an acceptable improvement.

In order to increase the size of the gap, or to enter a stronger coupling regime, which could offer interaction free measurement, the use of some kind of focusing element on the fibre faces would be needed. This is another direction in which future work may be directed. The use of graded index lenses, or other structures attached to the fibre faces, needs to be investigated. The fabrication of diffractive optical elements on fibre using e-beam lithography and chemical etching [129] has been published, and a thorough analysis of concepts such as this should be considered, for their suitability of use on the atom chip.

10.2.4 Other directions

The idea and application of evanescent detectors such as microdiscs or microspheres for atom detection was discussed at the beginning of this thesis with references to the literature. However, the concept of using the evanescent field emanating from the surface of a planar device needs researching. One obvious vehicle for a fully integrated system would be planar waveguides written into the substrate/chip itself. A bridging experiment to test the feasibility of this could be based upon a closed fibre cavity. By polishing a section of the fibre down to the core, it would be possible to couple the atom to the evanescent field of the cavity. This would have the benefit of low loss within the cavity, due to the omission of the gap, although the atom cavity coupling would be small.

Appendix A

Detector Response Adjustment

The following are corrections for detector response using the model described in Subsection: 7.2.1 with a detection broadening time, $t_{\text{det}} = 1.6 \times 10^{-4}$ s.

			Measured		Calculated	
No.	Z (mm)	WF (J cm^{-2})	F	τ (%)	L ($\times 10^{-3}$)	T (dB)
1a	2	800	82.3 (73.5)	68 (60)	6.5 (9.3)	−15.2 (−14.9)
1b *	2	800	73.2 (65.5)	71 (64)	6.5 (9.6)	−14.5 (−14.3)
1c	2	800	83.4 (73.6)	68 (60)	6.5 (9.4)	−15.2 (−14.9)
2a	5	150	39.0 (36.7)	62 (58)	16.7 (19.8)	−12.2 (−12.0)
2b	5	150	52.0 (48.0)	53 (49)	15.9 (19.2)	−13.7 (−13.5)
3a	4	400	197.2 (149.9)	8.7 (6.5)	11.2 (15.5)	−23.4 (−22.8)
3b	4	400	209.0 (156.6)	3.5 (2.6)	12.1 (16.7)	−25.6 (−25.0)
3c	4	400	207.5 (155.8)	4.5 (3.4)	11.8 (16.3)	−25.0 (−24.4)
4a	5	185	40.1 (37.7)	61 (56)	17.0 (19.9)	−12.3 (−12.2)
4b	5	185	69.1 (62.2)	37 (33)	17.5 (21.3)	−15.7 (−15.5)
4c	5	185	55.9 (51.3)	46 (42)	17.7 (21.1)	−14.3 (−14.2)
* grating mismatch						

TABLE A.1: Corrections for measurements and calculations from first set of test cavities written in PS750 fibre (Table 5.1). Grating length, Z; writing Fluence, WF; maximum cavity finesse, F; cavity throughput on resonance, τ; calculated grating loss, L; and calculated grating transmission, T. Original measured values and calculations are in brackets for comparison purposes.

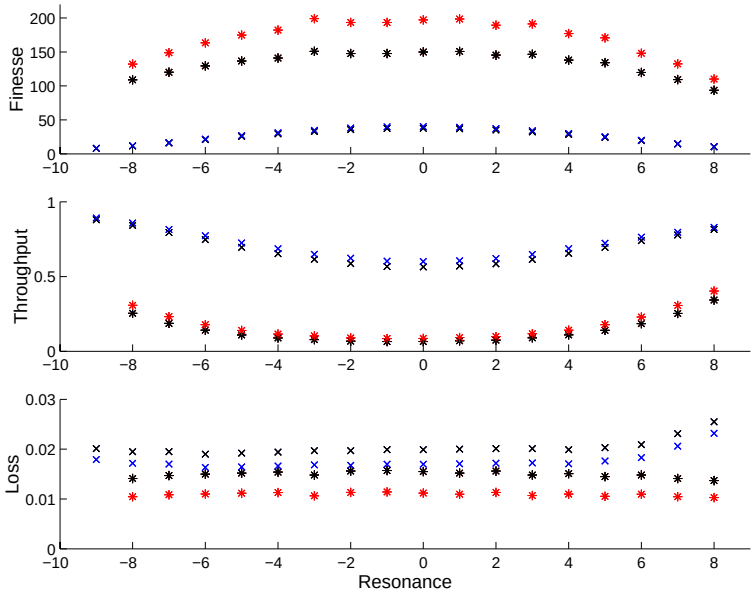

FIGURE A.1: Corrected cavity finesse, F, corrected throughput, τ, and calculated loss, L, for cavities 3a (red stars) and 4a (blue crosses). Original measurements and calculated loss displayed as black stars and crosses, respectively, for comparison purposes (see Fig. 5.6).

	Cavity measurement		Single-grating measurement
Cavity no.	κ (m $^{-1}$)	α (m^{-1})	κ (m^{-1})
1a	1213 (1198)	4.0 (5.7)	1200 ± 23
1b	1175 (1163)	3.9 (5.7)	
1c	1214 (1198)	4.0 (5.7)	
2a	414 (410)	3.6 (4.2)	407 ± 5
2b	450 (445)	3.7 (4.4)	
3a	844 (826)	4.7 (6.4)	840 ± 6
3b	907 (891)	5.5 (7.4)	
3c	890 (873)	5.3 (7.1)	
4a	418 (415)	3.7 (4.2)	424 ± 14
4b	497 (492)	4.4 (5.3)	
4c	465 (461)	4.2 (5.0)	

TABLE A.2: Corrected coupling and loss coefficients for first cavity set in PS750, from cavity measurements, and from single grating measurements. Computed values from initial measurements included in brackets. Transmission measurements are an average of each pair (see Table: 5.2).

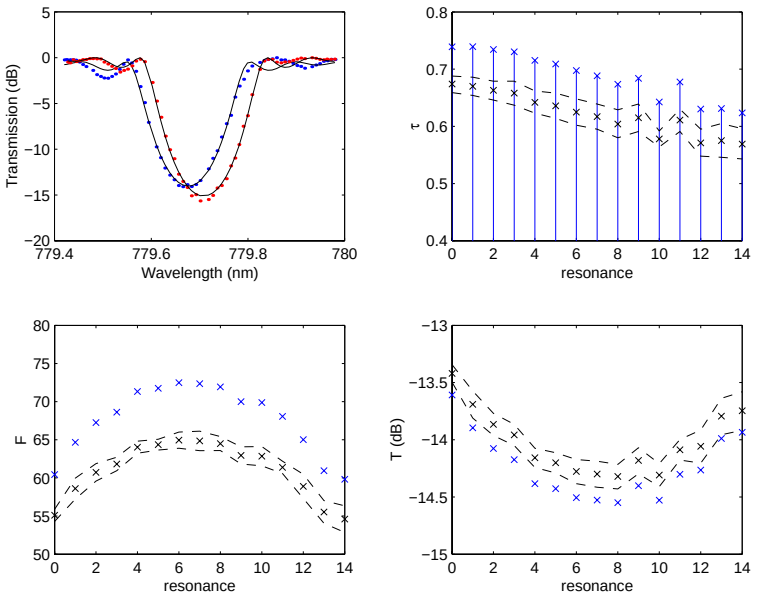

FIGURE A.2: Fig. 5.8 correction. Grating transmission measurements for cavity 1b and corrections to LabView data for measurements around region of maximum finesse: cavity throughput, τ, finesse, F, and calculated grating transmission, T. Black crosses are uncorrected with dashed lines indicating the limits of one standard deviation.

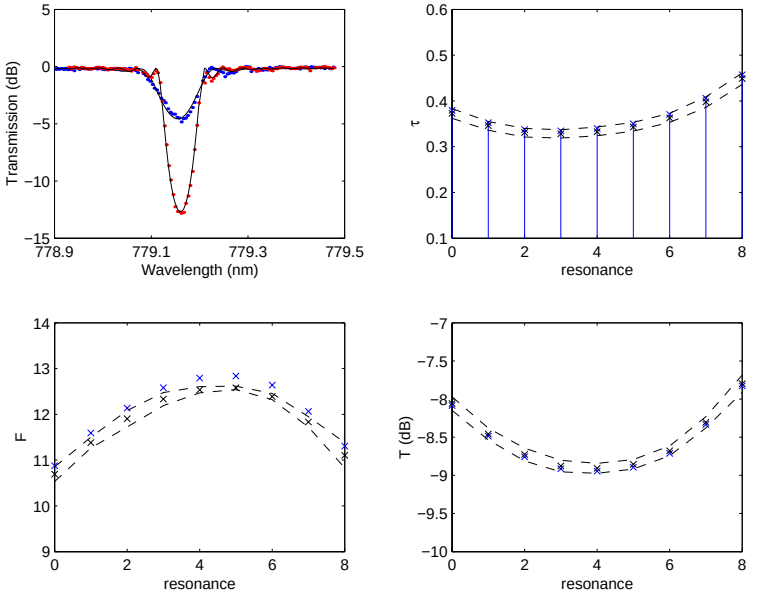

FIGURE A.3: Fig. 5.9 correction. Grating transmission measurements for Cavity 2c and corrections to LabView data for measurements around region of maximum finesse: cavity throughput, τ, finesse, F, and calculated grating transmission, T. Black crosses are uncorrected with dashed lines indicating the limits of one standard deviation.

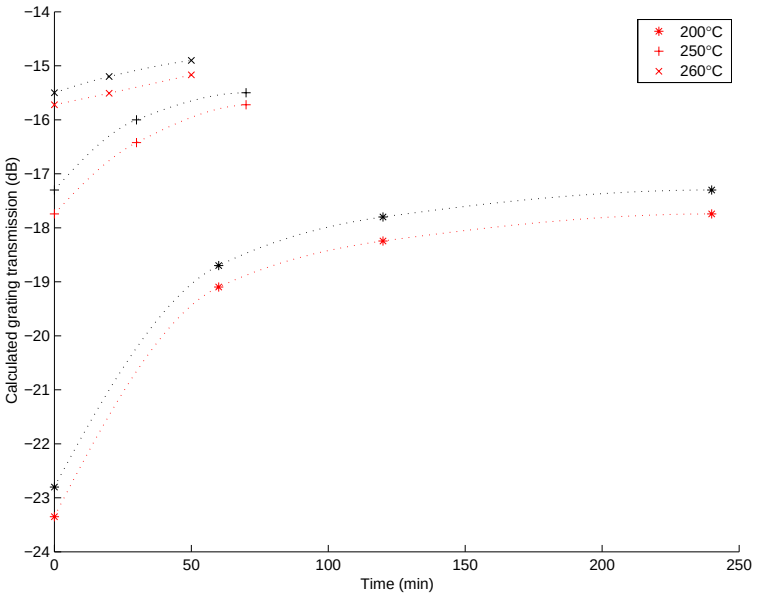

FIGURE A.4: Fig. 6.3 correction. Corrected minimum transmission,T, for cavity 3a annealing experiment (red). Original calculations in black. Dashed lines are guides for eye only.

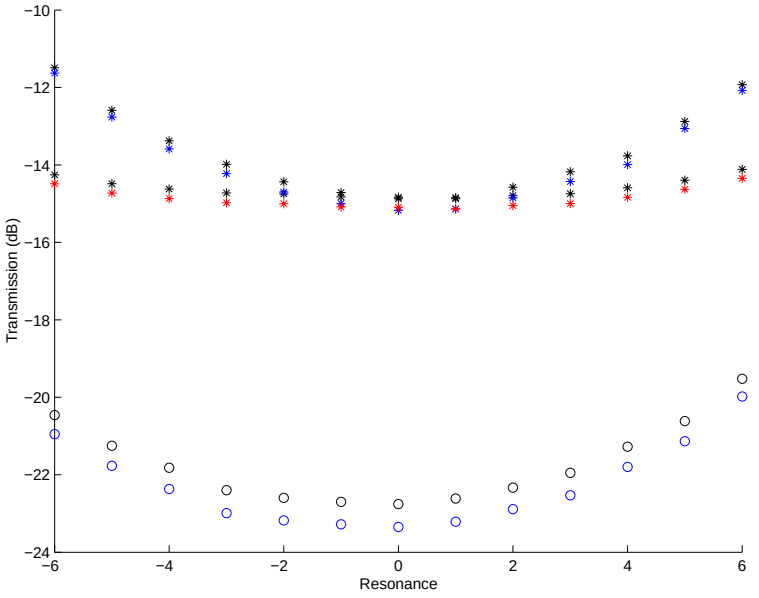

FIGURE A.5: Fig. 6.4(a) correction. Transmission comparison of annealed cavity 3a and cavity 1a. (a) Calculated grating transmission: 1a red stars, 3a blue stars , 3a pre-anneal transmission, circles. Original calculations shown with black symbols.

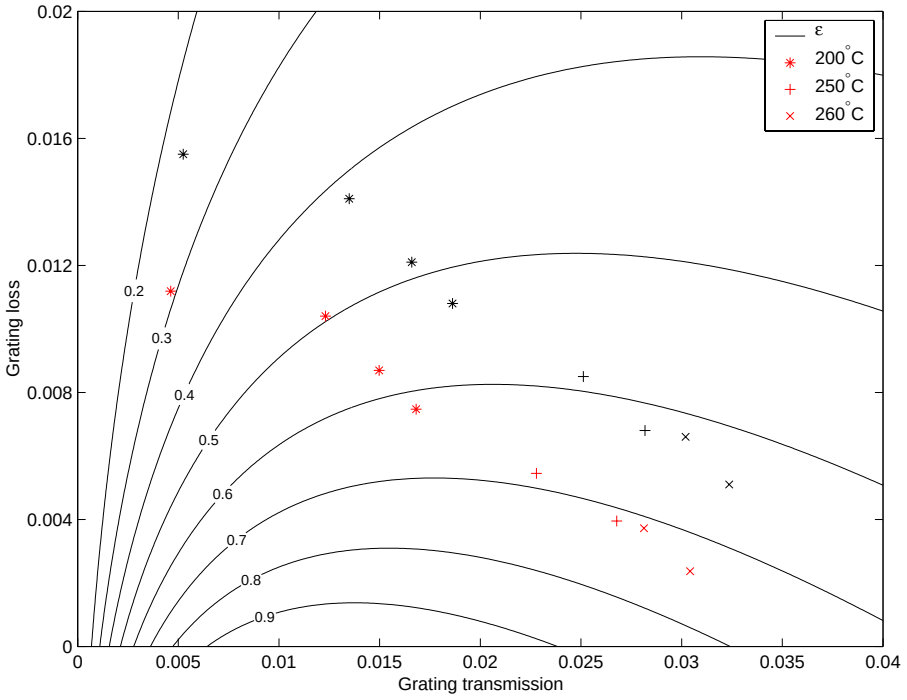

FIGURE A.6: Fig. 6.5 correction. Corrected results of thermal annealing of cavity 3a. Corrected calculated grating loss, L, and transmission, T (red symbols) against ϵ (contours). Original calculations black symbols.

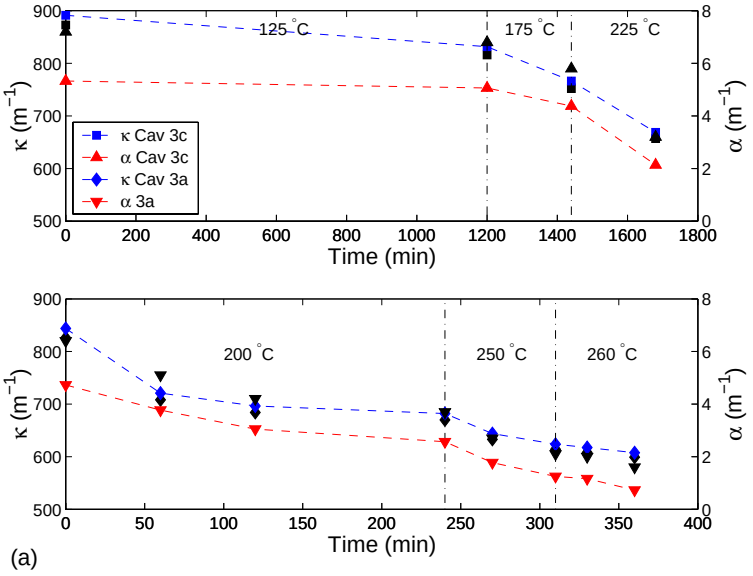

FIGURE A.7: Correction to Fig. 6.6(a). Comparison of low and high temperature annealing. The trends in grating loss per unit length and coupling constant against time are compared for low temperature annealing of cavity 3c, top, and high temperature annealing of cavity 3a, bottom. Original indicated with black symbols.

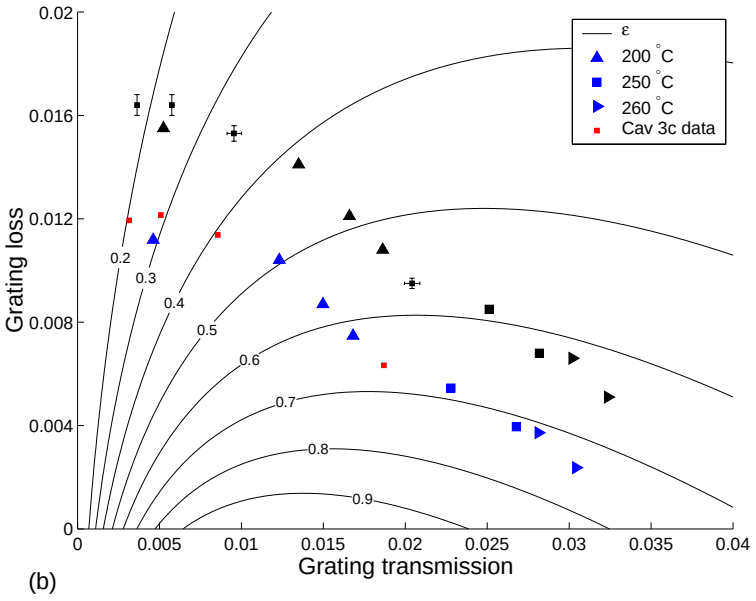

FIGURE A.8: Correction to Fig. 6.6(b). Comparison of low and high temperature annealing. Plots the grating loss against transmission for the annealed cavities 3a and 3c with reference to the cavity figure of merit ϵ. Uncorrected data indicated with black symbols.

Appendix B

Rubidium

There are many reasons why the cooling of alkali-metal atoms has become popular in recent years:
(i) the ground states have a closed shell with one valence electron;
(ii) it is easy to generate the light required for optical transitions, achievable with inexpensive diode lasers;
(iii) an atomic beam can be produced in a simple manner since only a relatively low temperature is required for a high vapour pressure.

Rubidium is an alkali-metal with ground state configuration:

$$1s^2 2s^2 2p^6 3s^2 3p^6 3d^{10} 4s^2 4p^6 5s^2 S_{1/2}$$

or [Kr]$5s^1$. There is no net angular momentum or spin for the closed sub-shell but it plays a part in the l-dependence of the energy levels of the valence electron. In effect, different orbits see different nuclear charges because of different levels of core penetration. Rubidium has two stable isotopes, ^{85}Rb and ^{87}Rb with respective abundances 72.17% and 27.83%. They have different nuclear spin and therefore different hyperfine structures which are shown in Figure B.1. The different transitions between F-levels which make up the D1-transitions and D2-transitions are also indicated.

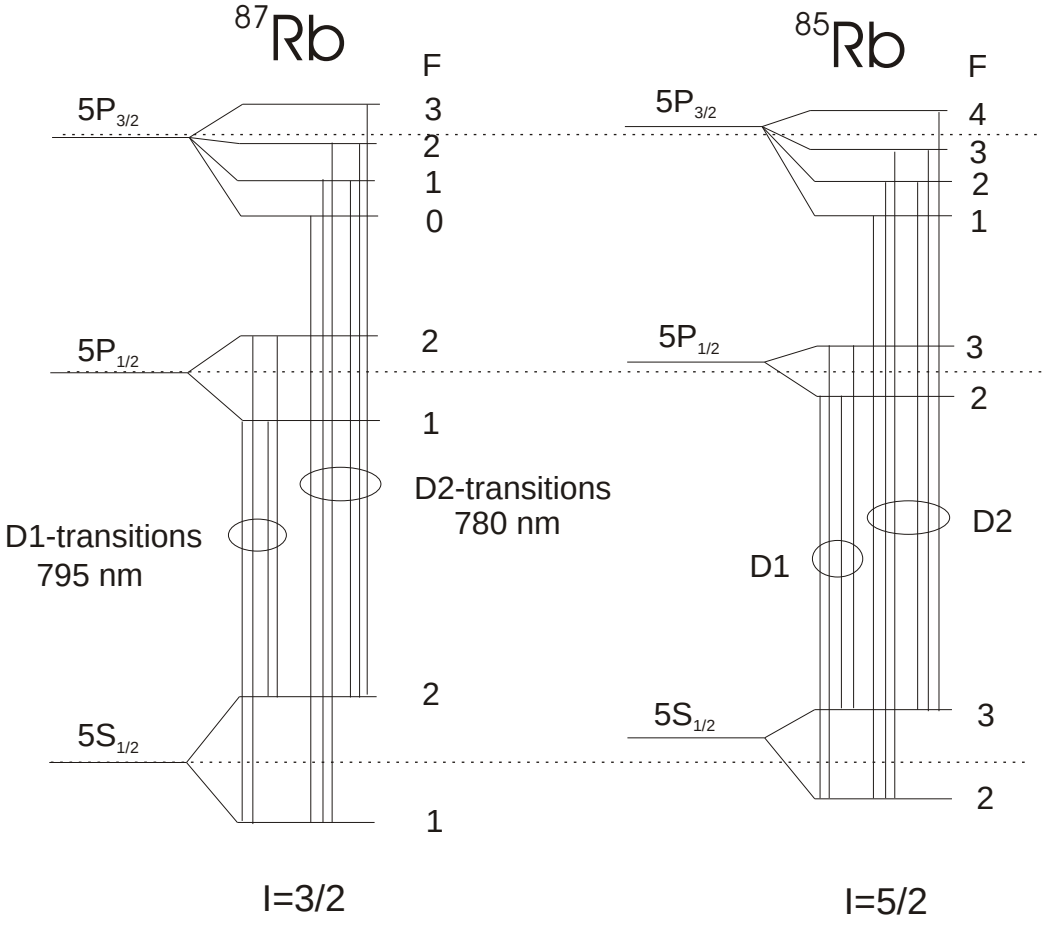

FIGURE B.1: Energy levels of Rubidium isotopes

Appendix C

Fluorescence - classical randomly oriented dipole

If we assume that the polarization direction of the illuminated light lies randomly in a plane perpendicular to the fibre lens then we can consider the atom to emit in a dipole pattern with the dipole axis being oriented randomly in this plane (the yz-plane in Figure C.1).

Firstly, considering a static dipole lying along the z-axis, as shown in Figure C.1(a), with the pump laser directed in the negative x-direction (into page). The electric and magnetic fields can be written [130], to the first order in 1/r, as

$$E_\theta = -\frac{\omega^2 p_0 \sin\theta}{4\pi\epsilon_0 c^2}\,\frac{\sin\omega(t-r/c)}{r}$$

and

$$B_\phi = -\frac{\mu_0\omega^2 p_0 \sin\theta}{4\pi c}\,\frac{\sin\omega(t-r/c)}{r}$$

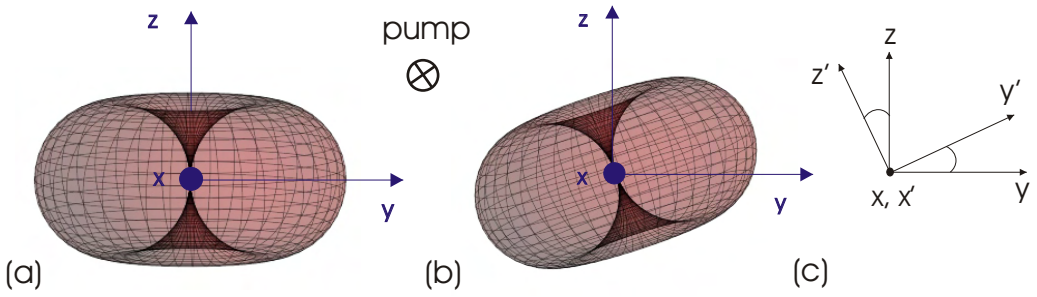

FIGURE C.1: (a) Dipole oriented along z-axis, (b)randomly oriented dipole in yz-plane, (c) coordinate transform

with

$$E_r = E_\phi = B_r = B_\theta = 0$$

where p_0 is the magnitude of the dipole, ω the angular frequency of the emitted radiation and, μ_0, ϵ_0 the permeability and permittivity of free space respectively. The far field radiation can be visualized as a toroidal pattern with a maximum energy flow in the xy-plane and zero energy flow in the positive or negative z-direction. This energy flow is in a radial direction and is given by the Poynting vector

$$\mathbf{N} = \mathbf{E} \times \mathbf{H} = \mathbf{e}_r \; E_\theta B_\phi/\mu_0 = \mathbf{e}_r \frac{\omega^4 p_0^2 \; \sin^2\theta}{16\pi^2\epsilon_0 c^3} \; \frac{\sin^2\omega(t - r/c)}{r^2} \; ,$$

so that the instantaneous total power crossing a sphere of radius r centred about the atom is

$$W = \int_S \mathbf{N} \cdot d\mathbf{S} = \frac{\omega^4 p_0^2}{16\pi^2\epsilon_0 c^3} \int_0^{2\pi} d\phi \int_0^{\pi} d\theta \; \sin^3\theta \; \sin^2\omega(t - r/c) \; .$$

The time averaged power crossing the sphere can be found by integrating with respect to time over a cycle of the radiation, resulting in:

$$\overline{W} = \frac{\omega^4 p_0^2}{12\pi\epsilon_0 c^3} \; . \tag{C.1}$$

We can treat the random orientation of the dipole in the yz-plane by rotating the y and z axes through α (Figure C.1(c)) and averaging over a complete rotation.

$$\langle N \rangle = \frac{\omega^4 p_0^2}{16\pi^2\epsilon_0 c^3} \frac{\sin^2\omega(t - r/c)}{r^2} \frac{1}{2\pi} \int_0^{2\pi} d\alpha \; \left(1 - \left(\frac{-y\sin\alpha + z\cos\alpha}{r}\right)^2\right)$$

which gives an averaged Poynting vector

$$\langle \mathbf{N} \rangle = \mathbf{e_r} \; \frac{\omega^4 p_0^2}{32\pi^2\epsilon_0 c^3} \left(\frac{1 + \sin^2\theta\cos^2\phi}{r^2}\right) \sin^2\omega(t - r/c) \; . \tag{C.2}$$

The averaged Poynting vector is symmetrical about the beam axis (x-axis) so the power collected by a fibre lying in the y-direction is equivalent to the power radiated into a solid angle subtended by the core of a fibre pointing in the positive or negative z-direction. Transforming the coordinates by a further rotation, α_1, about the y-axis enables the calculation of the power emitted into any solid angle. Here we let α_1 represent the angle of the collection fibre from the perpendicular (see Figure C.2(a)). Accounting for the time dependence, we can rewrite Equation C.2

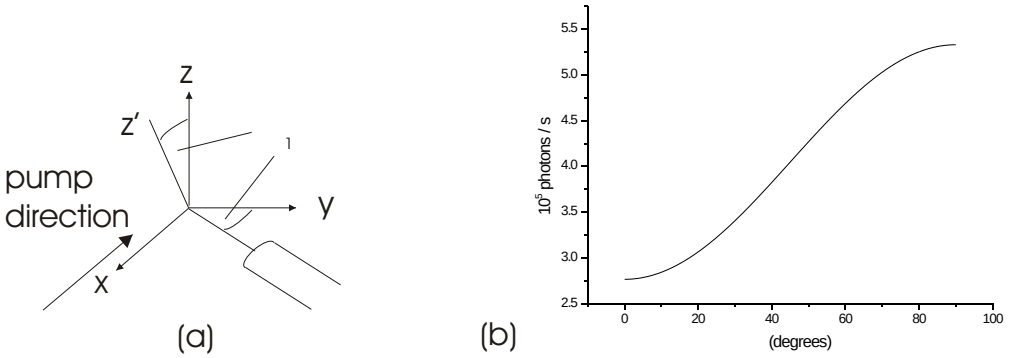

FIGURE C.2: (a) coordinate transform, (b) number of photons collected per second against position of collection fibre

as

$$\langle \overline{\mathbf{N}} \rangle = \mathbf{e_r} \, \frac{\omega^4 p_0^2}{64\pi^2 \epsilon_0 c^3} \frac{1}{r^2} \left(1 + \left(\frac{x}{r} \right)^2 \right)$$

and make the transformation: $x \mapsto x \cos\alpha_1 + z \sin\alpha_1$. Letting β be half of the angle subtended by the collection fibre core, then the time averaged power entering the collection fibre is

$$\langle \overline{W}_{fibre} \rangle = \frac{\omega^4 p_0^2}{64\pi^2 \epsilon_0 c^3} \int_0^{2\pi} d\phi \int_0^{\beta} d\theta \, (\sin\theta + \sin^3\theta \cos^2\phi \cos^2\alpha_1 + \sin\theta \cos^2\theta \sin^2\alpha_1 + 2\sin^2\theta \cos\theta \cos\phi \cos\alpha_1 \sin\alpha_1) \, .$$

Dividing the solution by Equation C.1 then gives the fraction of power entering the fibre:

$$\frac{\langle \overline{W}_{fibre} \rangle}{\overline{W}} = \frac{1}{2} + \frac{3}{16} \cos^2\alpha_1 \Big(\cos^3\beta - \cos\beta \Big) - \frac{3}{8} \Big(\cos\beta + \frac{1}{3} \cos^3\beta \Big) \, .$$

Figure C.2(b) shows the number of photons collected, at saturation, against the angle α_1 for a multimode fibre with NA= 0.275.

Due to symmetry, the same relationship applies for $-\alpha_1$ so the collection fibre could be positioned away from the TLF, however the highly divergent beam from the lens would have to be avoided.

List of Publications

S. Helsby, C. Corbari, M. Ibsen, P. Horak and P. G. Kazansky,
Fiber Bragg gratings for atom chips.
Physical Review A, Vol. 75: 013618, 2007.

M. Rosenblit, P. Horak, S. Helsby and R. Folman,
Single-atom detection using whispering gallery modes of microdisk resonators.
Physical Review A, Vol. 70(5): 053808, 2004.

S. Helsby, P. Horak and P. G. Kazansky,
Fibre optics for atom detection.
CLEO/Europe - EQEC, Munich 12-17 June 2005.

S. Helsby, H. F. Powell, P. Horak, B. G. Klappauf and P. G. Kazansky,
Fiber optics for quantum computing.
POWAG 2004, Bath 12-16 July 2004.

Bibliography

[1] D. J. Wineland and W. M. Itano. Laser cooling of atoms. *Phys. Rev. A*, 20(4):1521–1540, 1979.

[2] H. J. Metcalf and P. van der Straten. *Laser Cooling and Trapping*. Springer, New York, 1999.

[3] C. J. Foot. Laser cooling and trapping of atoms. *Contemp. Phys.*, 32(6):369–381, 1991.

[4] M. Kasevich and S. Chu. Laser cooling below a photon recoil with three-level atoms. *Phys. Rev. Lett.*, 69(12):1741–1744, 1992.

[5] A. Ashkin. Acceleration and trapping of particles by radiation pressure. *Phys. Rev. Lett.*, 24(4):156–159, 1970.

[6] A. Ashkin and J. P. Gordon. Stability of radiation-pressure particle traps: an optical Earnshaw theorem. *Opt. Lett.*, 8(10):511–513, 1983.

[7] A. Ashkin and J. M. Dziedzic. Observation of radiation-pressure trapping of particles by alternating light-beams. *Phys. Rev. Lett.*, 54(12):1245–1248, 1985.

[8] S. Chu, J. E. Bjorkholm, A. Ashkin, and A. Cole. Experimental observation of optically trapped atoms. *Phys. Rev. Lett.*, 57(3):314–318, 1986.

[9] J. E. Bjorkholm, R. R. Freeman, A. Ashkins, and D. B. Pearson. Observation of focusing of neutral atoms by the dipole forces of resonance-radiation pressure. *Phys. Rev. Lett.*, 41(20):1361–1364, 1978.

[10] E. L. Raab, M. Prentiss, A. Cable, S. Chu, and D. E. Pritchard. Trapping of neutral sodium atoms with radiation pressure. *Phys. Rev. Lett.*, 59(23):2631–2634, 1987.

[11] J. D. Miller, R. A. Cline, and D. J. Heinzen. Far-off-resonance optical trapping of atoms. *Phys. Rev. A*, 47(6):4567–4570, 1993.

[12] D. Frese, B. Ueberholz, S. Kuhr, W. Alt, D. Schrader, V. Gomer, and D. Meschede. Single atoms in an optical dipole trap: towards a deterministic source of cold atoms. *Phys. Rev. Lett.*, 85(18):3777–3780, 2000.

[13] C. E. Wieman. The creation and study of Bose-Einstein condensation in a dilute atomic vapour. *Philos. T. Roy. Soc. A*, 355(1733):2247–2257, 1997.

[14] M. H. Anderson, J. R. Ensher, M. R. Matthews, C. E. Wieman, and E. A. Cornell. Observation of Bose-Einstein condensation in a dilute atomic vapor. *Science*, 269:198–201, 1995.

[15] K. B. Davis, M.-O. Mewes, M. R. Andrews, N. J. van Druten, D. S. Durfee, D. M. Kurn, and W. Ketterle. Bose-Einstein condensation in a gas of sodium atoms. *Phys. Rev. Lett.*, 75(22):3969–3974, 1995.

[16] C.C. Bradley, C. A. Sackett, J. J. Tollett, and R. G. Hulet. Evidence of Bose-Einstein condensation in an atomic gas with attractive interactions. *Phys. Rev. Lett.*, 75(9):1687–1691, 1995.

[17] R. Folman, P. Krüger, J. Schmiedmayer, J Denschlag, and C. Henkel. Microscopic atom optics: from wires to an atom chip. *Adv. At. Mol. Opt. Phys.*, 48:263–356, 2002.

[18] J. Schmiedmayer, R. Folman, and T. Calarco. Quantum information processing with neutral atoms on an atom chip. *J. Mod. Opt.*, 49(8):1375–1388, 2002.

[19] J. Reichel. Microchip traps and Bose-Einstein condensation. *App. Phys. B*, 74(6):469–487, 2002.

[20] K. Brugger, T. Calarco, D. Cassettari, R. Folman, A. Haase, B. Hessmo, P. Krüger, T. Maier, and J. Schmiedmayer. Nanofabricated atom optics: atom chips. *J. Mod. Opt.*, 47(14-15):2789–2809, 2000.

[21] C. D. J. Sinclair, E. A. Curtis, I. Llorente Garcia, J. A. Retter, B. V. Hall, S. Eriksson, B. E. Sauer, and E. A. Hinds. Bose-Einstein condensation on a permanent-magnet atom chip. *Phys. Rev. A*, 72:031603, 2005.

[22] A. Ekert and R. Jozsa. Quantum computation and Shor's factoring algorithm. *Rev. Mod. Phys.*, 68(3):733–753, 1996.

[23] D. P. DiVincenzo. The physical implementation of quantum computation. *Fortschr. Phys.*, 48(9-11):771–783, 2000.

[24] K. Eckert, J. Mompart, X. X. Yi, J. Schliemann, D. Bruß, G. Birkl, and M. Lewenstein. Quantum computing in optical microtraps based on the motional states of neutral atoms. *Phys. Rev. A*, 66:042317, 2002.

[25] S. D. Bartlett and B. C. Sanders. Requirement for quantum computation. *J. Mod. Opt.*, 50(15-17):2331–2340, 2003.

[26] D. Schrader, I. Dotsenko, M. Khudaverdyan, Y. Miroshnychenko, A. Rauschenbeutel, and D. Meschede. Neutral atom quantum register. *Phys. Rev. Lett.*, 93(15):150501, 2004.

[27] S. Du, M. B. Squires, Y. Imai, L. Czaia, R. A. Saravanan, V. Bright, J. Reichel, T. W. Hänsch, and D. Z. Anderson. Atom-chip Bose-Einstein condensation in a portable vacuum cell. *Phys. Rev. A*, 70:053606, 2004.

[28] S. Eriksson, M. Trupke, H. F. Powell, D. Sahagun, C. D. J. Sinclair, E. A. Curtis, B. E. Sauer, E. A. Hinds, Z. Moktadir, C. O. Gollasch, and M. Kraft. Integrated optical components on atom chips. *Eur. Phys. J. D*, 35:135–139, 2005.

[29] X. Liu, K.-H. Brenner, M. Wilzbach, M. Schwarz, T. Fernholz, and J. Schmiedmayer. Fabrication of alignment structures for a fiber resonator using deep UV lithography. *Appl. Optics*, 44(32):6857–6860, 2005.

[30] P. A. Quinto-Su, M. Tscherneck, M. Holmes, and N. P. Bigelow. On-chip optical detection of laser cooled atoms. *Opt. Express*, 12(21):5098–5103, 2004.

[31] R. Long, T. Steinmetz, P. Hommelhoff, W. Hansel, T. W. Hansch, and J. Reichel. Magnetic microchip traps and single-atom detection. *Philos. T. Roy. Soc. A*, 361(1808):1375–1389, 2003.

[32] A. Haase, B. Hessmo, and J. Schmiedmayer. Detecting magnetically guided atoms with an optical cavity. *Opt. Lett.*, 31(2):268–270, 2006.

[33] I. Teper, Y.-J. Lin, and V. Vuletic. Resonator-aided single-atom detection on a microfabricated chip. *Phys. Rev. Lett.*, 97:023002, 2006.

[34] A. D. Kersey. A review of recent developments in fiber optic sensor technology. *Opt. Fiber Technol.*, 2(3):291–317, 1996.

[35] J. Dakin and B. Culshaw, editors. *Optical Fiber Sensors: Principles and Components, Vols. 1 and 2.* Artech House, Inc., 1988.

[36] J. A. Bucaro, H. D. Dardy, and E. F. Carome. Fiber-optic hydrophone. *J. Acoust. Soc. Am.*, 62(5):1302–1304, 1977.

[37] J. P. Dakin, C. A. Wade, and M. Henning. Novel optical fibre hydrophone array using a single laser source and detector. *Europhys. Lett.*, 20(1):53–54, 1983.

[38] H. Koseki and Y. Ohtsuka. Fiber-optic heterodyne gyroscope using two optical beams with orthogonally polarized components. *Opt. Lett.*, 13(9):785–787, 1988.

[39] G. F. Trommer, H. Poisel, W Buhler, E Hartl, and R Muller. Passive fiber optic gyroscope. *Appl. Optics*, 29(36):5360–5365, 1990.

[40] C. E. Lee and H. F. Taylor. Interferometric optical fibre sensors using internal mirrors. *Europhys. Lett.*, 24(4):193–194, 1987.

[41] J. J. Alcoz, C. E. Lee, and H. F. Taylor. Embedded fiber-optic Fabry-Perot ultrasound sensor. *IEEE T. Ultrason. Ferr.*, 37(4):302–306, 1990.

[42] C. E. Lee, W N. Gibler, R. A. Atkins, J. J. Alcoz, and H. F. Taylor. Metal-embedded fiber-optic Fabry-Perot sensors. *Opt. Lett.*, 16(24):1990–1992, 1991.

[43] J. Stone. Optical-fibre Fabry-Perot interferometer with finesse of 300. *Electron. Lett*, 21(11):504–505, 1985.

[44] D. Marcuse and J. Stone. Coupling efficiency of front surface and multilayer mirrors as fiber-end reflectors. *J. Lightwave Technol.*, LT-4(4):377–381, 1986.

[45] J. Stone and L. W. Stulz. Pigtailed high-finesse tunable fibre Fabry-Perot interferometers with large medium and small free spectral ranges. *Electron. Lett*, 23(15):781–783, 1987.

[46] D. Marcuse. Fiber-coupled short Fabry-Perot resonators. *J. Lightwave Technol.*, 7(5):869–876, 1989.

[47] J. Stone and L. W. Stulz. High-performance fibre Fabry-Perot filters. *Electron. Lett*, 27(24):2239–2240, 1991.

[48] K. O. Hill and G. Meltz. Fiber Bragg grating technology fundamentals and overview. *J. Lightwave Technol.*, 15(8):1263–1276, 1997.

[49] P. St. J. Russell, J. L. Archambauld, and L. Reekie. Fibre gratings. *Phys. World*, October:41–46, 1993.

[50] A. D. Kersey, T. A. Berkoff, and W. W. Morey. Multiplexed fiber Bragg grating strain-sensor system with a fiber Fabry-Perot wavelength filter. *Opt. Lett.*, 18(16):1370–1372, 1993.

[51] E. Chehura, C.-C. Ye, and R. P. Tatam. In-line laser Doppler velocimeter using fibre-optic Bragg grating interferometric filters. *Meas. Sci. Technol.*, 14:724–735, 2003.

[52] H. J. Lewandowski. *Coherences and correlations in an ultracold Bose gas.* Phd thesis, University of Colorado, 2002.

[53] M. R. Andrews, M.-O. Mewes, N. J. van Druten, D. S. Durfee, D. M. Kurn, and W. Ketterle. Direct, nondestructive observation of a Bose condensate. *Science*, 273(5271):84–87, 1996.

[54] C. C. Bradley, C. A. Sackett, and R. G. Hulet. Bose-Einstein condensation of lithium: observation of limited condensate number. *Phys. Rev. Lett.*, 78(6):985–989, 1997.

[55] D. J. Riley, M. Mann, D. A. MacLaren, P. C. Dastoor, W. Allison, K. B. K. Teo, G. A. J. Amaratunga, and W. Milne. Helium detection via field ionization from carbon nanotubes. *Nano Lett*, 3(10):1455–1458, 2003.

[56] A. Modi, N. Koratkar, E. Lass, B. Wei, and P. M. Ajayan. Miniaturized gas ionization sensors using carbon nanotubes. *Nature*, 424:171–174, 2003.

[57] T. Ristroph, A. Goodsell, J. A. Golovchenko, and L. V. Hau. Detection and quantized conductance of neutral atoms near a charged carbon nanotube. *Phys. Rev. Lett.*, 94:066102, 2005.

[58] S. Kadlecek, J. Sebby, R. Newell, and T. G. Walker. Nondestructive spatial heterodyne imaging of cold atoms. *Opt. Lett.*, 26(3):137–139, 2001.

[59] V. Savalli, G. Zs. K. Horvath, P. D. Featonby, L. Cognet, N. Westbrook, C. I. Westbrook, and A. Aspect. Optical detection of cold atoms without spontaneous emission. *Opt. Lett.*, 24(22):1552–1554, 1999.

[60] J. E. Lye, J. J. Hope, and J. D. Close. Rapid real-time detection of cold atoms with minimal destruction. *Phys. Rev. A*, 69:023601, 2004.

[61] P. W. H. Pinkse, T. Fischer, P. Maunz, T. Puppe, and G. Rempe. How to catch an atom with single photons. *J. Mod. Opt.*, 47(14-15 SPEC):2769–2787, 2000.

[62] J. Ye, D. W. Vernooy, and H. J. Kimble. Trapping of single atoms in cavity QED. *Phys. Rev. Lett.*, 83(24):4987–4990, 1999.

[63] P. W. H. Pinkse, T. Fischer, P. Maunz, and G. Rempe. Trapping an atom with single photons. *Nature*, 404(6776):365–368, 2000.

[64] P. Maunz, T. Puppe, I. Schuster, N. Syassen, P. W. H. Pinkse, and G. Rempe. Cavity cooling of a single atom. *Nature*, 428(6978):50–52, 2004.

[65] J. McKeever, A. Boca, A. D. Boozer, R. Miller, J. R. Buck, A. Kuzmich, and H. J. Kimble. Deterministic generation of single photons from one atom trapped in a cavity. *Science*, 303:1992–1994, 2004.

[66] P. R. Berman, editor. *Cavity Quantum Electrodynamics, Adv. At. Mol. Opt. Phys. Supp. 2.* Academic Press Inc., Boston, 1994.

[67] B. Lev, K. Srinivasan, P. Barclay, O. Painter, and H. Mabuchi. Feasibility of detecting single atoms using photonic bandgap cavities. *Nanotechnology*, 15:S556–S561, 2004.

[68] P. Domokos, M. Gangl, and H. Ritsch. Single-atom detection in high-Q multimode cavities. *Opt. Commun.*, 185:115–123, 2000.

[69] A. Öttl, S. Ritter, M. Köhl, and T. Esslinger. Correlations and counting statistics of an atom laser. *Phys. Rev. Lett.*, 95:090404, 2005.

[70] H. Mabuchi, Q. A. Turchette, M. S. Chapman, and H. J. Kimble. Real-time detection of individual atoms falling through a high-finesse optical cavity. *Opt. Lett.*, 21(17):1393–1395, 1996.

[71] P. Münstermann, T. Fischer, P. Maunz, P. W. H. Pinkse, and G. Rempe. Dynamics of single-atom motion observed in a high-finesse cavity. *Phys. Rev. Lett.*, 82(19):3791–3794, 1999.

[72] C. J. Hood, T. W. Lynn, A. C. Doherty, A. S. Parkins, and H. J. Kimble. The atom-cavity microscope: single atoms bound in orbit by single photons. *Science*, 287:1447–1453, 2000.

[73] A. Takamizawa, T. Steinmetz, R. Delhuille, T. W. Hänsch, and J. Reichel. Miniature fluorescence detector for single atom observation on a microchip. *Opt. Express*, 14(23):10976–10983, 2006.

[74] M. Trupke, J. Goldwin, B. Darquié, G. Dutier, S. Eriksson, J. Ashmore, and E. A. Hinds. Atom detection and photon production in a scalable, open, optical microcavity. *Phys. Rev. Lett.*, 99(6):063601, 2007.

[75] M. Trupke, F. Ramirez-Martinez, E. A. Curtis, J. P. Ashmore, S. Eriksson, E. A. Hinds, Z. Moktadir, C. Gollasch, M. Kraft, G. Vijaya Prakash, and J. J. Baumberg. Pyramidal micromirrors for microsystems and atom chips. *App. Phys. Lett.*, 88:071116, 2006.

[76] T. Steinmetz, Y. Colombe, D. Hunger, T. W. Hänsch, R. J. Warburton, A. Balocchi, and J. Reichel. Stable fiber-based Fabry-Pérot cavity. *App. Phys. Lett.*, 89:111110, 2006.

[77] H. Mabuchi and H. J. Kimble. Atom galleries for whispering atoms: binding atoms in stable orbits around an optical resonator. *Opt. Lett.*, 19(10):749–751, 1994.

[78] F. Treussart, J. Hare, L. Collot, V. Lefèvre, D. S. Weiss, V. Sandoghdar, J. M. Raimond, and S. Haroche. Quantized atom-field force at the surface of a microsphere. *Opt. Lett.*, 19(20):1651–1653, 1994.

[79] V. Lefèvre-Seguin and S. Haroche. Towards cavity-QED experiments with silica microspheres. *Mater. Sci. Eng.*, B48:53–58, 1997.

[80] D. W. Vernooy, A. Furusawa, N. P. Georgiades, V. S. Ilchenko, and H. J. Kimble. Cavity QED with high-Q whispering gallery modes. *Phys. Rev. A*, 57(4):2293–2296, 1998.

[81] V. S. Ilchenko, P. S. Volikov, V. L. Velichansky, F. Treussart, V. Lefèvre-Seguin, J. M. Raimond, and S. Haroche. Strain-tunable high-Q optical microsphere resonator. *Opt. Commun.*, 145:86–90, 1998.

[82] D. R. Rowland and J. D. Love. Evanescent wave coupling of whispering gallery modes of a dielectric cylinder. *IEEE Proc-J*, 140(3):177–188, 1993.

[83] J. C. Knight, G. Cheung, F. Jacques, and T. A. Birks. Phase-matched excitation of whispering-gallery-mode resonances by a fiber taper. *Opt. Lett.*, 22(15):1129–1131, 1997.

[84] V. S. Ilchenko, X. S. Yao, and L. Maleki. Pigtailing the high-Q microsphere cavity: a simple fiber coupler for optical whispering-gallery modes. *Opt. Lett.*, 24(11):723–725, 1999.

[85] S. M. Spillane. *Fiber-coupled Ultra-high-Q Microresonators for Nonlinear and Quantum Optics*. PhD thesis, California Institute of Technology, 2004.

[86] S. M. Spillane, T. J. Kippenberg, K. J. Vahala, K. W. Goh, E. Wilcut, and H. J. Kimble. Ultrahigh-Q toroidal microresonators for cavity quantum electrodynamics. *Phys. Rev. A*, 71:013817, 2005.

[87] M. Rosenblit, P. Horak, S. Helsby, and R. Folman. Single-atom detection using whispering-gallery modes of microdisk resonators. *Phys. Rev. A*, 70:053808, 2004.

[88] M. Rosenblit, Y. Japha, P. Horak, and R. Folman. Simultaneous optical trapping and detection of atoms by microdisk resonators. *Phys. Rev. A*, 73:063805, 2006.

[89] D. K. Armani, T. J. Kippenberg, S. M. Spillane, and K. J. Vahala. Ultra-high-Q toroid microcavity on a chip. *Nature*, 421:925–927, 2003.

[90] T. Aoki, B. Dayan, E. Wilcut, W. P. Bowen, A. S. Parkins, T. J. Kippenburg, K. J. Valhala, and H. J. Kimble. Observation of strong coupling between one atom and a monolithic microresonator. *Nature*, 443:671–674, 2006.

[91] P. Barclay, K. Srinivasan, O. Painter, B. Lev, and H. Mabuchi. Integration of fiber-coupled high-Q SiN_x microdisks with atom chips. *App. Phys. Lett.*, 89:131108, 2006.

[92] P. Horak, B. G. Klappauf, A. Haase, R. Folman, J. Schmiedmayer, P. Domokos, and E. A. Hinds. Possibility of single-atom detection on a chip. *Phys. Rev. A*, 67(4):043806, 2003.

[93] J. J. Sanchez-Mondragon, N. B. Narozhny, and J. H. Eberly. Theory of spontaneous-emission line shape in an ideal cavity. *Phys. Rev. Lett.*, 51(7):550–553, 1983.

[94] R. J. Thompson, G. Rempe, and H. J. Kimble. Observation of normal-mode splitting for an atom in an optical cavity. *Phys. Rev. Lett.*, 68(8):1132–1135, 1992.

[95] B. E. A. Saleh and M. C. Teich. *Fundamentals of Photonics*. Wiley-Interscience, New York, 1991.

[96] J. P. Goure and I. Verrier. *Optical Fibre Devices*. Series in Optics and Optoelectronics. IoP, Bristol, 2002.

[97] E. Hecht. *Optics, 3rd ed.* Addison Wesley, New York, 1998.

[98] J. M. Vaughan. *The Fabry-Perot Interferometer*. Adam Hilger, Bristol, 1989.

[99] J. Stone and D. Marcuse. Ultrahigh finesse fiber Fabry-Perot interferometers. *J. Lightwave Technol.*, 4(4):382–385, 1986.

[100] R. Kashyap. *Fiber Bragg Gratings*. Optics and Photonics. Academic Press, San Diego, 1999.

[101] V. Finazzi and M. N. Zervas. Effect of periodic background loss on grating spectra. *Appl. Optics*, 41(12):2240–2250, 2002.

[102] J. E. Sipe, L. Poladian, and C. Martijn de Sterke. Propagation through nonuniform grating structures. *J. Opt. Soc. Am. A*, 11(4):1307–1320, 1994.

[103] A. C. Judge, L. Poladian, and C. Martijn de Sterke. Coupled mode theory: limitations and applicability. *J. Mod. Opt.*, 51(3):447–454, 2004.

[104] T. Yoshino, K. Kurosawa, K. Itoh, and T. Ose. Fiber-optic Fabry-Perot interferometer and its sensor applications. *IEEE J. Quantum Elect.*, QE-18(10):1624–1633, 1982.

[105] M. Wilzbach, A. Haase, M. Schwarz, D. Heine, K. Wicker, X. Liu, K.-H. Brenner, S. Groth, Th. Fernholz, B. Hessmo, and J. Schmiedmayer. Detecting neutral atoms on an atom chip. *Fortschr. Phys.*, 54(8-10):746–764, 2006.

[106] A. Melloni, M. Floridi, F. Morichetti, and M. Martinelli. Equivalent circuit of Bragg gratings and its application to Fabry-Pérot cavities. *J. Opt. Soc. Am. A*, 20(2):273–281, 2003.

[107] Y. O. Barmenkov, D. Zalvidea, S. Torres-Peiró, J. L. Cruz, and M. V. Andrés. Effective length of short Fabry-Perot cavity formed by uniform fiber Bragg gratings. *Opt. Express*, 14(14):6394–6399, 2006.

[108] D. I. Babic and S. W. Corzine. Analytic expressions for the reflection delay, penetration depth, and absorptance of quarter-wave dielectric mirrors. *IEEE J. Quantum Elect.*, 28(2):514–524, 1992.

[109] T. Erdogan. Fiber grating spectra. *J. Lightwave Technol.*, 15(8):1277–1294, 1997.

[110] D. L. MacFarlane and E. M. Dowling. Z-domain techniques in the analysis of Fabry-Perot étalons and multilayer structures. *J. Opt. Soc. Am. A*, 11(1):236–245, 1994.

[111] T. Erdogan, V. Mizrahi, P. J. Lemaire, and D. Monroe. Decay of ultraviolet-induced fiber Bragg gratings. *J. Appl. Phys.*, 76(1):73–80, 1994.

[112] S. Helsby, C. Corbari, M. Ibsen, P. Horak, and P. Kazansky. Fiber Bragg gratings for atom chips. *Phys. Rev. A*, 75:013618, 2007.

[113] M. Janos, J. Canning, and M. G. Sceats. Incoherent scattering losses in optical fiber Bragg gratings. *Optics Letters*, 21(22):1827–1829, 1996.

[114] C. G. Askins and M. A. Putnam. Photodarkening and photobleaching in fiber optic Bragg gratings. *J. Lightwave Technol.*, 15(8):1363–1370, 1997.

[115] E. V. Anoikin, V. M. Mashinsky, V. B. Neustruev, and Y. S. Sidorin. Effects of exposure to photons of various energies on transmission of germanosilicate optical fiber in the visible to near IR spectral range. *J. Non-Cryst. Solids*, 179:243–253, 1994.

[116] K. E. Chisholm, K. Sugden, and I. Bennion. Effects of thermal annealing on Bragg fibre gratings in boron/germania co-doped fibre. *J. Phys. D Appl. Phys.*, 31:61–64, 1998.

[117] H. Patrick, S. L. Gilbert, A. Lidgard, and M. D. Gallagher. Annealing of Bragg gratings in hydrogen-loaded optical fiber. *J. Appl. Phys*, 78(5):2940–2945, 1995.

[118] S. R. Baker, H. N. Rourke, V. Baker, and D. Goodchild. Thermal decay of fiber Bragg gratings written in boron and germanium codoped silica fiber. *J. Lightwave Technol.*, 15(8):1470–1477, 1997.

[119] B. Poumellec and F. Kherbouche. The photorefractive Bragg gratings in the fibers for telecommunications. *J. Phys. III France*, 6:1595–1624, 1996.

[120] D. Marcuse. Loss analysis of single-mode fiber splices. *Bell Syst. Tech. J.*, 56(5):703–718, 1977.

[121] M. Saruwatari and K. Nawata. Semiconductor laser to single-mode fiber coupler. *Appl. Optics*, 18(11):1847–1856, 1979.

[122] A. Constable, J. Kim, J. Mervis, F. Zarinetchi, and M. Prentiss. Demonstration of a fiber-optical light-force trap. *Opt. Lett.*, 18(21):1867–1869, 1993.

[123] A. Mahmoud, Z. Ghassemlooy, and L. Chao. Modeling and analysis on the thermal tuning of fiber Bragg gratings for optical communication applications. In *Third International Symposium on Communication Systems Networks and Digital Signal Processing*, pages 86–89, 2002.

[124] A. Bertholds and R. Dandliker. Determination of the individual strain-optic coefficients in single-mode optical fibers. *J. Lightwave Technol.*, 6:17–20, 1988.

[125] D. J. Butler, K. A. Nugent, and A. Roberts. Characterization of optical fibers using near-field scanning optical microscopy. *J. Appl. Phys.*, 75(6):2753–2756, 1993.

[126] M. W. Sasnett. *The Physics and Technology of Laser Resonators*. Taylor and Francis, New York, 1989. Edited by D. R. Hall and P. E. Jackson.

[127] M. Wilzbach, D. Heine, S. Groth, X. Liu, B. Hessmo, and J. Schmiedmayer. A simple integrated single-atom detector. *e-print*, atom-ph/arXiv:0801.3255v1, 2008.

[128] A. D. Kersey, M. J. Marrone, A. Dandridge, and A. B. Tveten. Optimization and stabilization of visibility in interferometric fiber-optic sensors using input-polarisation control. *J. Lightwave Technol.*, 6(10):1599–1609, 1988.

[129] M. Prasciolu, P. Candeloro, R. Kumar, L. Businaro, E. D. Fabrizio, D. Cojoc, S. Cabrini, C. Liberale, and V. Degiorgio. Fabrication of diffractive optical elements on-fiber for photonic applications by nanolitography. *Jpn. J. Appl. Phys.*, 42(6B):4177–4180, 2003.

[130] I. S. Grant and W. R. Phillips. *Electromagnetism*. Wiley, Chichester, 1990.